

The Impact of Interfaces on the Performance of Organic Photovoltaic Cells

Roland Steim



Scientific
Publishing

Roland Steim

**The Impact of Interfaces on the Performance
of Organic Photovoltaic Cells**

The Impact of Interfaces on the Performance of Organic Photovoltaic Cells

by
Roland Steim

Dissertation, Karlsruher Institut für Technologie
Fakultät für Elektrotechnik und Informationstechnik, 2010

Impressum

Karlsruher Institut für Technologie (KIT)
KIT Scientific Publishing
Straße am Forum 2
D-76131 Karlsruhe
www.ksp.kit.edu

KIT – Universität des Landes Baden-Württemberg und nationales
Forschungszentrum in der Helmholtz-Gemeinschaft



Diese Veröffentlichung ist im Internet unter folgender Creative Commons-Lizenz
publiziert: <http://creativecommons.org/licenses/by-nc-nd/3.0/de/>

KIT Scientific Publishing 2010
Print on Demand

ISBN 978-3-86644-526-0

The Impact of Interfaces on the Performance of Organic Photovoltaic Cells

Zur Erlangung des akademischen Grades eines

DOKTOR-INGENIEURS

von der Fakultät für
Elektrotechnik und Informationstechnik
des Karlsruher Instituts für Technologie (KIT)

genehmigte
DISSERTATION
von

Dipl.-Ing. Roland Steim
geb. in: Karlsruhe

Tag der mündlichen Prüfung: 29.04.2010
Hauptreferent: Prof. Dr. rer. nat. Uli Lemmer
Korreferent: Prof. Dr. Christoph J. Brabec

Publications:

Journal Publications:

R. Steim, F. René Kogler, and C. J. Brabec, Interface materials of organic solar cells, *Journal of Materials Chemistry* 20, 2499 (2010).

R. Steim, P. Schilinsky, S. A. Choulis, and C. J. Brabec, Flexible polymer photovoltaic modules with incorporated organic bypass diodes to address module shading effects, *Solar Energy Materials and Solar Cells*, 93, 11, 1963 (2009).

C. N. Hoth, **R. Steim**, P. Schilinsky, S. A. Choulis, S. F. Tedde, O. Hayden, and C. J. Brabec, Topographical and morphological aspects of spray coated organic photovoltaics, *Organic Electronics* 10, 4, 587 (2009).

R. Steim, S. A. Choulis, P. Schilinsky, U. Lemmer, and C. J. Brabec, Formation and impact of hot spots on the performance of organic photovoltaic cells, *Applied Physics Letters* 94, 043304 (2009).

R. Steim, S. A. Choulis, P. Schilinsky, and C. J. Brabec, Interface modification for highly efficient organic photovoltaics, *Applied Physics Letters* 92, 093303 (2008).

Submitted contribution to book chapter “Printed organic photovoltaic“, “Photovoltaic materials: from crystalline silicon to 3rd generation approaches“ edited by Gavin Conibeer, Wiley-VCH, Weinheim.

Conference Presentations and Posters:

R. Steim, P. Schilinsky, F. R. Kogler, C. J. Brabec, Origin of the s-shape current-voltage characteristics in OPV Cells, MRS Fall Meeting 2009, Boston, USA.

R. Steim, S. A. Choulis, P. Schilinsky, C. J. Brabec, Interface engineering concepts for highly efficient inverted organic photovoltaics, MRS Spring Meeting 2009, San Francisco, USA.

R. Steim, S. A. Choulis, P. Schilinsky, C. J. Brabec, The influence of hot spots on the performance of organic photovoltaics, Photonics Europe 2008, Strasbourg, France.

R. Steim, S. A. Choulis, P. Schilinsky, C. J. Brabec, Degradation mechanisms due to shading effects on organic solar cell modules, Frühjahrstagung der DPG 2008, Berlin, Germany.

Zusammenfassung

Die ökonomische und umweltfreundliche Erzeugung von Elektrizität ist von bedeutender Rolle um den Energiebedarf der Weltbevölkerung weiterhin zu decken. Hierbei spielen erneuerbare Energien, wie die Photovoltaik, eine entscheidende Rolle. Die Photovoltaik ermöglicht die Umwandlung von Sonnenenergie in Elektrizität ohne CO₂ Ausstoß. Die organische Photovoltaik (OPV) weist ein hohes Potential gegenüber anderen Photovoltaiktechnologien auf, da flexible OPV Module kostengünstig durch Druckverfahren auf Rolle- zu- Rolle Basis realisiert werden können, die Prozessenergie niedrig ist und somit eine positive Energiebilanz nach kurzer Zeit erreicht wird. Ein ästhetischer Vorteil von OPV liegt darin, dass Module in unterschiedlichen Farben hergestellt werden können. Die Farbe ist hierbei durch den eingesetzten Absorber bestimmt.

Um das Potential der organischen Photovoltaik auszuschöpfen und konkurrenzfähig zu den anderen Technologien zur Energieerzeugung zu machen ist eine hohe Effizienz und Stabilität der OPV Module von Notwendigkeit. In dieser Arbeit wird gezeigt, dass optimierten Interfacematerialien neben der Absorberschicht eine bedeutende Rolle zukommt. Designregeln für exzellente Interfacematerialien werden in dieser Arbeit aufgestellt.

In dieser Arbeit wird die Stabilität von OPV Zellen bei einer angelegten Rückwärtsspannung untersucht. Eine hohe Stabilität bei angelegter Rückwärtsspannung ist insbesondere für die abgeschattete Zelle innerhalb eines seriell verschalteten Moduls wichtig, da die abgeschattete Zelle in Rückwärtsrichtung betrieben wird. OPV Zellen unter einer angelegten Rückwärtsspannung degradieren unter der Abnahme des Parallelwiderstandes, begleitet durch die Bildung von sogenannten „Hot Spots“, d.h. punktuellen Bereichen mit erhöhter Wärmedissipation unter einer Rückwärtsspannung. Der Parallelwiderstand bzw. Leckstrom wird als entscheidender Parameter zur Vorhersage der Stabilität von OPV Zellen identifiziert. OPV Zellen mit einem Leckstrom größer als 100 µA/cm² bei -1 V zeigen eine deutliche Degradation bei Anlegen einer Rückwärtsspannung von -5 V für 5 h. Dagegen sind OPV Zellen mit einem Leckstrom niedriger als 100 µA/cm² bei -1 V stabil unter denselben Bedingungen.

Zusammenfassung

Die Anforderungen der OPV innerhalb von Gebäuden („Anwendung unter schwachem Licht“) zur Erzeugung von Elektrizität wird ebenfalls experimentell untersucht. Es wird gezeigt, dass ein hoher Parallelwiderstand für die Effizienz der OPV Zelle unter schwachem Licht deutlich wichtiger ist als unter einer Sonne. OPV Zellen mit gleicher Effizienz unter einer Sonne, aber unterschiedlichen Parallelwiderständen haben bei schwachen Lichtintensitäten (z.B. 1000 lx) verschiedene Effizienzen in Abhängigkeit ihres Parallelwiderstandes. Nur OPV Zellen und Module mit einem hohen Parallelwiderstand haben eine hohe Effizienz sowohl unter einer Sonne als auch bei schwachen Lichtintensitäten. Dagegen ist für Anwendungen der OPV unter schwachem Licht der Einfluss des Serienwiderstandes geringer als bei Beleuchtung unter einer Sonne. In dieser Arbeit wird gezeigt, dass für OPV Zellen unter schwacher Beleuchtung von 1000 lx ein Parallelwiderstand größer als $85 \text{ k}\Omega\text{cm}^2$ notwendig ist. Im Gegensatz dazu reicht ein Parallelwiderstand größer als $1 \text{ k}\Omega\text{cm}^2$ für die Bestrahlung unter einer Sonne aus. Ein Serienwiderstand von weniger als $50 \Omega\text{cm}^2$ ist ausreichend für schwache Lichtintensitäten im Gegensatz zu weniger als $3 \Omega\text{cm}^2$ für die Bestrahlung unter 1 Sonne. Der geringere Einfluss des Serienwiderstands für die Anwendungen der OPV Zellen unter schwachem Licht erlaubt den Einsatz von Interface- und Elektrodenmaterialien mit schlechterer Leitfähigkeit. Durch die Anforderung eines hohen Parallelwiderstandes für den Einsatz der OPV unter schwachem Licht werden jedoch exzellente Interfacematerialien benötigt, welche einen hohen Parallelwiderstand der OPV Zelle bewirken.

Die Integration von organischen Bypass-Dioden in OPV Module erlaubt die Prozessierung von Modulen mit Bypass-Dioden in den gleichen Prozessschritten, was die Vorteile der OPV beibehält. In dieser Arbeit wird gezeigt, dass OPV Zellen mit einem hohen Parallelwiderstand gute organische Bypass-Dioden sind mit ähnlichen Eigenschaften wie anorganische Bypass-Dioden. In dieser Arbeit wird gezeigt, dass ein hoher Parallelwiderstand essentiell für verschiedene Anwendungen der OPV ist. Hot Spots, welche in zahlreichen OPV Modulen vorkommen, sind die Ursache für einen reduzierten Parallelwiderstand. In dieser Arbeit wird aus der Kombination von Photostrom und Thermographie eine Technik entwickelt, welche es erlaubt zwischen einer defekten Interfaceschicht und einer defekten Absorberschicht zu unterscheiden. Diese Messungen geben Aufschluss, welche der Schichten für einen höheren Parallelwiderstand optimiert werden muss. Die durchgeführten Messungen zeigen, dass eine Ursache für Hot Spots

defekte Interfaceschichten sind. Daher sind optimierte Interfacematerialien notwendig, um einen hohen Parallelwiderstand einer OPV Zellen zu gewährleisten und weiter zu erhöhen. Ein erhöhter Parallelwiderstand bei gleichzeitig niedrigerem Serienwiderstand wurde durch Modifizierung der Interface Schicht erreicht. OPV Zellen mit der Schichtenfolge aus den Interfacematerialien polyoxyethylene tridecyl ether (PTE) und Titandioxid (TiO_x) als Elektronen-selektiver Kontakt zeigen Effizienzen von 3.6 % im Vergleich zu 3.2 % für OPV Zellen ohne PTE. Diese Verbesserung wird auf eine bessere Benetzung von TiO_x zurückgeführt, da sich weder die Arbeitsfunktion noch die chemische Zusammensetzung von TiO_x durch das PTE verändert.

Die Notwendigkeit einer exzellenten und an das Absorbermaterial angepassten Interfaceschicht wird im Detail anhand von TiO_x diskutiert. TiO_x erlaubt die Analyse eines unangepassten und eines exzellenten Interfacematerials in derselben OPV Zelle, da sich TiO_x durch UV Bestrahlung von einem limitierenden Interfacematerial in ein exzeptentes Interfacematerial umwandeln lässt. Ohne UV-Bestrahlung zeigen OPV Zellen mit TiO_x eine S-förmige Strom-Spannungs (J-V) Kennlinie welche mit UV Bestrahlung verschwindet. Dies resultiert in einer höhere Effizienz. Es wird gezeigt, dass sich die Leitfähigkeit von TiO_x mit ähnlicher Dynamik ändert, wie das Verschwinden und Auftauchen der S-förmigen J-V Kennlinie mit und ohne UV Bestrahlung. Ergebnisse aus Simulationen untermauern diese Beobachtungen. Durch die alleinige Änderung der Beweglichkeit oder Dotierung der TiO_x Schicht ist die Simulation der J-V Kennlinien mit und ohne S-Form möglich. Der Abfall des elektrischen Feldes in der Nähe als auch über die Interfaceschicht aus TiO_x und kaum innerhalb der aktiven Schicht resultiert in der S-Form der J-V Kennlinie. Für J-V Kennlinien ohne S-Form ist der Abfall des elektrischen Feldes hingegen hoch innerhalb der aktiven Schicht. Eine experimentelle Verschlechterung der Leitfähigkeit der Interfaceschicht durch Einbringen einer dünnen, isolierenden Schicht aus SiO_x resultiert in einer effizienzlimitierenden S-Form der J-V Kennlinie. Diese Ergebnisse weisen darauf hin, dass die S-Form der J-V Kennlinie auf eine Verschlechterung der Leitfähigkeit der Interfaceschichten zurückzuführen ist.

Zusammenfassend wird demonstriert, dass die richtige Wahl der Interfaceschichten sehr wichtig für effiziente und stabile OPV Zellen und Module ist, sowohl für die Anwendung der OPV unter einer Sonne als auch unter „Niedriglicht“ Bedingungen. Ein hoher Parallelwiderstand ist hierfür von entscheidender Bedeutung, der wiederum maßgebend vom

Zusammenfassung

Interfacematerial beeinflusst wird. Ein unangepasstes Interfacematerial kann die Effizienz und Eigenschaften einer OPV Zelle deutlich verschlechtern, was anhand von TiO_x gezeigt wird. Die Eigenschaften sowie die zahlreichen in der Literatur beschriebenen Interfacematerialien sind für den Leser zusammengefasst.

Die Entwicklung von noch effizienteren und stabileren OPV Zellen und Modulen erhöht die Attraktivität dieser Technologie weiter und macht sie konkurrenzfähig zu anderen PV Technologien und Energiequellen. Die Optimierung von Interfacematerialien spielt hierbei eine ebenso große Rolle wie die Weiterentwicklung der Absorberschicht.

Danksagung

Ich möchte mich bei Prof. Dr. rer. nat. Uli Lemmer für die Betreuung und Unterstützung während meiner Doktorarbeit bedanken. Prof. Dr. Christoph Brabec gilt mein Dank für zahlreiche Diskussionen und der Übernahme des Korreferats. Für die gute Betreuung sowie für zahlreiche Diskussion möchte ich mich bei Prof. Dr. Stelios Choulis, Dr. Pavel Schilinsky und Dr. F. René Kogler bedanken.

Ein großer Teil dieser Arbeit ist bei Konarka Technologies GmbH in Nürnberg entstanden. Ich möchte mich bei den Mitarbeitern von Konarka für das gute Arbeitsklima und bei der Firma Konarka für die finanzielle Unterstützung sowie der zur Verfügung Stellung der Labors bedanken.

Nicht unwesentlichen Anteil am Entstehen dieser Dissertation hatten all meine Freunde. Ich möchte mich bei Euch allen für die manch schönen Abende und Tage bedanken.

Mein Dank gilt meinen Eltern, die mich bis zum jetzigen Zeitpunkt in jeglicher Hinsicht unterstützt haben.

Contents

1	INTRODUCTION	1
2	FUNDAMENTALS OF ORGANIC PHOTOVOLTAICS – MATERIALS, CHARACTERIZATION AND PROCESSING	7
2.1	FUNDAMENTALS OF ORGANIC PHOTOVOLTAICS.....	7
2.1.1	<i>Organic Semiconductors</i>	7
2.1.2	<i>Charge Generation in a Bulk-Heterojunction</i>	8
2.2	CURRENT-VOLTAGE PARAMETERS AND MODELS OF SOLAR CELLS	11
2.2.1	<i>Macroscopic Device Model.....</i>	12
2.2.2	<i>Microscopic Device Model.....</i>	14
2.3	LIGHT SOURCES.....	15
2.4	EXPERIMENTAL	17
2.4.1	<i>Doctor Blading</i>	17
2.4.2	<i>Thermal Evaporation.....</i>	18
2.4.3	<i>Materials and Device Structure.....</i>	18
2.5	MEASUREMENT METHODS	21
2.5.1	<i>Current-Voltage Measurements</i>	21
2.5.2	<i>Conductivity Measurements</i>	22
2.5.3	<i>Dark Lock-In Thermography.....</i>	23
2.5.4	<i>Light Beam Induced Current Measurements.....</i>	24
2.5.5	<i>Ultraviolet and X-Ray Photoelectron Spectroscopy.....</i>	25
3	REVIEW ON INTERFACE MATERIALS AND THEIR FUNCTION.....	27
3.1	THEORY OF CONTACT FORMATION ACTIVE LAYER/INTERFACIAL LAYER.....	27
3.2	PURPOSE OF INTERFACIAL LAYERS	30
3.2.1	<i>Impact on the Open-Circuit Voltage</i>	30
3.2.2	<i>Polarity of the Device</i>	34
3.2.3	<i>Electrode Materials – Conductive Layers.....</i>	36
3.2.4	<i>Optical Spacer</i>	36

Contents

3.2.5	<i>Protective Layer between Polymer and Electrode</i>	37
3.2.6	<i>Formation of Carrier Selective Contact and Exciton Blocking Layer</i>	37
3.3	MATERIALS OVERVIEW FOR INTERFACIAL LAYERS	38
3.3.1	<i>Metals</i>	38
3.3.2	<i>Semiconducting Layers</i>	40
3.3.2.1	Inorganic Materials - Metal Oxides	41
3.3.2.1.1	P-Type Inorganic Materials	41
3.3.2.1.2	N-Type Inorganic Materials.....	43
3.3.2.2	Organic Layers	45
3.3.2.2.1	P-Type Organic Materials	45
3.3.2.2.2	N-Type Organic Materials	47
3.3.3	<i>Dipole Layers</i>	48
3.3.3.1	Self-Assembled Monolayers	50
3.3.3.2	Salts	52
3.4	SUMMARY	54
4	IMPACT OF THE SHUNT RESISTANCE ON THE PERFORMANCE OF ORGANIC PHOTOVOLTAIC CELLS	55
4.1	HOT SPOTS.....	56
4.1.1	<i>Reverse Bias Testing</i>	56
4.1.2	<i>Degradation under Reverse Bias in Hot Spots</i>	57
4.1.3	<i>Summary</i>	61
4.2	LOW LIGHT APPLICATIONS	62
4.2.1	<i>Impact of the Shunt Resistance for Low Light Applications</i>	63
4.2.2	<i>Summary</i>	67
4.3	ORGANIC BYPASS DIODES	68
4.3.1	<i>Design Rules for Organic Bypass Diodes</i>	69
4.3.2	<i>Summary</i>	75
4.4	TYPE OF SHUNTS IN ORGANIC PHOTOVOLTAIC	75
4.4.1	<i>Origin of the Shunt in Organic Photovoltaic Cells</i>	77
4.4.2	<i>Summary</i>	81
5	INTERFACE ENGINEERING	83

5.1	INTERFACE MODIFICATION FOR HIGHLY EFFICIENT ORGANIC PHOTOVOLTAICS.....	83
5.1.1	<i>Improved Interfaces by Stacking of Solution Processed Organic and Inorganic Layers</i> 84	
5.1.2	<i>Origin of the Improvement with PTE</i>	87
5.1.3	<i>Summary</i>	91
5.2	S-SHAPE CURRENT-VOLTAGE CHARACTERISTICS IN ORGANIC PHOTOVOLTAIC CELLS	
	92	
5.2.1	<i>Introduction</i>	92
5.2.2	<i>Behavior of Organic Photovoltaic Cells under UV-VIS Irradiation.....</i>	95
5.2.3	<i>Simulation of the S-shape Current-Voltage Characteristic.....</i>	98
5.2.4	<i>Experimental Simulation of the S-shape Current-Voltage Characteristic</i>	111
5.2.5	<i>Summary</i>	115
6	SUMMARY AND CONCLUSION	117
	ABBREVIATIONS AND SYMBOLS	121
	LIST OF FIGURES.....	125
	LIST OF TABLES.....	127
	BIBLIOGRAPHY	129

1 Introduction

The development and commercialization of renewable energy sources, like photovoltaics (PV), is a must for future energy supply scenarios. The need for a “clean” renewable energy source becomes necessary due to the increase in costs of non-renewable energy sources like oil and coal and due to the problems caused by carbon dioxide (CO_2) emission. Herein solar energy plays a crucial role since it converts solar radiation, available at no cost, into electricity without CO_2 emission. Electricity from solar energy can be produced in large grid connected power plants, as well as via little stand alone power sources which makes this technology attractive. Figure 1-1 summarizes the world wide available renewable energy compared to the Global Primary Energy Consumption (GPEC).

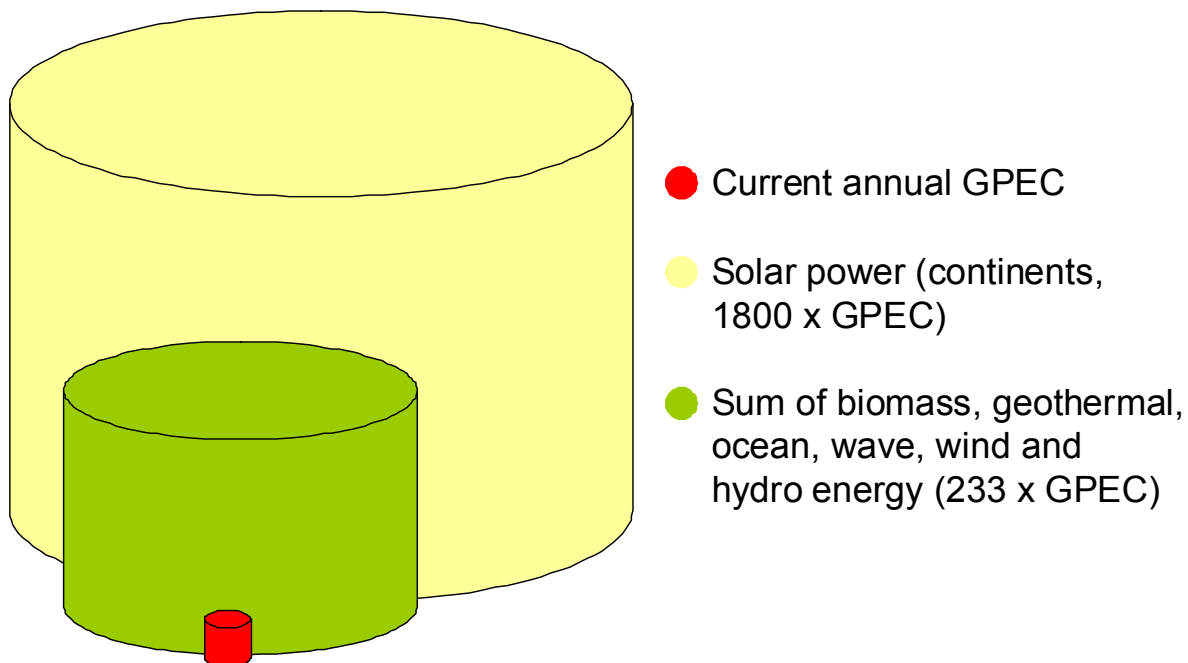


Figure 1-1: Comparison of the available renewable energy sources to the global primary energy consumption in 2007.^{1,2}

Renewable energy sources, including wind energy, biomass, geothermal energy, hydro energy, ocean and wave energy, together provide the 233 fold energy of GPEC. The worldwide available solar power on the continents is as high as 1800 GPEC. As such, the use of only a little fraction of the total solar power can cover the GPEC.^{1,2} However, the yearly

1 Introduction

sum of global irradiation on the continents is not distributed equally all over the world.³ Motivated by the high yearly sum of global irradiation in some parts of the world, projects for the production of solar electricity in those areas for the rest of the world, e.g. the Sahara, have been initiated.⁴

The European Photovoltaic Industry Association predicts the growth of the photovoltaic world market from 5.6 GW in 2008 to up to 22 GW in 2013. This study assumes that the development of PV is policy driven, e.g. motivated PV investment by Feed-in Tariffs. Figure 1-2 summarizes the expected development of the photovoltaic industry from 2000 to 2008, and the assumed development until 2013. Approximately 90% of the PV power generated today in Europe is in Spain and Germany in 2008.⁵ Crystalline silicon is the most widely used material for solar modules. However, it is expensive in production and has a very high energy payback time. Therefore, the search for alternative photo-active materials providing the potential to solve future energy supply scenarios is investigated. This includes inorganic, e.g. thin film technologies like amorphous silicon, CIS, CIGS and CdTe, as well as organic materials.

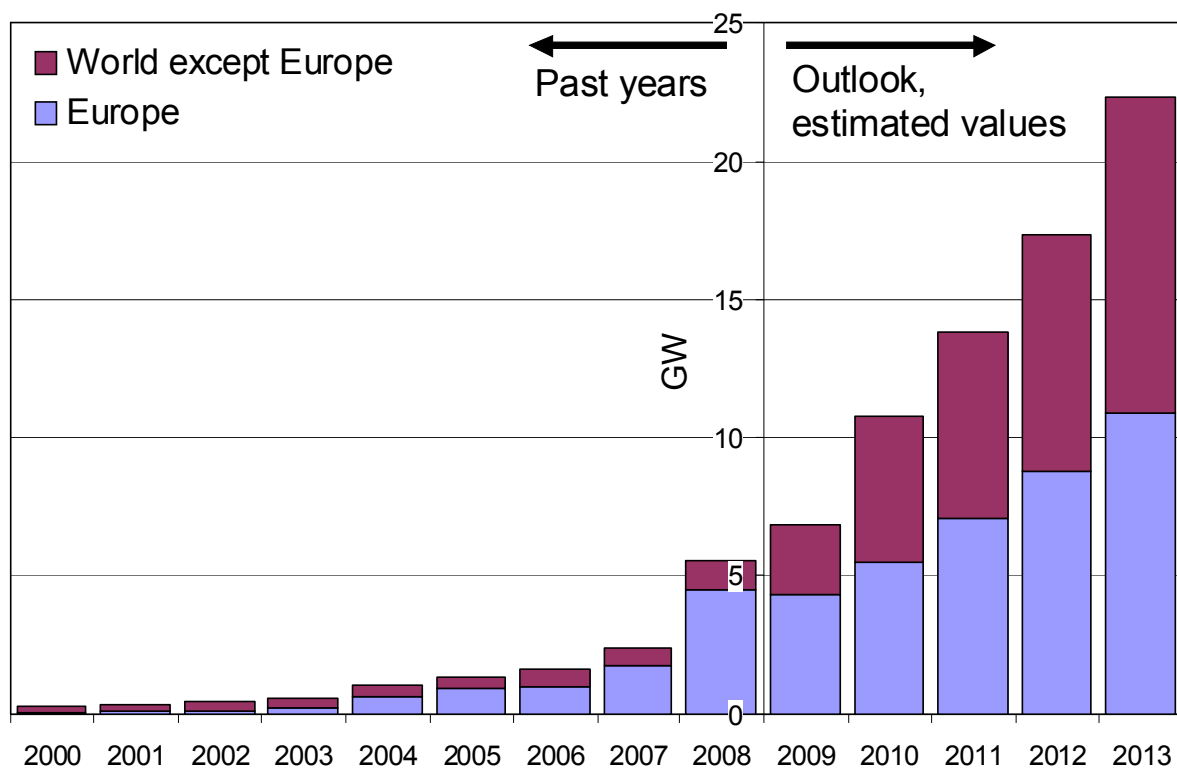


Figure 1-2: Global annual PV market growth (policy driven scenario).⁵

Organic photovoltaic (OPV) provides all the advantages that polymers provide, such as tunable properties of the photo-active and interfacial layers plus the feasibility for cheap roll-to-toll processing.

The potential of OPV is based mainly on these advantages:

- The absorption of organic materials for OPV is very high. A layer thickness of some 100 nm is sufficient to absorb most of the light, which saves material costs.
- The processing of polymer OPV is feasible through low temperature printing technologies in a roll-to-roll production method. Assuming a web speed of 10 m/sec at a foil width of 2 – 3 m a productivity of up to 50,000 – 100,000 m²/hr can be achieved. This high productivity combined with a relative low initial investment cost for solution processed OPV results in prices in the range of 0.5 €/W_p and even lower in the near future. This value is below the one of Si-modules.⁶
- The production of OPV devices on flexible and lightweight substrates opens up new application categories, e.g. the integration of OPV modules in portable electronics and clothes which allows charging electronic devices in everyday life without grid connection. Integration of OPV modules into buildings offers functional design possibilities.⁷
- The usage of semi-transparent OPV modules makes them attractive for integration into windows.
- The tunable “colours” of OPV modules allow OPV applications with attractive design.
- The low-temperature roll-to-roll printing technology on flexible substrates is a well established technology compatible to other printing technologies and well established for the photographic film and magnetic tape production. The demand for those “old” technologies decreases and unused production capacities from these technologies can be used for OPV production. Relatively low investment costs of production facilities for printed OPV modules allow new business models and financing mechanisms which makes this technology attractive for more investors. On the other hand, for Si based solar cells this initial investment is very high which is particularly problematic during financial crises.
- One criticism of the Si technology is the low energy balance, defined as the ratio between energy needed for production and energy output during module lifetime. For

the Si technology a module lifetime of 2 – 8 years is required for a positive energy balance. The corresponding value can be as low as a few weeks for OPV.⁶

To further strengthen the potential of OPV and make this technology competitive to other solar cell technologies and energy sources the research efforts in this field have to be strengthened by e.g. further increase the power conversion efficiency (PCE) and lifetime of OPV modules. Most organic materials used for OPV applications are sensitive to oxygen and water which limits lifetime. Despite these challenges, PCEs of up to 7.9 %⁸, certified by the U.S. Department of Energy's National Renewable Energy Laboratory, and outdoor lifetime of 3 years⁹ are impressive values for the young OPV technology. In combination with the successful demonstration of OPV production by printing technologies^{10, 11} first applications are already entering the market. Theoretical studies assigned this technology a possible PCE of well above 10% and further increased lifetime, which makes OPV an attractive candidate to solve future energy supply scenarios. Beside the development and synthesis of novel and improved absorber materials, the engineering of improved interface materials is of importance for highly efficient and stable OPV cells and modules, since unadjusted interfaces limit or even drastically reduce the performance of OPV cells which is discussed and demonstrated in this work. The need for the right choice of interface materials is demonstrated for varying aspects and applications of OPV. From these findings design rules for OPV applications are derived and improved interfacial layers are presented.

The thesis is organized as follows. Starting with an introduction to this thesis in chapter 1, chapter 2 outlines the fundamentals of OPV, the investigated devices structure as well as measurement and characterization methods applied while this work. In chapter 3 a literature review of the recent progress in the development and understanding of interface materials for OPV is presented which is published in the Journal of Materials Chemistry [*R. Steim, Rene F. Kogler, and C. J. Brabec, Interface materials of organic solar cells, Journal of Materials Chemistry* 20, 2499 (2010)]. Chapter 4 presents experimental results of OPV cells for reverse bias degradation [*R. Steim, S. A. Choulis, P. Schilinsky, U. Lemmer, and C. J. Brabec, Formation and impact of hot spots on the performance of organic photovoltaic cells, Applied Physics Letters* 94, 043304 (2009)], low light applications, organic bypass diodes [*R. Steim, P. Schilinsky, S. A. Choulis, and C. J. Brabec, Flexible polymer photovoltaic modules with incorporated organic bypass diodes to address module shading effects, Solar Energy Materials and Solar Cells*, 93, 11, 1963 (2009)] and derives design rules for those

applications emphasizing the need of a high shunt resistance. The origin of a low shunt resistance is investigated. In chapter 5 improved interfaces and therefore device performance are presented [*R. Steim, S. A. Choulis, P. Schilinsky, and C. J. Brabec, Interface modification for highly efficient organic photovoltaics, Applied Physics Letters 92, 093303 (2008)*]. The origin of this improvement is discussed. The need for excellent interfaces is discussed exemplarily for TiO_x , an interfacial layer which is switchable by UV irradiation from an unadjusted, device performance limiting interfacial layer to an excellent interfacial layer. Experimental and simulation results are combined to create an understanding of this behaviour.

2 Fundamentals of Organic Photovoltaics – Materials, Characterization and Processing

In this chapter an introduction to organic semiconductors and charge generation in OPV cells is given, focusing on the photoactive layer. Relevant device parameters, characterization and processing methods used in this work are outlined.

2.1 Fundamentals of Organic Photovoltaics

One important milestone in the development of organic photovoltaic is the discovery and development of conducting polymers by A. J. Heeger, A. MacDiarmid and H. Shirakawa in 1976^{12,13} for which they received the Nobel Prize in Chemistry in 2000.¹⁴ A second important finding is by Tang et al. in 1986. They reported that combining an electron donor with an electron acceptor leads to efficiencies of approximately 1 %, which is a major breakthrough in 1986.¹⁵

In this sub-chapter a short introduction to organic semiconductors is given. Concentrating on the photo-active layer, the relevant processes for charge and current generation are discussed.

2.1.1 Organic Semiconductors

Organic compounds with only single bonds ("saturated compounds") have 4 single bonds (σ -bonds) per C atom. The σ -electrons are strongly bound. (sp^3 -hybridized). Polymers which have only σ -bonds in the backbone are electrically insulating. In order to have semiconducting properties, polymers must have backbones with alternating single and double bonds, which form a delocalized π -electron system. Polyacetylene is a basic example of a conjugated polymer. The structure of polyacetylene is shown in Figure 2-1. Each carbon atom has 3 strongly bound σ -bonds and one weak π -bond (sp^2 -hybridization). Optical excitation of a π -electron with light results in the transition of the electron from the ground state to an excited state. The transition with the lowest energy usually corresponds to the promotion of the electron from the highest occupied molecular orbital (HOMO) to the lowest unoccupied molecular orbital (LUMO). The energy difference between HOMO and LUMO is related to the optical band gap of the organic semiconductor. In case the HOMO is not

fully populated, the π -electrons become mobile along the polymer chain and can be transferred by hopping processes from one polymer chain to another one. Therefore they are called semiconducting polymers in analogy to inorganic semiconductors.^{16,17}

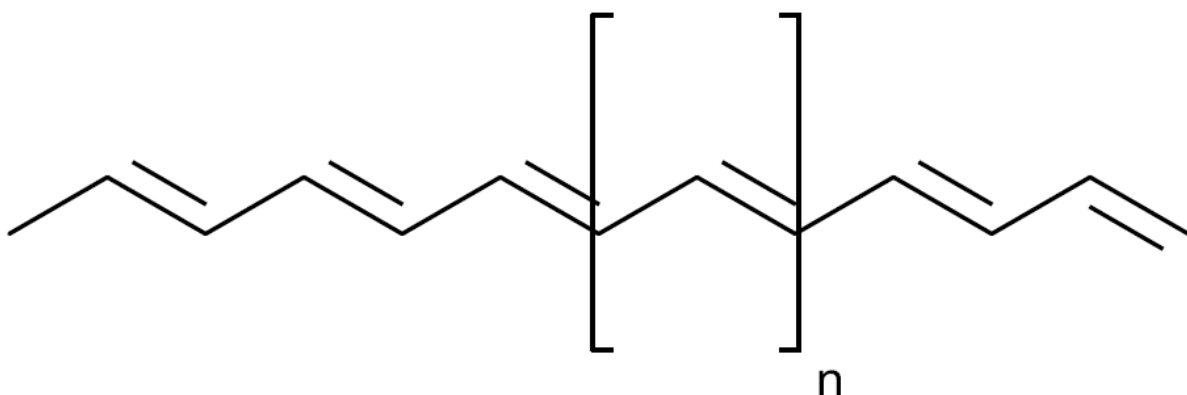


Figure 2-1: Chemical structure of polyacetylene.

2.1.2 Charge Generation in a Bulk-Heterojunction

A fundamental difference between inorganic photovoltaic materials and organic semiconductors is the creation of strongly bound electron-hole pairs (excitons) upon absorption of light in the latter. The energy which is required to split an exciton is in the range of 0.1 - 0.4 eV and is thus much larger than the thermal energy kT at standard conditions. Moreover, the electric field is not sufficient to dissociate these excitons.¹⁸ In order to split excitons into free charge carriers, the energy can be provided by the transfer of the electron to an electron accepting material with a higher electron affinity. A typical organic semiconducting material system which enables effective exciton splitting and also being used in this work is poly(3-hexylthiophene) (P3HT) and [6,6]-phenyl C61 butyric acid methyl ester (PCBM). Due to the high absorption cross sections of conjugated polymers, the density of light-generated excitons is generally high in a bulk heterojunction cell. The diffusion length of excitons is typically in the range of 5 – 10 nm.¹⁸ Diffusion of the exciton towards a donor-acceptor interface where it is split into charge carriers is thus the limiting process of charge carrier formation. The layer thicknesses in bilayer devices consisting of acceptor and donor are thus strongly limited to the diffusion length of excitons. This in turn limits the absorbance of the device. A way to overcome these limitations in layer thickness is the

preparation of so called bulk-heterojunction devices by depositing mixed solutions of donor and acceptor materials. The bulk heterojunction is not only a random mixture of two materials but also consists of homogeneously distributed acceptor and donor phases with appropriate dimensions to effectively split excitons in the whole bulk. This is schematically shown in Figure 2-2. Once these excitons are split into free carriers they are transported via percolated donor and acceptor pathways to the corresponding electrodes, i.e. electrons by the acceptor to the cathode and holes by the donor to the anode. In this work this definition of anode and cathode is used. The definition depends whether charge carriers are injected or extracted. Due to the close proximity of holes and electrons in the bulk heterojunction devices, the charge carriers recombine quickly on the way to the electrodes. The thickness limiting factor of this configuration is thus the mobility-lifetime product of the carriers. The fundamental processes from light harvesting to power generation are graphically illustrated in Figure 2-2 and can be summarized as follows:

- (a) light is absorbed by the donor, i.e. P3HT, and excitons are created. Absorption of the acceptor is neglected in this description.
- (b) excitons diffuse to the donor-acceptor interface and split into free carriers.
- (c) the carriers are transported to the respective electrode, electrons by the acceptor to the cathode and holes by the donor to the anode.
- (d) the carriers are extracted to the electrode by the help of interfacial layers.

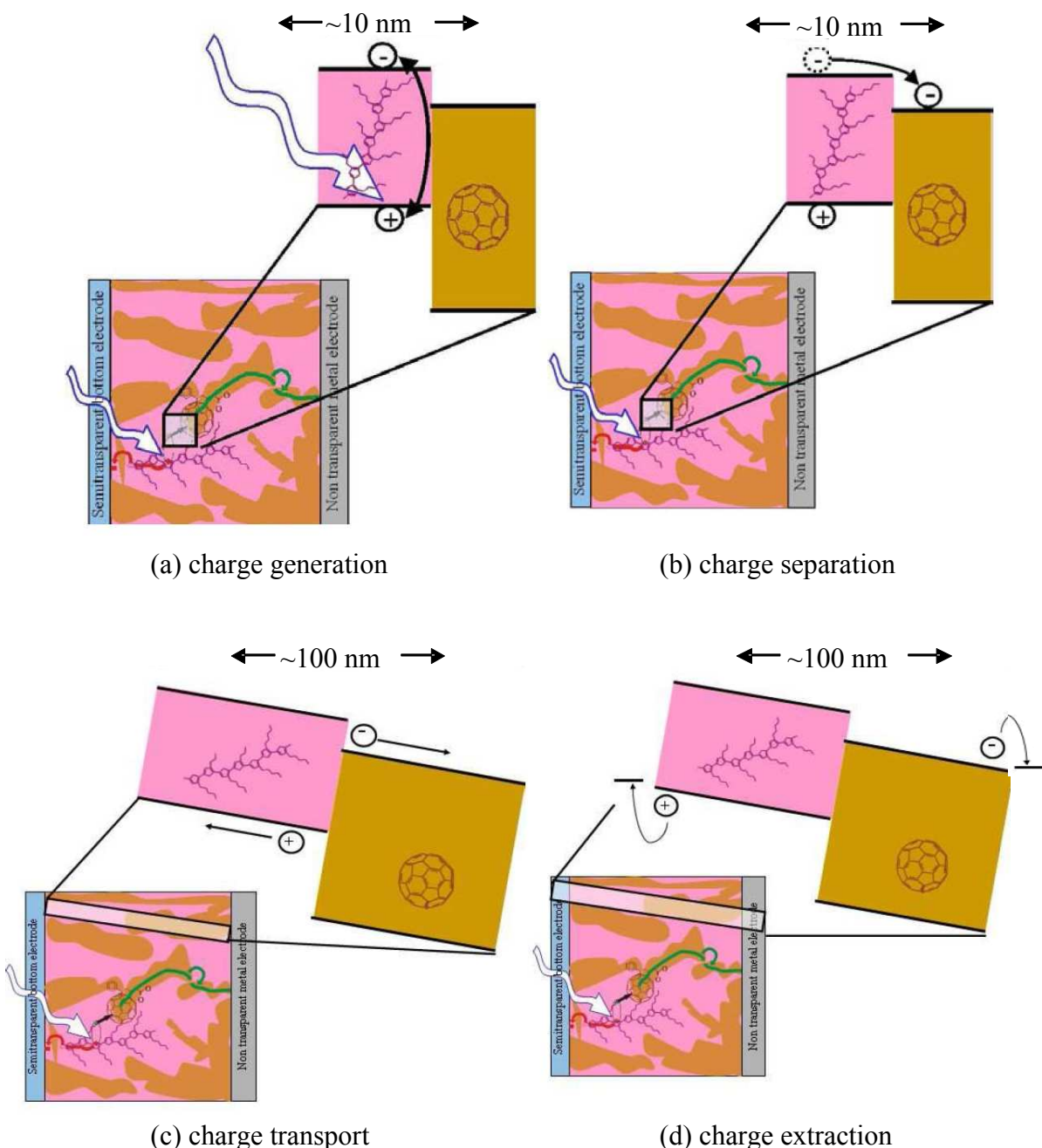


Figure 2-2: Scheme of light harvesting and charge generation in OPV cells. The brown phase is the acceptor. The red phase is the donor. (a) Light is absorbed by the donor, i.e. P3HT, and excitons are created. (b) Excitons diffuse to the donor-acceptor interface and split into free carriers. (c) The carriers are transported to the respective electrode, electrons by the acceptor to the cathode and holes by the donor to the anode. (d) The carriers are extracted to the electrode by the help of interfacial layers.¹⁹

2.2 Current-Voltage Parameters and Models of Solar Cells

In this subchapter the basic parameters of the current-voltage (J-V) characteristic of a solar cell is presented. The application of the "one diode model" to bulk heterojunction solar cells is discussed and fundamental parameters that can be derived either from the one diode model or directly from J-V curves are presented.

Depending on the voltage which is applied to the electrodes, the carriers are injected into or extracted from the solar cell. The open-circuit voltage (V_{oc}) is defined as the externally applied voltage at which no current is flowing in the outer circuit. At V_{oc} , all photo-generated carriers recombine within the active layer. The built-in voltage (V_{bi}) is defined as the maximal voltage that V_{oc} can reach in an OPV device and is usually higher than the measured V_{oc} due to contribution of the dark current. V_{bi} can be estimated by the voltage for which the photo-generated current ($I_{photogenerated}$) under 1 sun is zero. It can be experimentally derived by subtracting the J-V curve measured in the dark from the J-V curve measured under illumination of 1 sun.^{18, 20}

In the following, the injection mode and extraction mode of the solar cell is defined in terms of V_{oc} , since the extracted or injected current to the outer circuit is of interest, neglecting the difference in V_{bi} and V_{oc} . For external voltages higher than V_{oc} ($V > V_{oc}$) carriers are injected. In opposite, for voltages below V_{oc} ($V < V_{oc}$), carriers are extracted to the respective electrodes, i.e. holes by the anode and electrons by the cathode. If the external voltage is sufficiently smaller than V_{oc} , the electric field inside the device is sufficient to extract the majority of photo-generated carriers, thus minimizing recombination losses. The short-circuit current density (J_{sc}) is the current extracted from the solar cell when no external voltage is applied. The electrical field required to extract the carriers is provided by the solar cell. The OPV cell generates power when it is driven in the 4th quadrant, i.e. for voltages between 0 V and V_{oc} . The maximum power point (MPP) is the working point of the device for which the highest power is generated. The corresponding voltage and current at MPP conditions are named V_{MPP} and J_{MPP} , respectively. The power output is maximum where the product of voltage multiplied with current is maximum. Graphically this can be represented by the area of the largest rectangle under the J-V curve in the fourth quadrant. The fill factor (FF) is the ratio between the power output at the MPP and the theoretical maximum power output.

$$FF = \frac{V_{MPP} * J_{MPP}}{V_{oc} * J_{sc}} \quad (2.1)$$

The power conversion efficiency (PCE) is the ratio between the electric power output at the MPP (P_{OUT}) and the luminous power hitting the cell (P_{IN}).

$$PCE = \eta_{Power} = \frac{P_{OUT}}{P_{IN}} = \frac{J_{MPP} * V_{MPP}}{P_{IN}} = \frac{FF * J_{SC} * V_{OC}}{P_{IN}} \quad (2.2)$$

2.2.1 Macroscopic Device Model

For the macroscopic solar cell model the basic electrical equivalent-circuit is the “one-diode-model” which is shown in Figure 2-3. This model consists of a diode, a current source, a parallel shunt resistance and a serial resistance. The current source provides the photo-generated current $I_{photogenerated}$. The diode, combined with the shunt resistance (R_p) and serial resistance (R_s) determines the selectivity of the OPV cell.

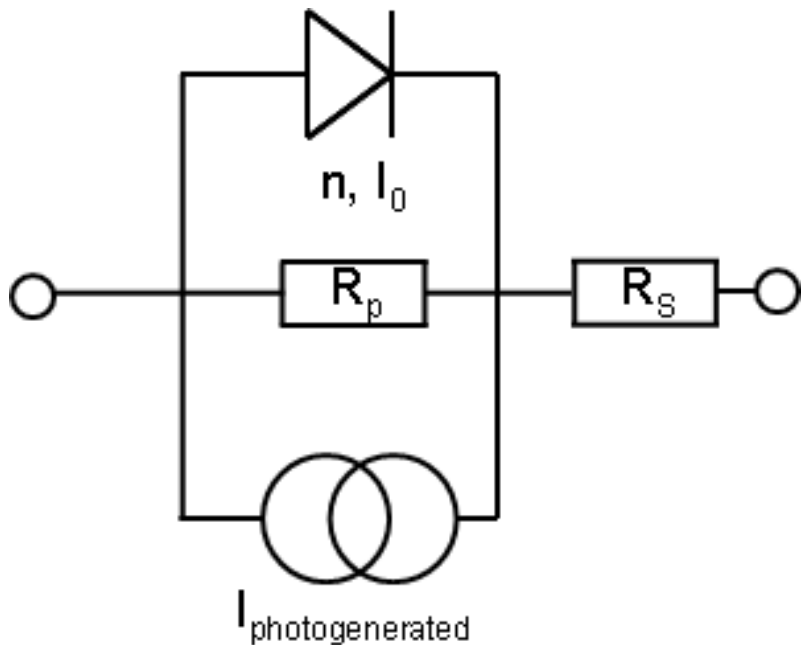


Figure 2-3: One diode model of a solar cell.

Based on this model the current balance of this circuit can be written as:

$$I - I_0 \cdot \left(\exp\left(\frac{e \cdot (V - I \cdot R_s)}{n_i \cdot k_B \cdot T}\right) - 1 \right) - \frac{(V - I \cdot R_s)}{R_p} - I_{photogenerated} = 0, \quad (2.3)$$

where I is the current, I_0 is the saturation current, k_B is the Boltzmann constant, T is the temperature, V is the externally applied voltage, e is the elementary charge and n_i is the

ideality factor of the diode.¹⁹ For sufficiently high R_p the current through the shunt resistance can be neglected and V_{oc} ($I = 0$) can be written as:

$$V_{oc} = \frac{n k_B T}{e} \ln\left(\frac{I_{photogenerated}}{I_0} + 1\right) \sim \ln(I_{photogenerated}) \quad (2.4)$$

V_{oc} shows a logarithmic dependence on the photo-generated current. It has been shown that J_{sc} correlates linearly with the light intensity.^{21, 22} Thus, V_{oc} is proportional to the logarithm of the light intensity.

From the dark J-V characteristics R_p , R_s , n , I_0 and the leakage current can be derived. R_p is the slope of the J-V curve at reverse bias while the leakage current is defined as the current density at an arbitrary voltage in reverse bias. Figure 2-4 demonstrates the impact of the resistances R_p and R_s on the J-V characteristics of an OPV cell.

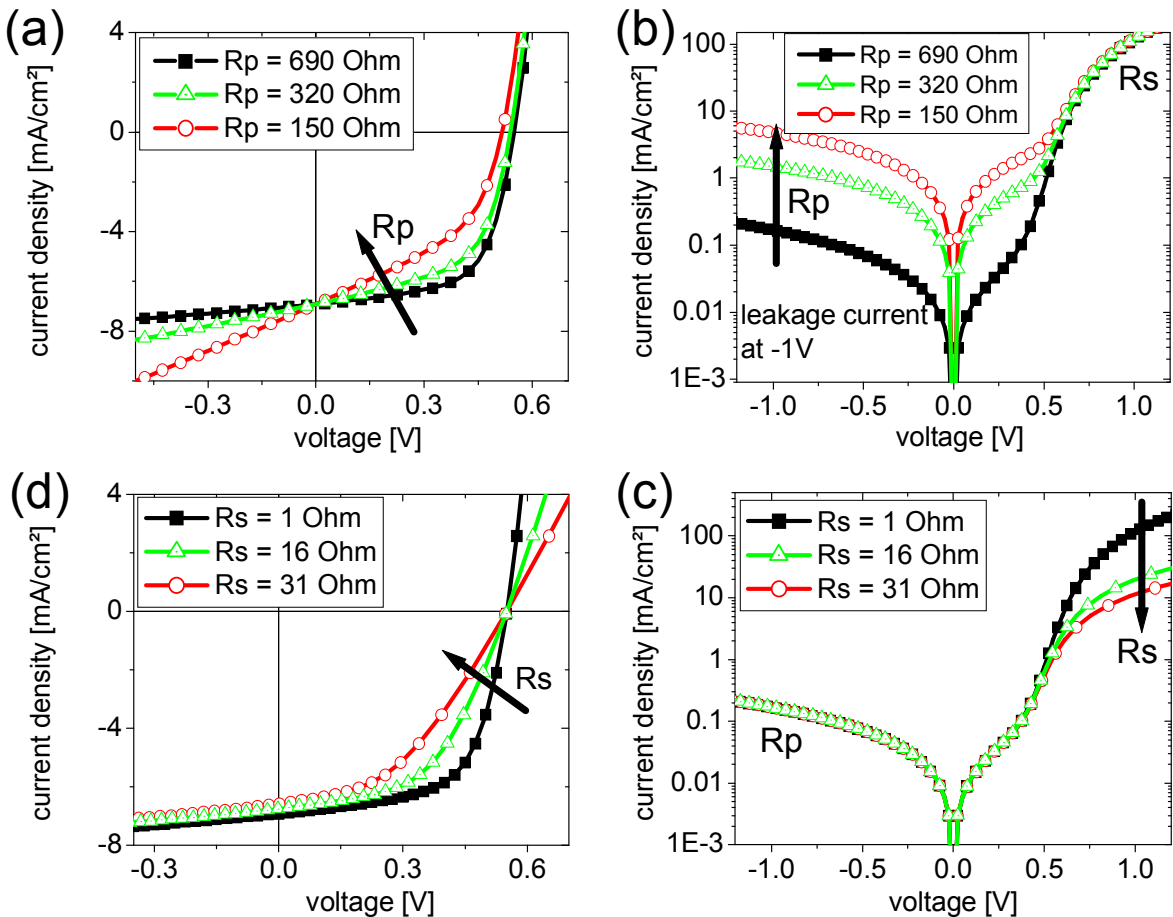


Figure 2-4: Impact of R_s and R_p on the performance of OPV cells at 1 sun. The black (rectangular) J-V curve is measured at 1 sun. For the others the change in R_p or R_s is numerically calculated to the measured J-V curve.

A variation of R_p from 690 Ohm to 150 Ohm (Figure 2-4 a) and b)) clearly reduces the OPV performance due to a decrease in FF and, to a lesser extent, also in V_{oc} . J_{sc} is not affected, because at short circuit conditions no current flows through R_p . The dark leakage current at -1V increases by a factor of 50 on going from $R_p = 690$ Ohm to 150 Ohm. The injection current does not change significantly. Upon variation of the serial resistance from $R_s = 1$ Ohm to $R_s = 31$ Ohm (Figure 2-4 (c) and (d)), the FF drops significantly while J_{sc} decreases only slightly. V_{oc} is not affected, because at open circuit conditions no current flows through R_s . The leakage current does not change significantly when varying R_s . Summarizing, R_p is the limiting resistance in reverse polarity whereas R_s is the limiting resistance in forward polarity. For high efficiency OPV cells a high shunt resistance and a low serial resistance is thus essential.

2.2.2 Microscopic Device Model

A microscopic device model based on solving the full set of relevant coupled differential equations is utilized for simulating J-V characteristics. This model allows the simulation of the band structure, electrical field distribution and other important parameters within a one-dimensional semiconductor structure. The relevant equations are the hole and electron continuity equations, the Poisson equations and the current transport equation noted here:

$$\begin{aligned} I_n &= q \cdot \mu_n \cdot (n \cdot E + \frac{k \cdot T}{q} \cdot \frac{\partial n}{\partial x}) \\ I_p &= q \cdot \mu_n \cdot (n \cdot E + \frac{k \cdot T}{q} \cdot \frac{\partial n}{\partial x}) \\ \frac{\partial n}{\partial t} &= G - R(p, n) + \frac{1}{q} \cdot \frac{\partial I_n}{\partial x} \\ \frac{\partial p}{\partial t} &= G - R(p, n) + \frac{1}{q} \cdot \frac{\partial I_p}{\partial x} \\ \frac{\partial E}{\partial x} &= -\frac{\rho(x)}{\varepsilon} \end{aligned} \tag{2.5}$$

with the mobility μ of the electrons and holes, the generation rate G , the recombination rate R , the electrical field E , and the densities of negative and positive charge carrier n and p , respectively, the current of electrons and holes $I_{n,p}$, the net charge ρ , the elementary charge q and the dielectric constant ε .^{19,23} For solving these equations and illustrating the band

structure the software PC1D²⁴ is used which is based on the fundamental equations of inorganic semiconductor physics.

2.3 Light Sources

The spectrum of the sun matches best with a black body radiator with the temperature of 5760 K. When light passes the atmosphere, different parts of the spectrum are absorbed or scattered by different atmospheric constituents. Oxygen, nitrogen and ozone absorb light below 300 nm. H₂O absorbs light at 900, 1100, 1400 and 1900 nm. CO₂ absorbs light at 1800 and 2600 nm. As such the spectrum and light intensity of the sun at the earth depend on the optical path length of the light through the atmosphere. The “Air Mass” (AM) factor attributes to this and is defined as the quotient of the “optical path length to the sun” and the “optical path length if the sun is directly overhead”.²⁵ Solar cells are typically measured at AM1.5 and a light intensity of 100 mW/cm². Figure 2-5 illustrates the spectrum of the sun compared to the absorption of P3HT.

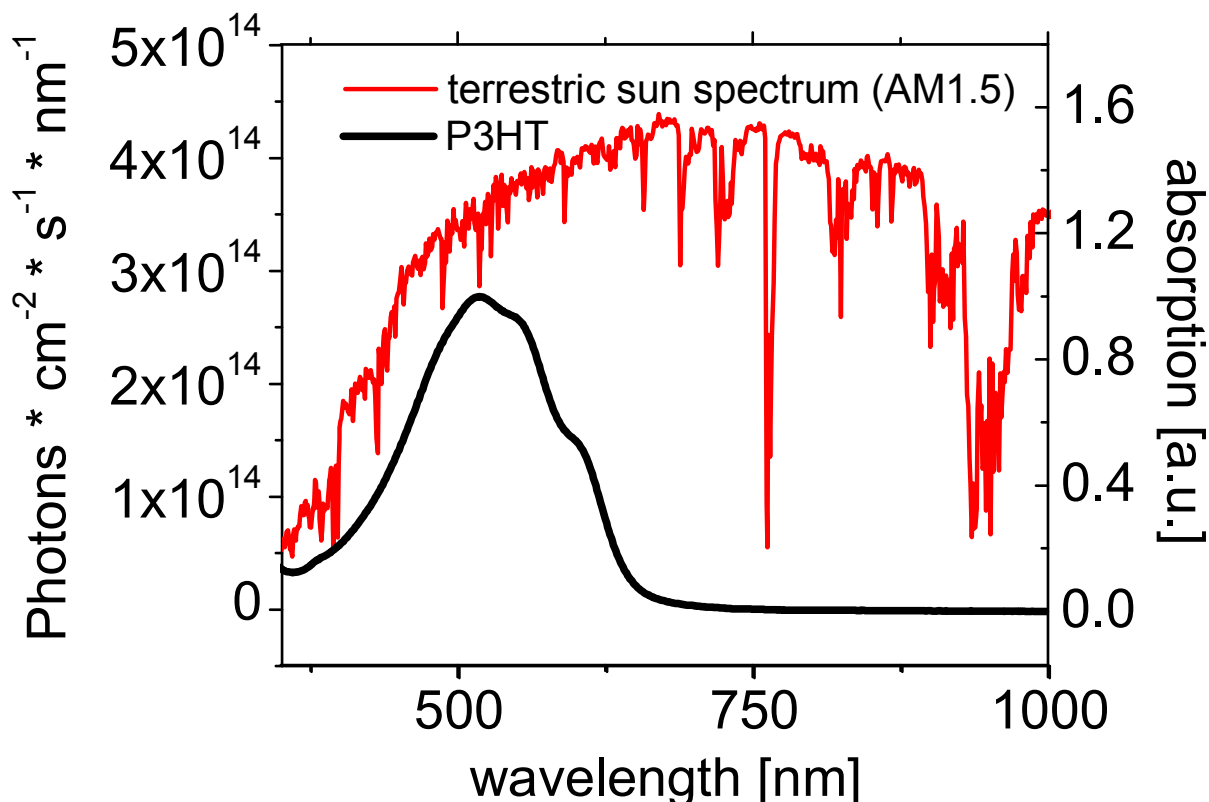


Figure 2-5: Comparison of the AM1.5 spectrum of the sun with the absorption of P3HT. The unit for the terrestrial sun spectrum are photons*cm⁻²*s⁻¹*nm⁻¹. The absorption of P3HT is given in arbitrary units.

For indoor applications fluorescent lamps as light sources in professional lighting are widely used. In these lamps electrons are emitted from one electrode and accelerated by an electric field towards the other electrode. These electrons collide with atoms placed in the bulb, e.g. mercury, and excite those. The excited atoms emit resonance radiation. In the case of low-pressure discharge lamps with mercury, i.e. fluorescent lamps, this resonance radiation is UV radiation. The UV radiation is transformed by different fluorescent powders coated on the bulb into visible light.²⁶ In dependence of the kind and amount of different fluorescent powders used varying light colours can be designed. A typical value to quantify artificial light sources is the luminous flux. The luminous flux is defined as the energy flow per unit time weighted by the sensitivity of the human eye.²⁶ Figure 2-6 presents the spectrum of a fluorescent lamp with the light colour 830.

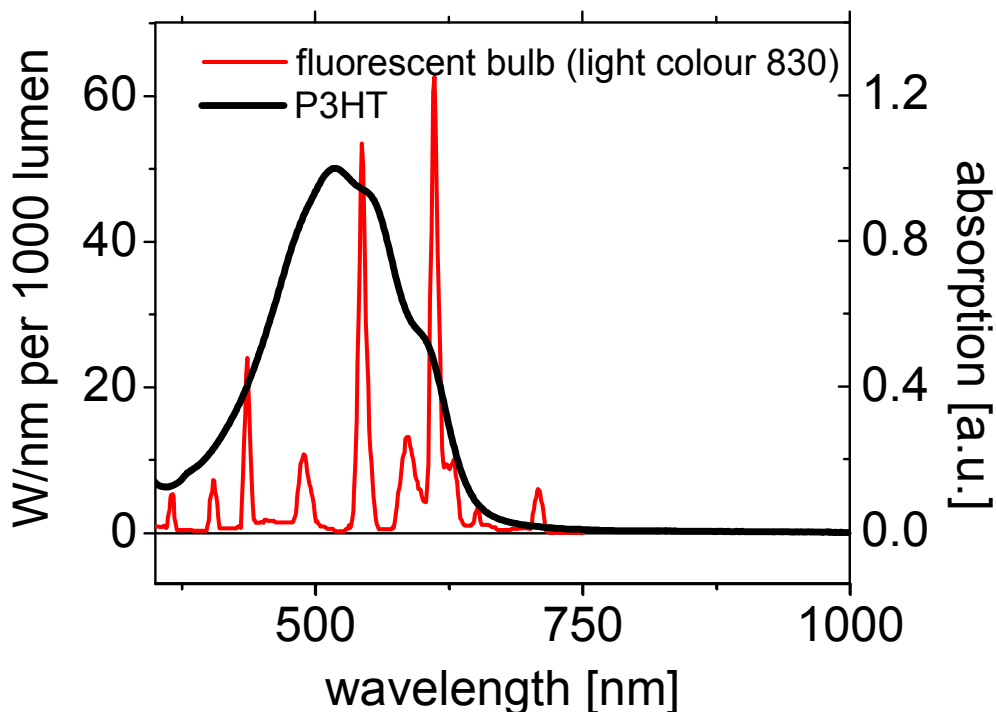


Figure 2-6: Comparison of the absorption of P3HT with the spectrum of a fluorescent lamp weighted by the sensitivity of the human eye. The spectrum of the fluorescent lamp is given in W/nm per 1000 lumen. The absorption of P3HT is given in arbitrary units.

The spectrum of the fluorescent lamp is limited to the visible range and is not continuous in contrast to the spectrum of a black body radiator.

2.4 Experimental

The processing methods and the device structures investigated in this thesis are presented here. Except for the electrode materials, it is attempted to deposit organic and inorganic layers exclusively by solution processing in ambient atmosphere since this technology has a great advantage concerning the up-scaling to fast, continuous and low-cost roll-to-roll production techniques on plastic substrates. On the laboratory scale, doctor blading has emerged as a suitable method to apply thin films from solution. The metal top electrode is thermally evaporated. The device structure, processing and materials used in this thesis are presented.

2.4.1 Doctor Blading

Doctor blading is a very flexible method concerning the processing parameters and yields reproducible results with high film quality. The schematic is shown in Figure 2-7.

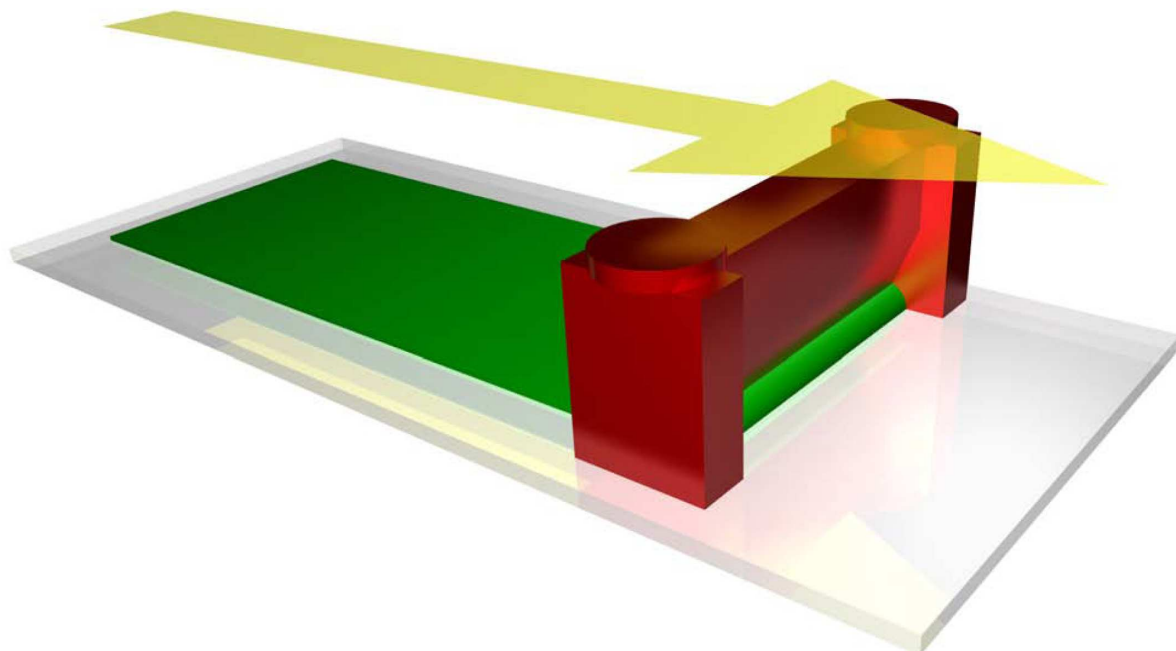


Figure 2-7: Schematic illustration of the doctor-blade technique.⁸³

A blade moves over the substrate at a height of some 100 µm. In the slit between the substrate and the coating knife the solution is placed, moved over the substrate, leaving behind a wet film of the solution over the substrate. The solvent evaporates and leaves only

the solid on the substrate. The substrate can be heated. The parameters affecting the layer thickness and the quality of the layer are the surface energy of the substrate, the amount of solution left on the surface, as well as the vapour pressure, the concentration, and the viscosity of the solution. The amount of solution left behind by the blade increases with the blading velocity, with the distance of the coating knife from the substrate as well as with the angle of the blade. The vapour pressure increases with the temperature of the substrate and of the blade.

2.4.2 Thermal Evaporation

The top electrodes of the device are metal contacts which are vapour-deposited onto the solution processed layers. The metal to be evaporated is melted by a current to the boiling point under high vacuum conditions (10^{-6} mbar). The vacuum is needed to increase the mean free path length of the evaporating metal to decrease the possibility of collisions with other particles and molecules. A shadow mask placed over the active layers determines which areas are metallized.

2.4.3 Materials and Device Structure

The materials and device structures investigated in this work are presented in this section. All chemicals and solvents used in this work are purchased from Sigma-Aldrich and used without further purification. P3HT is bought from Merck. Poly(3,4-Ethylenedioxythiophene) (PEDOT):poly(styrene-sulfonate) (PSS) is bought from H. C. Starck. The structural formulas of these materials are shown in Figure 2-8. The device structure investigated is the inverted structure indium tin oxide (ITO)/titanium oxide (TiO_x)/P3HT:PCBM/PEDOT:PSS/Ag illustrated in Figure 2-9 (a). This device architecture acts as reference for further improved structures and is the one under investigation unless otherwise noted. The corresponding HOMO and LUMO levels of the relevant materials are presented in Figure 2-9 (b).

ITO/ TiO_x is the selective contact for electrons, i.e. the cathode. Ag/PEDOT:PSS is the selective contact for holes, i.e. the anode. The substrate is either glass or a flexible PET foil which is coated with ITO through a sputtering process providing a sheet resistance of below $20\ \Omega/\text{Square}$. The ITO is structured in stripes.

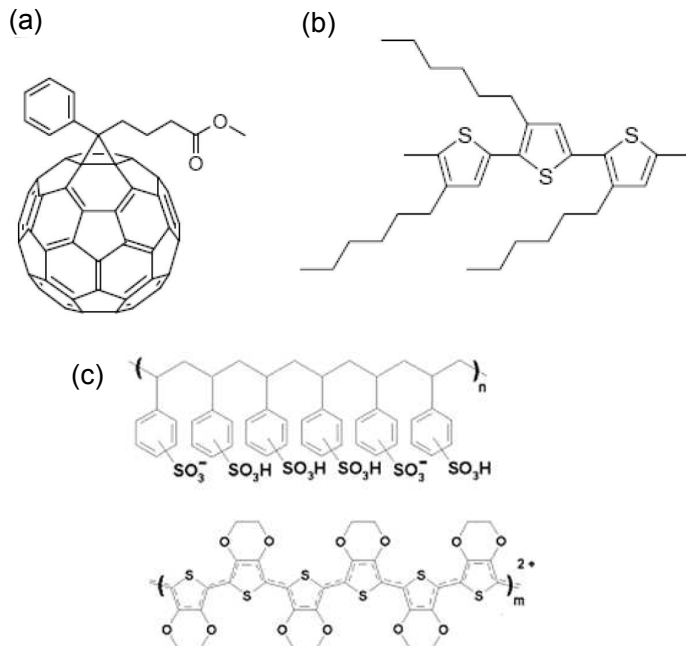


Figure 2-8: Chemical structure of (a) PCBM, (b) P3HT, (c) PEDOT and PSS.

The ITO coated glass substrates are sonicated for 10 min in acetone and another 10 min in isopropanol. Before blading the next layer the ITO is treated by ozone for 10 min to increase its surface energy and thus improve the wetting of the TiO_x layer.

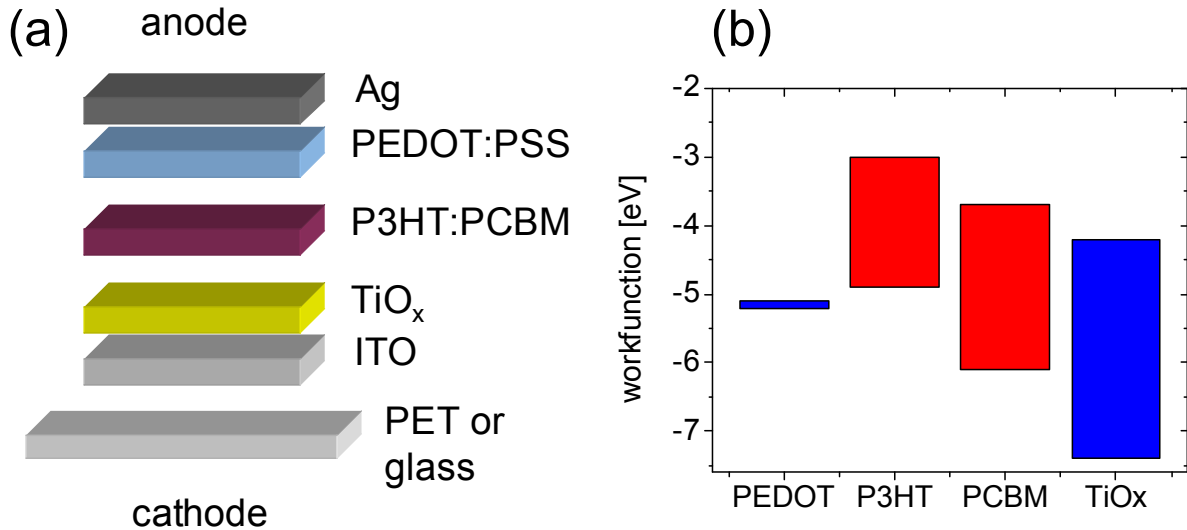


Figure 2-9: (a) Inverted device structure investigated in this work and acting as reference system. (b) HOMO and LUMO levels of the investigated materials of the inverted device structure. The values for the work function are taken from literature²⁷ and vary depending on the literature source.

The ITO coated PET foil is cleaned for 10 min in an isopropanol ultrasonic bath. TiO_x is deposited in a sol-gel process by doctor blading on ITO. After processing, TiO_x is stored for 2 hours in air to be converted by hydrolysis.

The photo-active layer consists of a bulk-heterojunction of P3HT and PCBM. P3HT and PCBM are dissolved in o-xylene and deposited by doctor blading on the ITO/ TiO_x layer resulting in a layer thickness of 250 nm. The PEDOT:PSS solution is diluted in isopropanol and coated on top of the photo-active layer. Subsequently, the morphology of the photoactive layer is adjusted by heat treatment. All process steps up to the photo-active layer are performed in ambient atmosphere under clean-room conditions. Finally, an Ag electrode is thermally evaporated on top of the PEDOT:PSS layer as illustrated in Figure 2-10.

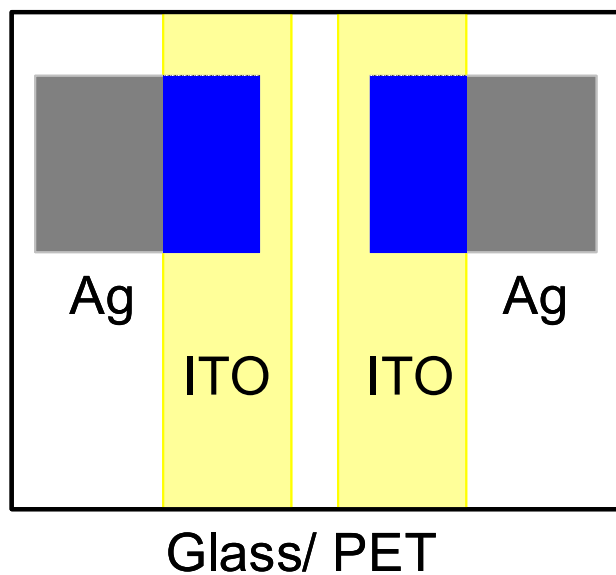


Figure 2-10: Exemplary layout of the investigated OPV cells. The crossover of the ITO electrode with the Ag electrode is marked blue and forms the active area.

The crossover of the ITO and Ag forms the active layer. The solar cells under investigation have a typical active area between 20 mm^2 and 100 mm^2 . The investigated OPV modules are serially interconnected. The schematic for a 3 stripe module is illustrated in Figure 2-11. All J-V measurements presented here were performed after 20 min of UV-VIS irradiation of the device.

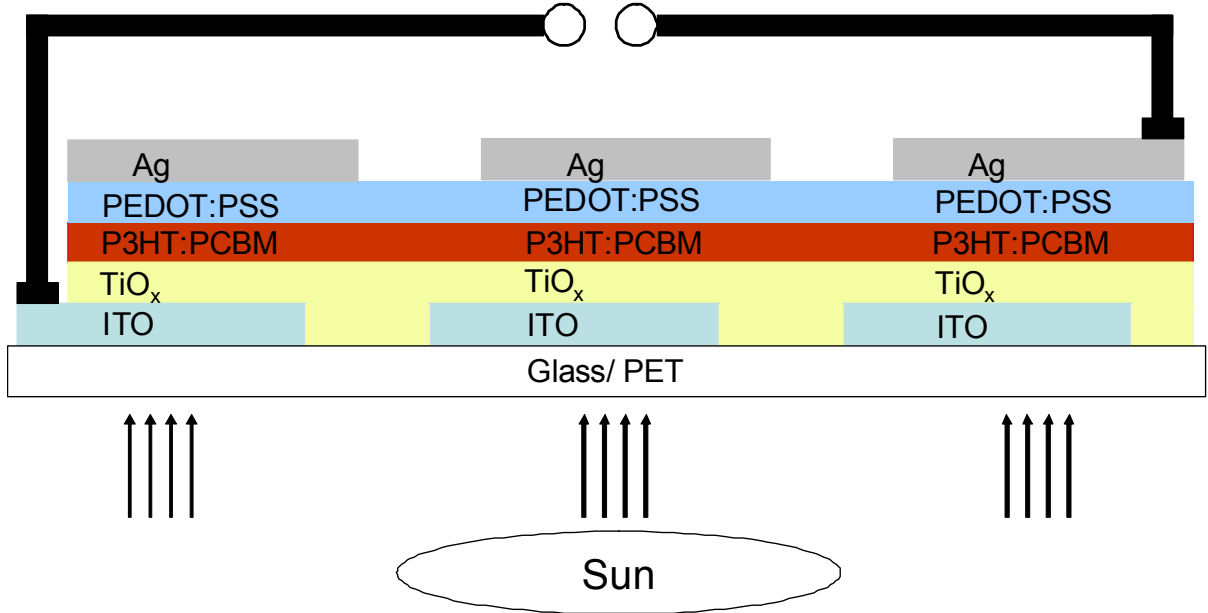


Figure 2-11: Schematics of a serially interconnected 3 stripe module. The active areas are defined by the crossover of the ITO electrode with the Ag electrode. The Ag electrode is connected to ITO electrode of the next cell.

2.5 Measurement Methods

In this subchapter relevant measurement and characterization methods for OPV cells used in this work are presented. J-V measurements, dark lock-in thermography (DLIT), ultraviolet photoelectron spectroscopy (UPS), x-ray photoelectron spectroscopy (XPS) and light beam induced current (LBIC) measurement methods are presented.

2.5.1 Current-Voltage Measurements

To measure the J-V characteristics, a voltage sweep is performed and for every voltage the current from the organic solar cell is measured. The current is divided by the active area of the solar cell to get the respective current densities in mA/cm² and make results comparable. The J-V characteristics are measured with a Keithley source measurement unit (SMU 2400) controlled by a computer. For illumination at 1 sun a calibrated solar simulator (Steuernagel) is used providing a homogeneous AM 1.5G spectra at 100 mW/cm². Since the spectrum of the metal halogen lamps of the solar simulator does not fully match with the spectrum of the sun the solar simulator is cross-calibrated by external quantum efficiency measurements. The

mismatch factor of the solar simulator and P3HT:PCBM based solar cells is 0.8. The intensity of the solar simulator is adjusted that a P3HT:PCBM based solar cell supplies the expected current density at 1 sun. All measurements at 1sun are carried out using this mismatch factor of 0.8.

For indoor measurements a fluorescent bulb with the light colour of 830 is used. The spectrum of the investigated fluorescent lamp is illustrated in Figure 2-6. The measurement setup is calibrated to an illumination of 500 lx, 1000 lx and 5000 lx. The illumination in lx is defined as the luminous flux per area, i.e. lm/m².²⁶ The illumination is calibrated by a luxmeter of the company Testo (testo 545).

2.5.2 Conductivity Measurements

In this work the conductivity of sol-gel TiO_x and P3HT:PCBM is determined. An ITO coated glass is separated with a laser and then coated with the sol-gel TiO_x formulation or P3HT:PCBM. After that, a voltage is applied between the separated ITO stripes and the current is measured as schematically shown in Figure 2-12.

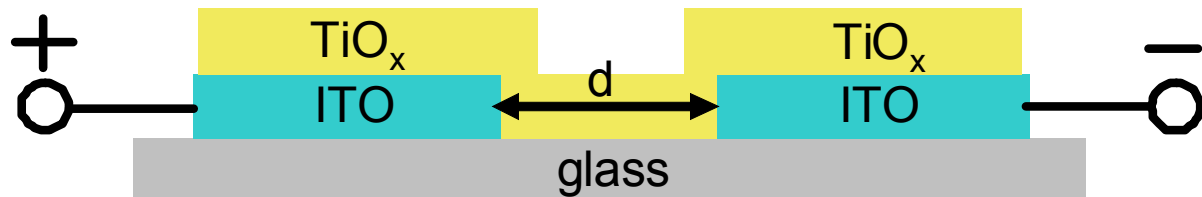


Figure 2-12: Schematic illustration of the principle of the conductivity measurement.

The conductivity can be calculated according to

$$\sigma = \frac{I}{V} \cdot \frac{d}{A} \quad (2.6)$$

where σ is the conductivity, V the applied voltage, A the area (layer thickness times length of the separated ITO strips), d the distance between the ITO strips and I the current.

The use of a laser for structuring the ITO glass allows increasing the sensitivity by reducing the spacing d down to 70 µm. The length of the separated ITO strips is increased to 75 cm in an interdigitated contact structure to further increase the strength of the signal.

2.5.3 Dark Lock-In Thermography

Dark lock-in thermography (DLIT) is used to visualize temperature differences of surfaces. The lock-in technique allows to reduce stochastic noise, suppress DC components and to get the phase information of the measured IR signal. This increases the sensitivity of the DLIT setup to temperature differences in the range of μK compared to several mK without lock-in technique. Therefore heat has to be generated periodically within the OPV cell. In DLIT this heat is generated by applying a voltage to the OPV cell which is periodically modulated with the lock-in frequency f_{li} . The electrical power applied to the OPV cell results in the production of heat with the frequency f_{li} which diffuses through the cell in periodic waves. The temperature rise ΔT of a body upon adding the amount of heat ΔQ by introducing the electrical power P_{el} in the time period from t_0 to t_1 is defined as:

$$\Delta T = \frac{\Delta Q}{c \cdot m} = \frac{1}{c \cdot m} \int_{t_0}^{t_1} P_{el}(t) dt \quad (2.6)$$

where c is the specific heat capacity of the body and m is its mass. The thermal diffusion length Λ of an ideal point source is

$$\Lambda = \sqrt{\frac{\lambda}{\rho_d \cdot c \cdot f_{li} \cdot \pi}} \quad (2.7)$$

where λ is the thermal conductivity and ρ_d is the density of the sample. The increase in f_{li} enhances the lateral resolution of the heat source by reducing the thermal diffusion length. However, with increasing f_{li} , the P_{el} applied to the cell and therefore ΔT are reduced. Therefore, for estimating the size and shape of the heat source a high f_{li} is preferable while for the detection of little inhomogeneities in temperature a low f_{li} is preferable. Figure 2-13 presents the schematics of the DLIT measurement setup. A power supply unit provides the electrical amplitude modulated signal which provides P_{el} to the OPV cell. A function generator (Agilent 33120A) provides a rectangular signal which varies between 0 V and the adjusted voltage amplitude. The IR radiation is detected by an IR camera (IR-camera Taurus 110k SM pro from IRCAM GmbH)²⁸ controlled by a PC. The detector (HgCdTe) is cooled to 80 K. It is sensitive to IR radiation in the range of 2 μm to 5 μm . The detector has a size of 384 * 288 pixels. During one lock-in period, several images are taken and each pixel is weighted by the harmonic correlation functions, the sine and cosine. Adding the images weighted by the sine function of one lock-in period results in the “in phase image” S_0 .

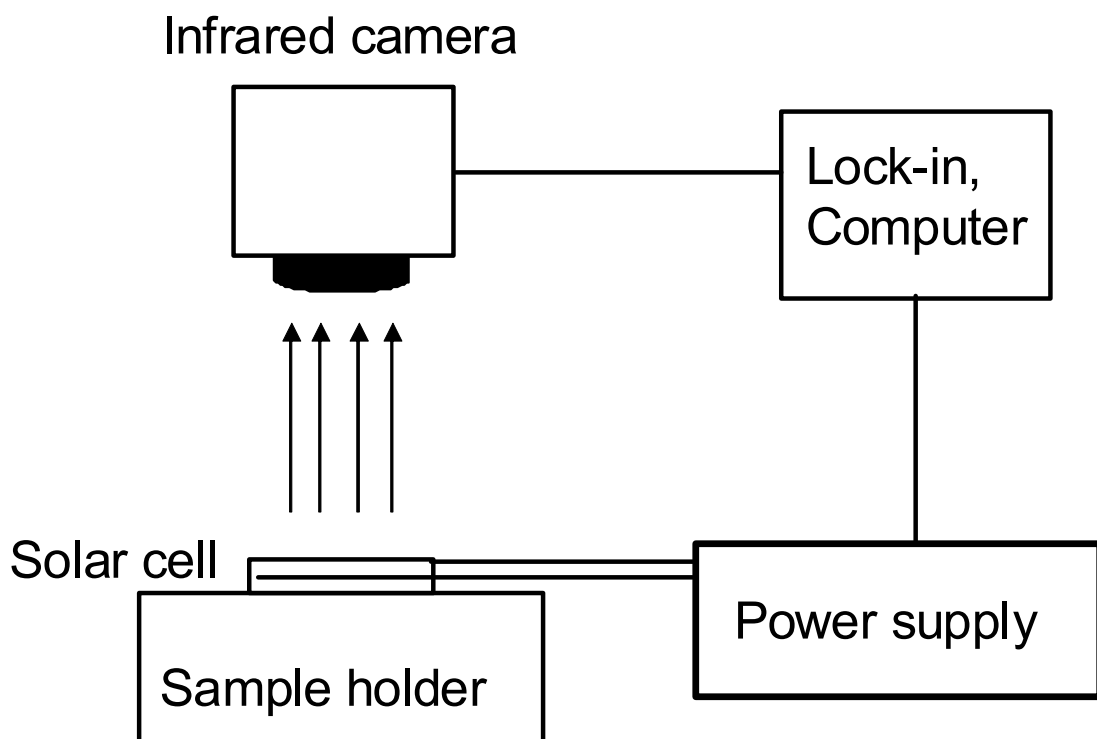


Figure 2-13: Schematic illustration of the DLIT measurement setup.

Adding the images weighted by the cosine function of one lock-in period results in the “90° phase shifted” image S_{90} .

The amplitude signal discussed in this work is obtained from the S_0 and S_{90} image by adding the values of the corresponding pixels (S_{0A} , S_{90A}) as follows:

$$A = \sqrt{(S_{0A})^2 + (S_{90A})^2} \quad (2.8)$$

A more detailed description on DLIT can be found in literature.^{29,30}

2.5.4 Light Beam Induced Current Measurements

The light beam induced current (LBIC) technique measures the local photocurrent of an OPV cell. A mapping over the whole OPV cell results in a map of the local photocurrent. The light source is a green laser wavelength 532 nm which is focused on the OPV cell by different magnification optics. The focal diameter of the laser beam is in the range of a few microns. For mapping, the substrate is moved and the position of the laser spot is fixed. With a lock-in

amplifier the corresponding current to each illuminated point is detected. Lock-In technique is used since the measured currents are in the range of nA.

2.5.5 Ultraviolet and X-Ray Photoelectron Spectroscopy

Ultraviolet photoelectron spectroscopy (UPS) and x-ray photoelectron spectroscopy (XPS) are used to analyze the surface chemistry of materials - to determine the elemental composition, as well as the chemical and electronic structure of the investigated materials. In order to analyze the surface, it is irradiated by UV radiation or x-rays. The number and kinetic energy of the electrons that escape from the solid are measured. The binding energy E_b of the electrons to the solid is determined from their kinetic energy E_k after expulsion from the solid by the photon of energy $h\nu$:

$$E_b = h \cdot \nu - E_k + \Delta\Phi \quad (2.9)$$

where $\Delta\Phi$ is the difference in the work functions between the detector material and the sample. Surface charges are neglected. Each element is characterized by a specific range of electron binding energies. Within this range, the binding energy varies with the chemical environment of the element in the sample. The detection depth is in the range of 1 nm to 10 nm^{31,32} and the analyzed area has a size of a few cm². For UPS measurement the HeI line with energy of 21.2 eV is used. For XPS the Mg-K α line with energy of 1253.6 eV³³ is used. XPS measurements are carried out in a Specs/MAX 200 Ultra High Vacuum system at 10⁻⁹ mbar range and at room temperature.

3 Review on Interface Materials and their Function

In this chapter a literature review of the recent progress in the development and understanding of interface materials for OPV is presented. The proper choice of interface materials is a must for highly efficient and stable OPV devices and has become a significant part of the OPV research today. Interface materials do not only provide selective contacts for carriers of one sort, but can also determine the polarity of OPV devices, be intrinsically conductive layers, affect the open-circuit voltage, and act as optical spacers or protective layers. In this chapter both inorganic and organic interface materials are discussed with respect to their function in the OPV device.

In the first part of this chapter the general concepts of OPV related to interfacial layers as well as the function of interfacial layers are discussed. In the second part an overview of the materials reported in literature is presented including metals, dipole layers, n- and p- type organic and inorganic materials. In some parts, findings and results from organic light emitting diodes (OLEDs) are added.

3.1 Theory of Contact Formation Active Layer/Interfacial Layer

Interface materials are applied between the photoactive layer, i.e. donor and acceptor materials, and the electrode materials. The understanding of the function of those interfacial layers, i.e. metals, metal like materials, organic materials and combinations thereof, and especially of the resulting band alignment between electrode, interfacial layer, and active layer is essential for the proper choice of such interfacial materials. The integer charge model is developed for OPV devices and found to be valuable for most interfaces which are relevant to OPV.^{34,35} This theory predicts Fermi level pinning of a conducting interfacial layer to the organic semiconductor until equilibrium is reached when spontaneous charge transfer between these two layers is possible. In case of no charge transfer between the two layers, no Fermi level pinning takes place.

Figure 3-1 presents experimental results on the energy level alignment between the low-band-gap polymer polyfluorene APFO-Green1 and a conducting substrate. The substrate

work function is varied between 3.0 eV and 5.5 eV and the resulting band alignment is then measured when APFO-Green 1 is coated on the substrate.

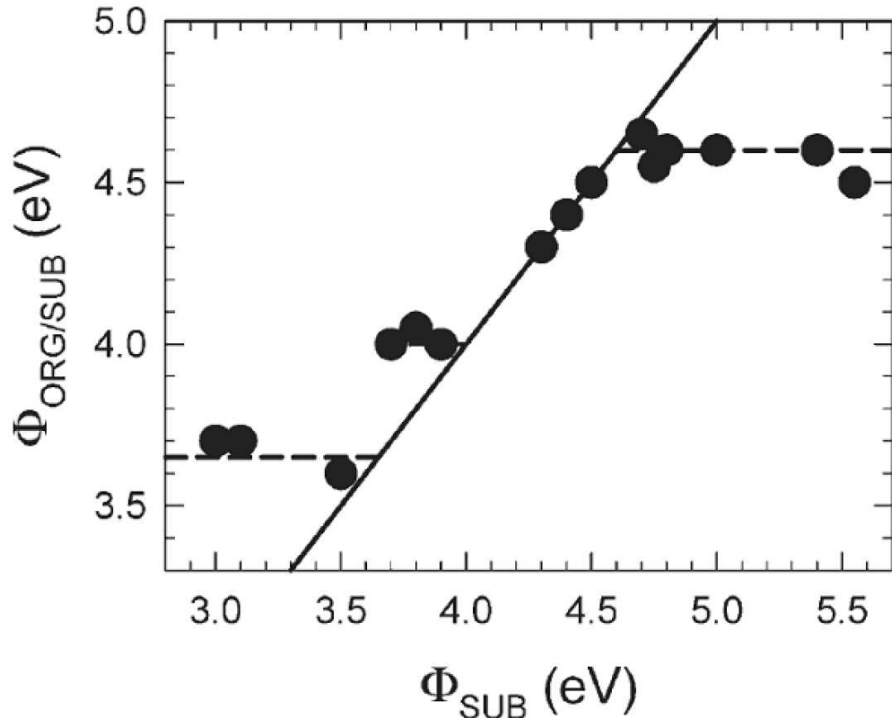


Figure 3-1: Dependence of the work function of molecule-coated substrates ($\Phi_{\text{org/sub}}$) on the work function of bare substrates (Φ_{sub}) for APFO-Green1.³⁴ The solid line is added as a guide to eye, illustrating the slope = 1 dependence as expected for vacuum level alignment. The dashed lines are added as guides to the eye, illustrating the slope = 0 dependence expected for a Fermi-level pinned interface. Adapted with permission from [³⁵]. Copyright 2009, Wiley VCH.

In this review we compare the absolute values of the work function. For substrate work functions larger than 4.6 eV and lower than 3.6 eV, the Fermi level of the substrate is pinned to APFO-Green1, i.e. to 3.6 eV and 4.6 eV, respectively. In the integer charge model these states are called positive ($E_{\text{ICT+}}$) and negative ($E_{\text{ICT-}}$) integer charge-transfer states. $E_{\text{ICT+}}$ is defined as the energy which is required to extract one electron from the polymer/molecule to produce a thermally fully relaxed state. $E_{\text{ICT-}}$ is defined as the energy which is gained when one electron is added to the molecule/polymer in order to produce a fully relaxed state. These states differ from the lowest unoccupied molecular orbital (LUMO) and highest occupied molecular orbital (HOMO) of the organic semiconductor. In between these states a linear correlation between the substrate work function (Φ_{sub}) and the measured work function

organic/substrate ($\Phi_{\text{org}/\text{sub}}$) with a slope of 1 is found. The system describes a full “Mark of Zorro” dependence. The Fermi level pinning of the conducting substrate to the charge transfer states is also observed experimentally for several other organic semiconductors and fullerenes, including P3HT and C₆₀.^{36,35}

The “Mark of Zorro” dependence is schematically depicted in Figure 3-1 and described in the integer charge model as follows: Depending on the position of the Fermi level of the substrate with respect to E_{ICT^+} and E_{ICT^-} , three scenarios can be distinguished which are schematically depicted in Figure 3-2:

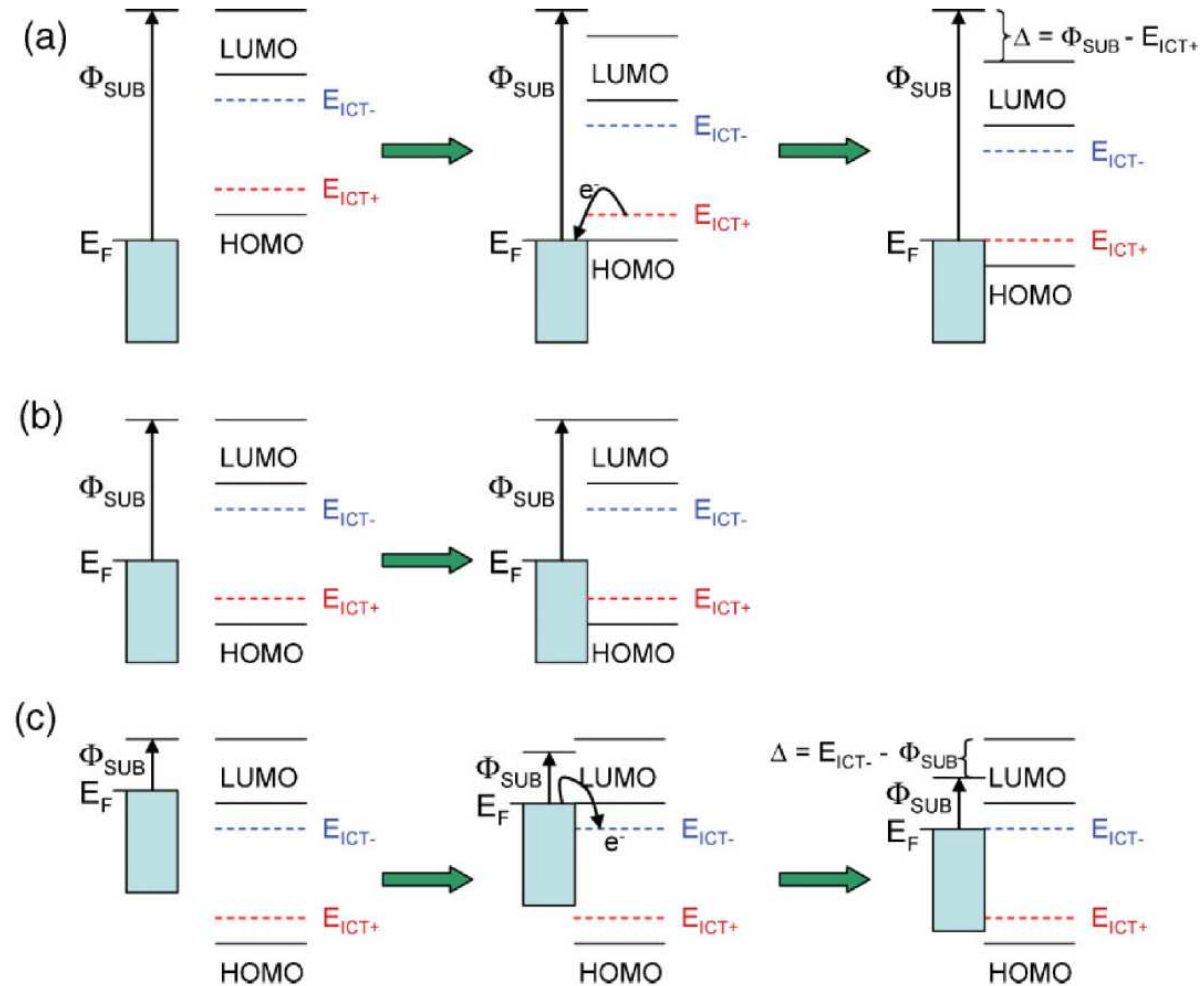


Figure 3-2: Schematic illustration of the evolution of the energy-level alignment when a pi-conjugated organic molecule or polymer is physisorbed on a substrate surface when a) $\Phi_{\text{sub}} > E_{\text{ICT}^+}$: Fermi-level pinning to a positive integer charge-transfer state, b) $E_{\text{ICT}^-} < \Phi_{\text{sub}} < E_{\text{ICT}^+}$: vacuum level alignment, and c) $\Phi_{\text{sub}} < E_{\text{ICT}^-}$: Fermi-level pinning to a negative integer charge-transfer state. The charge-transfer-induced shift in vacuum level, Δ , is shown where applicable. Adapted with permission from [35]. Copyright 2009, Wiley VCH.

- (a) When the substrate work function is larger than E_{ICT+} of the polymer, electrons will flow from the polymer chain to the substrate and the Fermi level of the substrate will be pinned to E_{ICT+} of the polymer, due to the high density of states in the polymer at E_{ICT+} .
- (b) When the Fermi level of the substrate is in between E_{ICT+} and E_{ICT-} , the vacuum levels align and no Fermi level pinning occurs, .
- (c) When the substrate work function is smaller than E_{ICT-} of the polymer, electrons will flow from the substrate to E_{ICT-} of the polymer and the Fermi level of the substrate will be pinned to E_{ICT-} of the polymer.³⁵

Analogously, the integer charge model can be transferred to stacked multilayer systems. A more detailed description of this model including physisorption, chemisorption and the induced density of states model is given in the review of Braun et. al.³⁵ and others.³⁷⁻³⁹

3.2 Purpose of Interfacial Layers

Interfacial layers enable the unipolar extraction of photo-generated carriers from the active layer to the electrodes. Photons are absorbed in the active layer by the photosensitive layer, e.g. a polythiophene and a fullerene composite, excitons are created and split into free carriers at the donor-acceptor interface. Electrons are transported to the cathode by the acceptor material, holes to the anode by the donor material and get extracted to the electrodes by the interfacial layer. The interface which is formed between the active layer and the electrodes is essential for highly efficient and stable OPV devices. The main functions of interface materials are:

- (1) Adjust the energetic barrier height between the active layer and the electrodes.
- (2) Formation of carrier selective contact.
- (3) Determine the polarity of the device.
- (4) Prohibit a chemical or physical reaction between the polymer and electrode.
- (5) Act as optical spacer.

3.2.1 Impact on the Open-Circuit Voltage

Interface materials enable the electrical contact between the active layer and the electrode materials for charge carrier extraction. Thus, the impact of the interfacial layers on V_{oc} of a

device needs to be investigated more closely. Two models are discussed extensively in literature, the metal-insulator-metal (MIM) model and the Ohmic contact model. The MIM model claims that V_{oc} originates from the work function difference of the electrode materials. This model is applied to non-ohmic contacts where no Fermi level pinning between cathode - donor and anode - acceptor occurs. The MIM-model is supported by experiments of Mihailetti et. al., who report that for non-ohmic contacts V_{oc} is determined by the work function difference of the electrodes. The cathode materials are varied while the anode material in all experiments is ITO/PEDOT:PSS. When the anode material is varied from Ag to Pd, the V_{oc} is reduced from 0.59 V to 0.398 V, compared to a difference in the work functions of the investigated cathodes of 0.29 V. In this regime V_{oc} correlates linearly with the work function differences of the investigated cathodes with a scaling factor close to 1. The scaling factor is defined as the quotient of the difference of V_{oc} and the difference of the work functions for the investigated cathode materials. Pd forms a non-ohmic contact to PCBM.⁴⁰

For ohmic contacts the situation is different. In chapter 3.1 it is discussed that Fermi level pinning occurs when the substrate work function exceeds E_{ICT^+} and is below E_{ICT^-} , respectively. These results have been experimentally confirmed for P3HT and C60, the fruit fly semiconductors for OPV. The relevant interfaces are anode-donor and cathode-acceptor because electrons are transported by the acceptor and holes by the donor material in OPV cells. Therefore, E_{ICT^+} , E_{ICT^-} and the respective band alignment at the interfaces formed between semiconducting polymer/interfacial layer/electrode are relevant for the open-circuit voltage of the OPV device. Thus, the highest possible open-circuit voltage is the difference of E_{ICT^+} of the donor and E_{ICT^-} of the acceptor, independent of the work function of the interfacial material, provided that Fermi level pinning occurs. Interfacial materials, whose Fermi level is located between E_{ICT^+} and E_{ICT^-} , reduce the V_{oc} . For instance, the origin of V_{oc} is investigated in detail for poly(2-methoxy-5-(3',7'-dimethyloctyloxy)-1,4-phenylenevinylene) (MDMO-PPV) blended with highly soluble fullerene derivatives as active layer. The investigated structure is ITO/PEDOT:PSS/MDMO-PPV:Fullerene/metal electrode with the fullerene and the electrode as varying parameter. The work function of the metal electrode, i.e cathode, is varied from 5.1 eV for Au to 2.87 eV for Ca/Ag. This resulted in an increase of V_{oc} from 0.650 V to 0.814 V. The corresponding scaling factor is estimated to 0.1 or lower. (Figure 3-3) This contact behavior is explained by the Fermi level pinning

mechanisms which occur for ohmic contacts. In contrast, for non-ohmic contacts, e.g., in the case of Palladium, it is found that the V_{oc} is influenced by the work function of the interface materials.⁴⁰

In another experiment, the LUMO of the acceptor is varied and its influence on V_{oc} is investigated. It is found that raising the LUMO of the acceptor by 160 mV (reduction potential changed from -0.53 V for N-3-[2-ethylhexyloxy]benzyl ketolactam to -0.69 V for PCBM vs. normal hydrogen electrode) increases V_{oc} from 0.56V to 0.76V. The corresponding scaling factor is close to 1 and proofs that V_{oc} is controlled by the LUMO of the acceptor as depicted in Figure 3-3.⁴¹

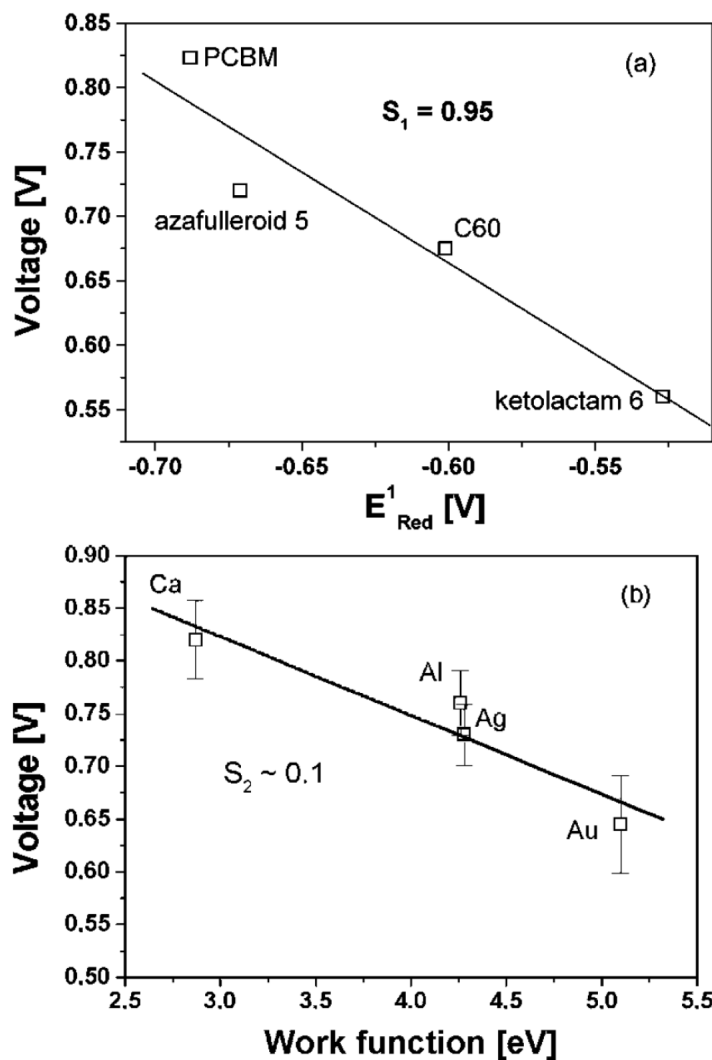


Figure 3-3: a) V_{oc} versus acceptor strength and b) V_{oc} versus electrode work function. The slopes S_1 and S_2 of the linear fits of the experimental data are given inside the figures. Adapted with permission from [41]. Copyright 2001, Wiley VCH.

Figure 3-4 illustrates experimental results on the dependence of the V_{oc} to the HOMO position of the donor polymer, i.e. the onset of oxidation, for 26 different donors. The linear fit of the measured points has a slope equal to 1 which proves that V_{oc} correlates linearly with the HOMO of the donor⁴².

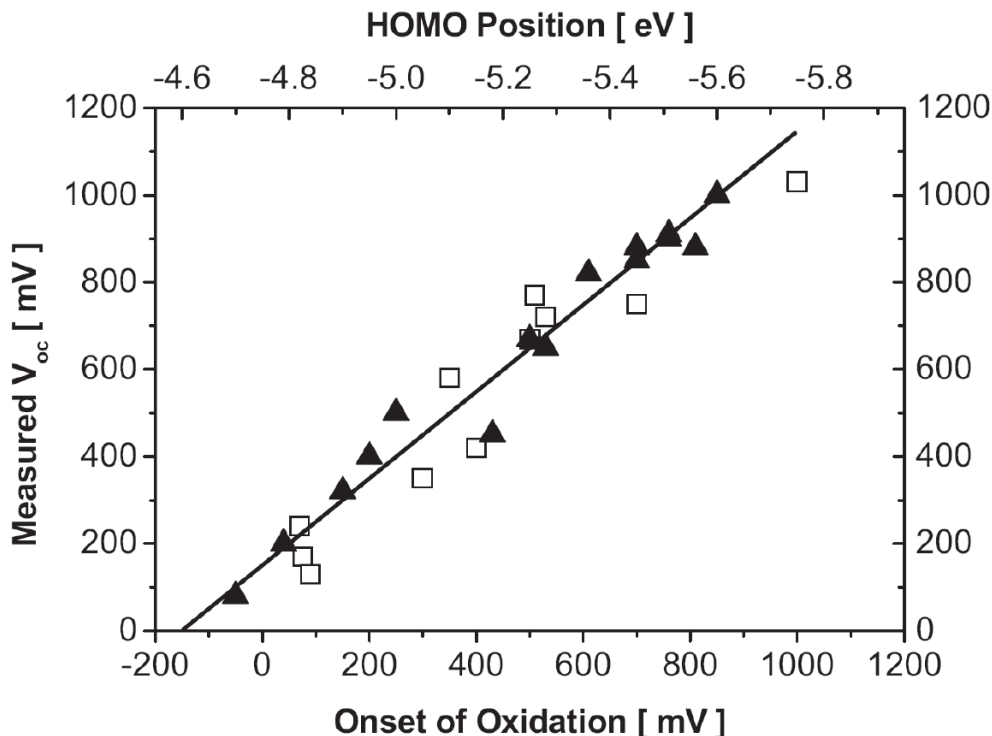


Figure 3-4: V_{oc} of different bulk-heterojunction solar cells plotted versus the oxidation potential/HOMO position of the donor polymer used in each individual device. The straight line represents a linear fit with a slope of 1. Adapted with permission from [42]. Copyright 2006, Wiley VCH.

In conclusion V_{oc} correlates with the HOMO of the donor and the LUMO of the acceptor in the case of ohmic contacts - the Fermi levels of the interfacial and electrode materials are pinned to E_{ICT+} of the donor at the anode and E_{ICT-} of the acceptor at the cathode. For non-ohmic contacts V_{oc} is influenced by the interface materials - the upper limit of V_{oc} is the difference of E_{ICT+} of the donor and E_{ICT-} of the acceptor.⁴³ V_{oc} values exceeding beyond these limits have not been observed to the best of our knowledge.

3.2.2 Polarity of the Device

Two different geometries of OPV cells, the normal and the inverted structure, are reported in the literature (Figure 3-5), depending on whether the bottom electrode forms the anode or the cathode. The bottom electrode is the transparent electrode, e.g. ITO, on which the OPV cell is constructed. In the normal structure holes are extracted at the bottom electrode, in the inverted structure holes are extracted at the top electrode. The active layer of an OPV cell in many cases is formed by a bulk-heterojunction where the donor- and an acceptor material are blended. In an ideal case the donor and acceptor materials are distributed equally throughout the active layer. Therefore, a bulk-heterojunction does not have a preferential direction to extract electrons or holes to one side of the solar cell. The interface materials/electrodes which are sandwiching the active layer constitute the cathode and the anode of the OPV cell, i.e. the interfacial layer/cathode with the larger work function forms the anode. Depending on the thickness and type of the used interface materials, the polarity of the device may become independent of the used electrode materials. For instance, PEDOT:PSS and TiO_x are utilized in the normal as well as in the inverted structure. TiO_x determines the cathode and PEDOT:PSS the anode of an OPV cell, independent of the used electrode materials (see Figure 3-5).

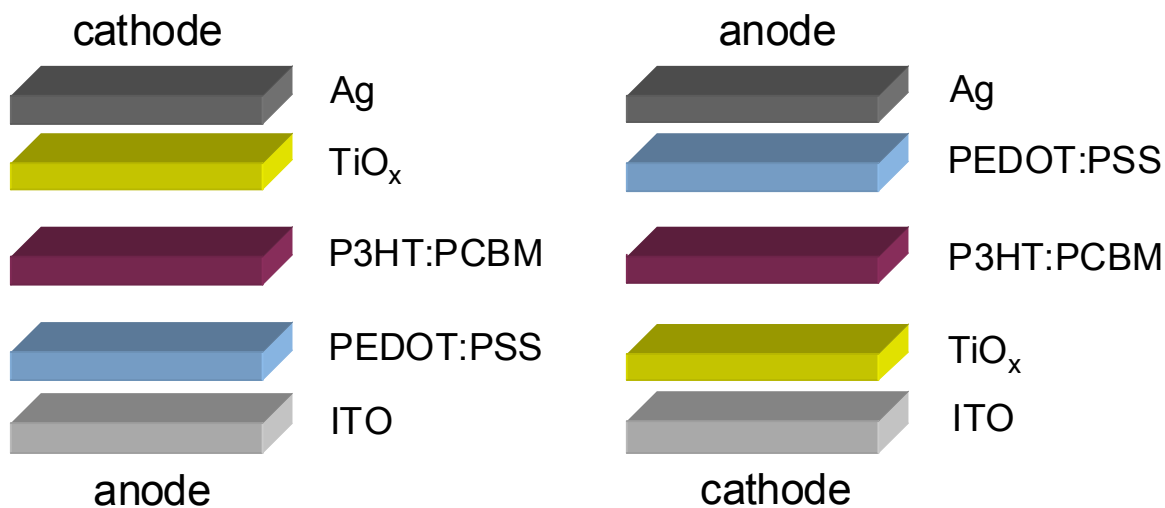


Figure 3-5: Device structure in the normal (left) and inverted structure (right).

Figure 3-6 presents the J-V-characteristics of devices in the normal structure (ITO/PEDOT:PSS/P3HT:PCBM/LiF/Al) and inverted structure

(ITO/TiO_x/P3HT:PCBM/PEDOT:PSS/Au). In both devices PEDOT:PSS is used as the anode material, the cathode, however, is either given by the LiF/Al contact or by the ITO/TiO_x layer. Both architectures give quite comparable performance, the differences in device performance are usually explained with a vertical phase separation^{44,45} of the acceptor and donor, which may be more favorable for one structure versus the other, but not sufficient to determine the polarity of the OPV device.⁴⁶

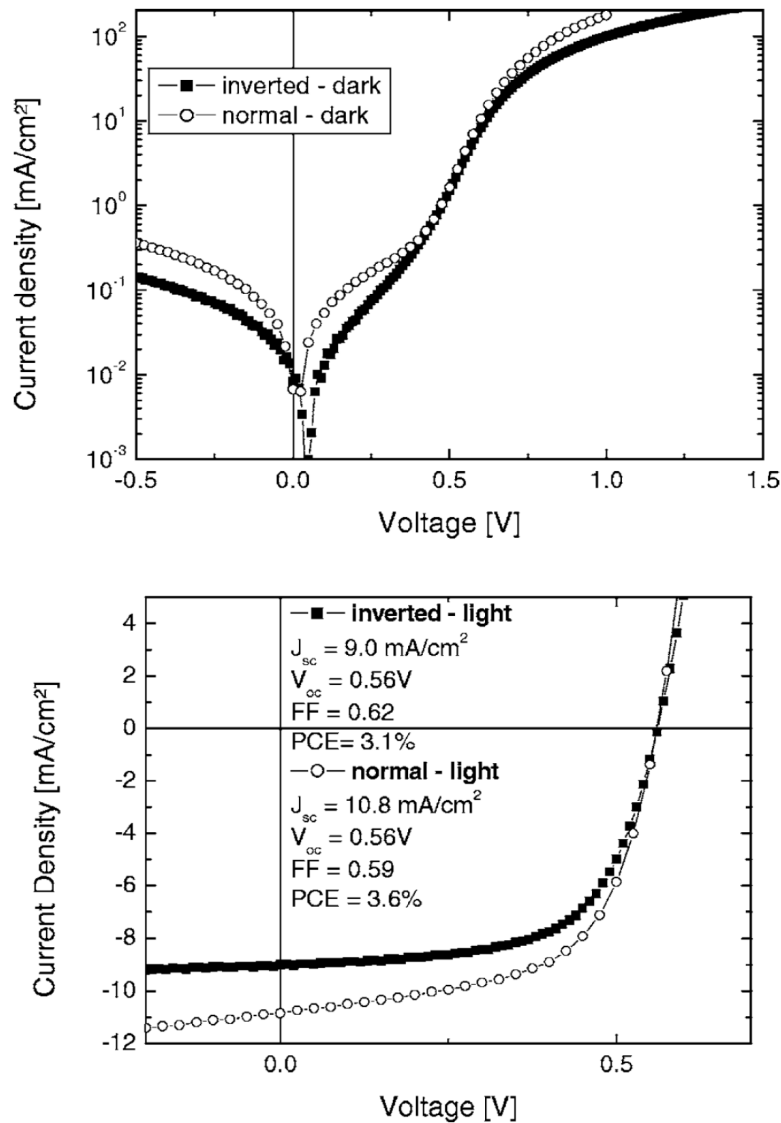


Figure 3-6: J-V curves in a semilogarithmic representation for the normal (open Circles) and inverted (solid squares) OPV in the dark (upper plot) and under illumination (bottom plot). Adapted with permission from [46]. Copyright 2006 American Institute of Physics.

3.2.3 Electrode Materials – Conductive Layers

Some interfacial layers act as both, interfacial layer and electrode material. A low sheet resistance of electrode materials ($<10 \Omega/\text{sq}$) is essential to transport the photo-generated carriers with little losses. Many metals are typically utilized for the non-transparent back-contact. The materials for the transparent front electrodes are much more limited. ITO is the most prominent transparent electrode for OPV devices. ITO provides sufficiently high transmittance (~90%) and low sheet resistance (~ $10 \Omega/\text{sq}$). ZnO doped with group III elements, i.e. B⁴⁷, Ga⁴⁸⁻⁵⁰ and Al^{51,52} are alternative transparent electrode materials. Other approaches to replace ITO are carbon nanotubes⁵³, graphene⁵⁴, highly conductive polymers⁵⁵, metal grids,⁵⁶ metal nano-meshes⁵⁷, optically thin metal layers alone⁵⁸ or thin metals in combination with other metal oxides.⁵⁹

3.2.4 Optical Spacer

Most OPV devices consist of a transparent front electrode and a non-transparent reflecting back electrode. Light enters the OPV cell through the transparent electrode and is reflected at the non-transparent electrode. Therefore, the light passes the active layer twice and a standing wave is formed, with the electrical field strength $|E| = 0$ at the reflecting electrode and its maximum somewhere in the bulk, depending on the refractive index and the thicknesses of the layers. The absorption of light depends on the electrical field strength of the light which depends on the phase. For OPV cells with a photoactive layer thickness in the range of 100 nm, interference effects may become important. The absorbing active layer thickness needs to be correlated to the mobility-lifetime product of the photo-generated charge carriers within the active layer, so that most photo-generated charge carriers can reach the electrodes. The optical spacer effect is a concept to optimize the absorption within the active layer. A transparent layer is inserted between the reflecting electrode and the active layer. Depending on the thickness and refractive index of the transparent optical spacer layer, the absorption maximum can be shifted. A layer thickness of a few 10 nm might be enough to improve the absorption within the active layer significantly. Once optimized, such an optical spacer layer can help to improve the short-circuit current of an OPV device, specifically for thin film devices which otherwise would not absorb all light in a single pass.⁶⁰ An example for an OPV cell structure with and without optical spacer is

glass/ITO/PEDOT/P3HT:PCBM/TiO_x/Al and is given in Figure 3-7. Here, TiO_x acts as optical spacer⁶¹⁻⁶³.

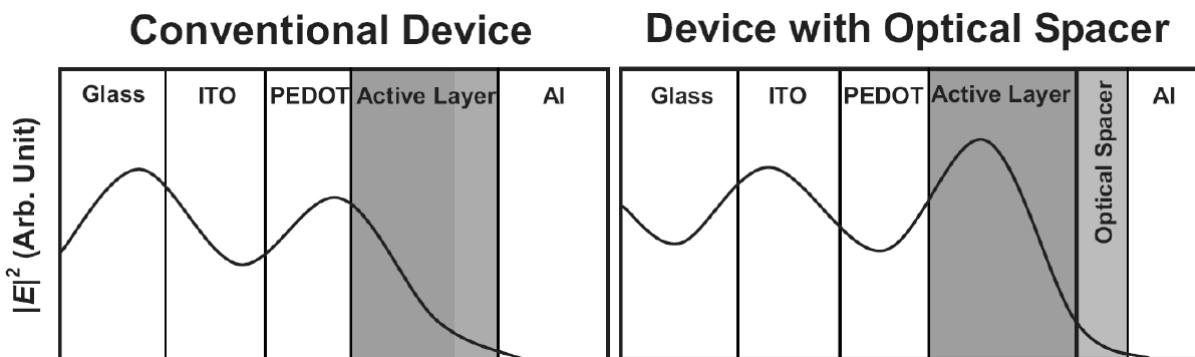


Figure 3-7: Schematic representation of the spatial distribution of the squared optical electric field strength $|E|^2$ inside the devices with a structure of ITO/PEDOT/active layer/Al (left) and ITO/PEDOT/active layer/optical spacer/Al (right). Adapted with permission from [61]. Copyright 2006, Wiley VCH.

3.2.5 Protective Layer between Polymer and Electrode

An interfacial layer protects the organic layer from physical or chemical interaction with the electrode materials. For example, metals are often used as electrode material providing the conductivity needed to extract photo-generated carriers. The diffusion of metal atoms into polymeric layers during the thermal evaporation process causes shunting or electrical shorting of the organic devices and limits their lifetime.⁶⁴⁻⁶⁶ The protection of the active layer from oxygen and water of the atmosphere by an interfacial layer of TiO_x is also reported as an interesting approach to improve lifetime.⁶⁷

3.2.6 Formation of Carrier Selective Contact and Exciton Blocking Layer

Since excitons and carriers are created in the entire active layer, interfacial layers form selective contacts and hinder excitons and carriers to recombine at the electrodes.⁶⁸⁻⁷² Thus, interfacial layers form a barrier for carriers of one sort, and pass by the carriers of the opposite sort. For instance, the cathode enables or facilitates extraction and injection of electrons, but blocks holes. Interfacial layers which act as an exciton blocking layer have a bandgap higher than the one of the acceptor and donor of the active layer. The transfer of

excitons through the interfacial layer is not possible without supply of additional energy. Therefore, an interfacial layer can act as exciton blocking layer.

3.3 Materials Overview for Interfacial Layers

Some materials discussed in this review can be used as both, electrode material and interfacial layer. Other materials, e.g. when the conductivity is not sufficient, are sole interface materials. In the following the most prominent interface materials will be reviewed, categorized in conducting layers, semiconducting layers and interface dipole layers. Also we will distinguish between cathode (n-type) and anode (p-type) materials.

In organic electronics it is demonstrated that chemical doping with organic and inorganic materials can modify material properties such as conductivity and the Fermi level.⁷³⁻⁷⁷ For efficient n-type doping the HOMO level of the dopant or Fermi level must be lower than the LUMO level of the material that has to be doped. For p-type doping the LUMO level of the dopant has to be higher than the HOMO level of the material to be doped.

3.3.1 Metals

Metals can be thermally evaporated in optical thick and thin layers to form a non-transparent or transparent electrode or/and interfacial layer. Especially for Ag which is widely used, several deposition methods have been successfully demonstrated. For instance, spray-coating of Ag nanoparticles⁷⁸, Ag-pastes and transparent Ag nanowire meshes⁷⁹ have been reported to be feasible for solution processing, which makes these materials attractive for roll-to-roll printing processes.

Al, Mg/Ag, Ca/Al, Ca/Ag, Ba/Al ,Au, Ti are successfully used in OPV devices.⁸⁰ A combination of a low work function metal (Ca, Ba) with Ag or Al is a common way to decrease the work function of the electrode and to prevent Ag and Al atoms from diffusing into the polymeric layer. The work function of these metals ranges from 5.1 eV for Au⁸¹ to 2.7 for Ba⁸¹. Figure 3-8 illustrates experimental results for several electrode materials as cathode in the normal device structure (ITO/PEDOT:PSS/P3HT:PCBM/cathode). V_{oc} , FF and the normalized efficiency is depicted. The pristine metals Al and Ag have the lowest performance while in combination with Mg:Ag, LiF, Ba or Ca the device performance is

clearly improved because these materials decrease the work function of the cathode, act as protection layer and improve the selectivity.

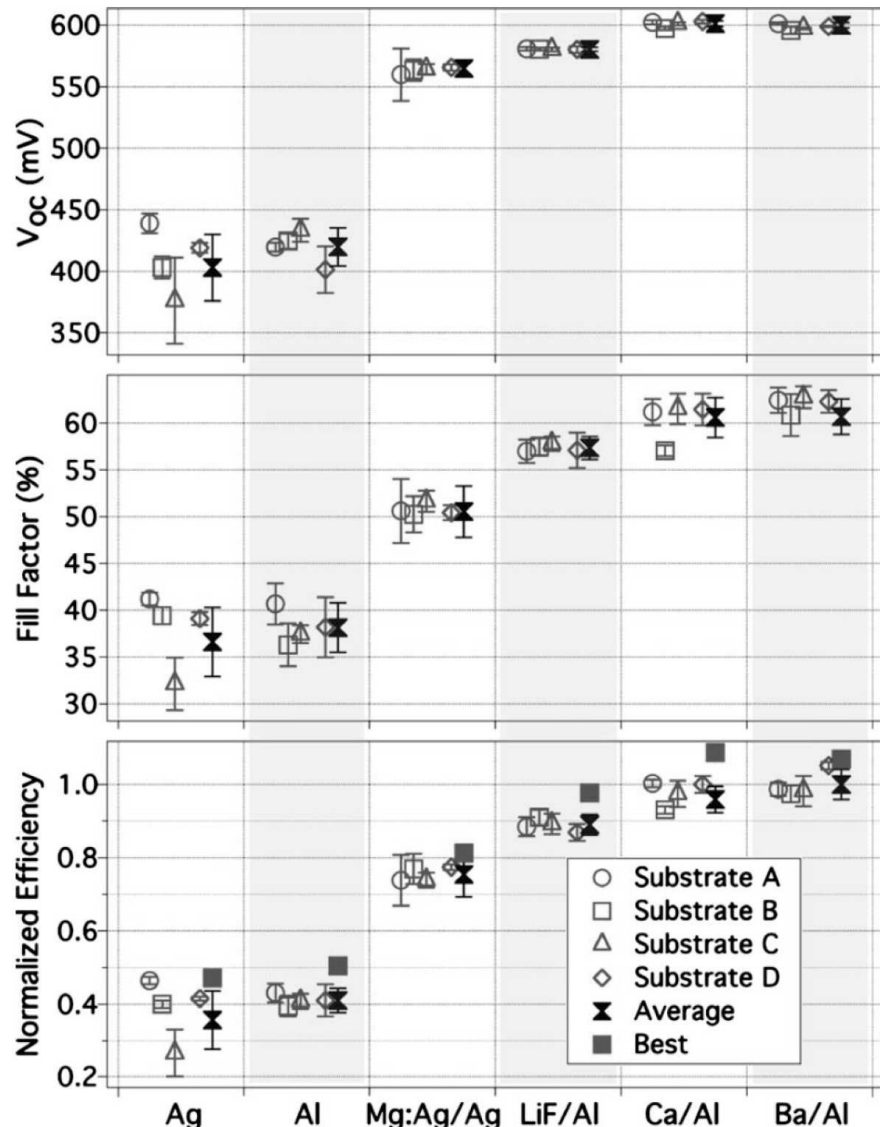


Figure 3-8: V_{oc} , FF, and normalized efficiency vs negative electrode type. Average values are displayed both for individual and groups of substrates (ITO/PEDOT:PSS/P3HT:PCBM/cathode). Error bars denote plus and minus one standard deviation. “Best” efficiency values are for devices made by Reese et al.. Adapted with permission from [80]. Copyright 2008 American Institute of Physics.

Apart from a modification of the work function of the electrode and physical barrier layer, low work function metals have also been used to n-dope organic layers. This is possible when the work function of the metal is smaller than the LUMO of the organic layer, e.g. Mg can

dope C₆₀.⁸² Figure 3-9 gives a comprehensive overview of the work functions of metals and semi-metals.^{83, 81}

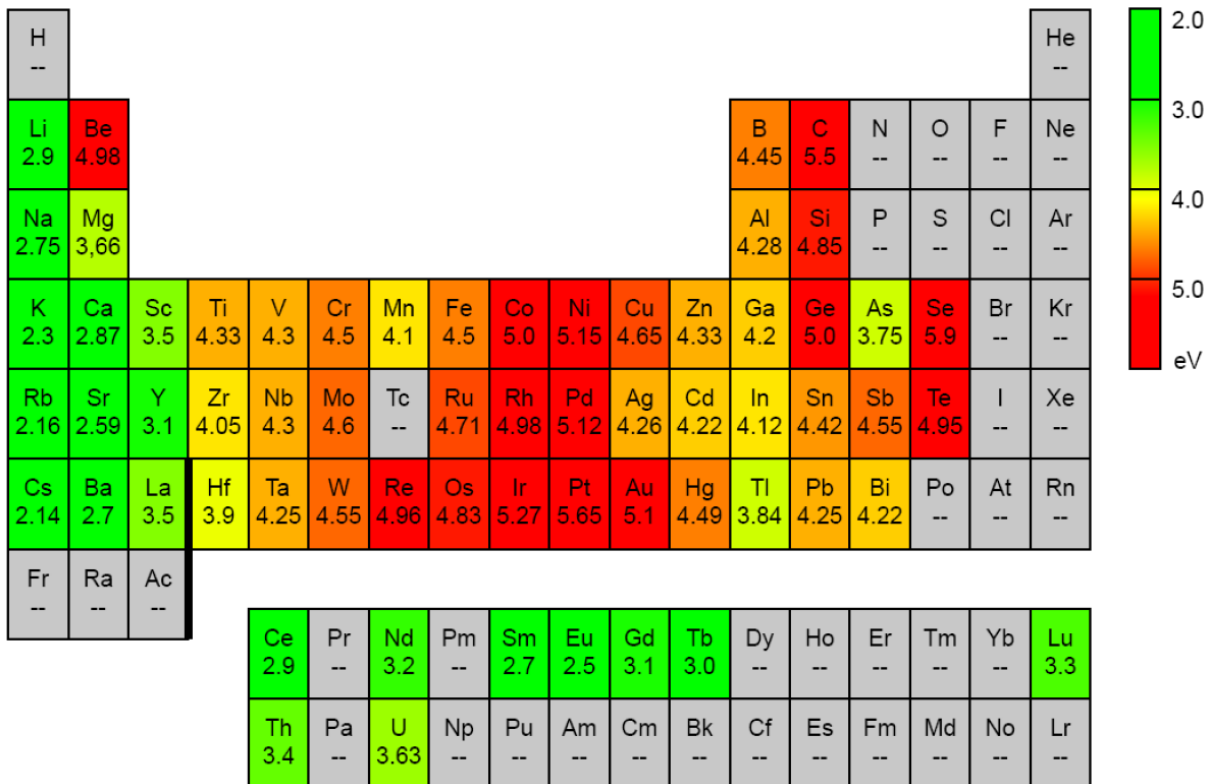


Figure 3-9: Work function of the elementary solids.⁸³ Adapted with permission from [81]. Copyright 1977 American Institute of Physics.

3.3.2 Semiconducting Layers

Many semiconducting interfacial materials are shown to be feasible for OPV applications. We distinguish between inorganic materials (metal oxides) and organic materials, reviewing the most prominent ones. Transparency, i.e. little absorption losses, is a must for efficient OPV devices and allows to deposit thick layers without absorption losses. As such, interfacial materials are often required to be transparent in the visible light spectrum. Moreover, doped semiconducting materials with a high conductivity can be used as transparent electrode material and thick interfacial layers.

3.3.2.1 Inorganic Materials - Metal Oxides

Metal oxides can be p-type and n-type materials, depending on the position of the valence band and conduction band. For a p-type contact material, the valence band of the metal oxide is required to match the HOMO of the polymer. For an n-type material, electron transfer from the LUMO of the acceptor to the conduction band of the metal oxide is required. A wide band gap of the interface material then results in a barrier for carriers of the other sort and enables highly selective contacts. Figure 3-10 summarizes widely used p-type and n-type metal oxides for the P3HT-PCBM donor-acceptor system. As reference, the energetic level of the most common interface material PEDOT:PSS is added.

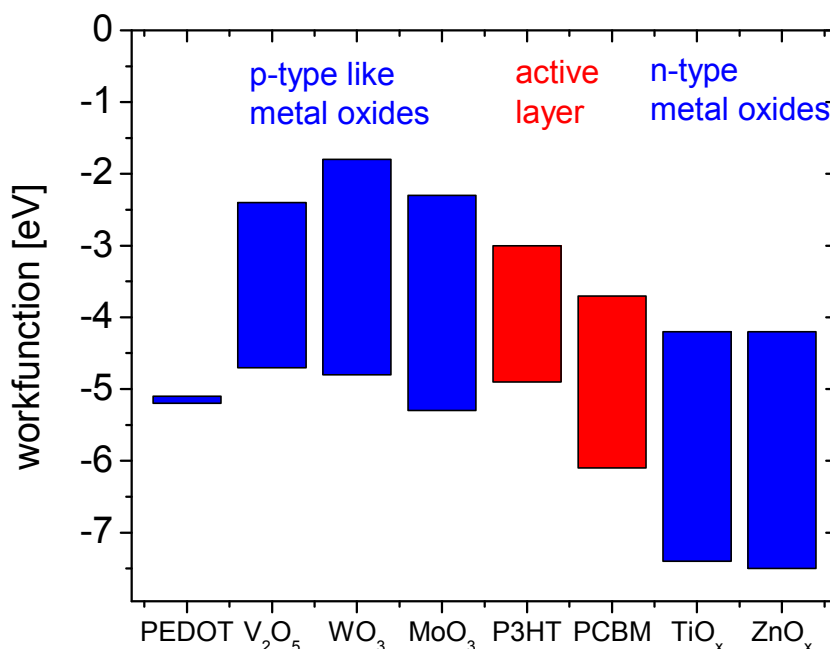


Figure 3-10: Energy level diagram of p-type and n-type metal oxides incorporated in OPVs. As reference the PEDOT:PSS, P3HT and PCBM are added. Values are taken from the references given in sections 3.3.2.1.1 and 3.3.2.1.2.

3.3.2.1.1 P-Type Inorganic Materials

P-type like transition metal oxides have been successfully introduced in OPV. WO_3^{84-86} , NiO^{68} , $V_2O_5^{87-90}$ and $MoO_3^{87,91}$ are such p-type like metal oxides with respect to P3HT.

Shrotriya et. al demonstrated that thermally evaporated transition metal oxides have the potential to replace PEDOT:PSS. They studied different layer thicknesses of V₂O₅ and MoO₃ and compared results of OPV devices without and with PEDOT:PSS as p-type interfacial layer (Table 1).

Table 1: Device operation parameters for devices with different types of anodes fabricated in this study. Adapted with permission from [⁸⁷]. Copyright 2006 American Institute of Physics.

Anode	I_{SC} (mA/cm ²)	V_{OC} (V)	FF (%)	PCE (%)
ITO only	7.82	0.49	51.1	1.96
ITO/PEDOT:PSS (25 nm)	8.95	0.59	59.6	3.18
ITO/V ₂ O ₅ (1 nm)	8.86	0.59	47.5	2.48
ITO/V₂O₅ (3 nm)	8.83	0.59	59.1	3.10
ITO/V ₂ O ₅ (5 nm)	8.54	0.59	57.2	2.88
ITO/V ₂ O ₅ (10 nm)	8.16	0.59	57.9	2.79
ITO/MoO ₃ (1 nm)	8.75	0.53	42.3	1.98
ITO/MoO ₃ (3 nm)	8.86	0.59	58.3	3.06
ITO/MoO₃ (5 nm)	8.94	0.60	61.9	3.33
ITO/MoO ₃ (10 nm)	8.73	0.60	59.8	3.13
ITO/MoO ₃ (20 nm)	8.19	0.58	59.9	2.86

A clear improvement in J_{sc} , V_{oc} , FF and PCE is observed for all investigated metal oxide layer thicknesses compared to OPV devices without p-type interfacial layer (ITO only). Thin layers of metal oxide (1nm) do not cover the entire electrode; too thick metal oxide layers reduce the J_{sc} and FF due to the serial resistance of the interfacial oxide. Excellent results are achieved for the optimized layer thickness of V₂O₅ (3 nm) and MoO₃ (5 nm).⁸⁷ This has been reported for the normal as well as for the inverted structure by various groups.^{92 91 89}, Moreover, it is shown that stacking of PEDOT:PSS with a metal oxide may further improve the device performance.⁸⁶

3.3.2.1.2 N-Type Inorganic Materials

$\text{TiO}_x^{67, 46, 93-96}$ and $\text{ZnOx}^{91, 97-100}$ are well investigated n-type interfacial layers for OPV devices. These materials are transparent in the visible radiation spectrum but absorb UV radiation. The layer thickness of the interfacial layer is tunable without absorption losses in the VIS light and thus can additionally act as optical spacer.⁶¹⁻⁶³

Figure 3-11 illustrates the J-V-characteristics of inverted OPV cells with electrodeposited amorphous (TiO_x) or anatase (TiO_2) titanium oxide as n-type interfacial layers with and without UV irradiation. Without UV irradiation (< 440nm) the PCE of the OPV cell is drastically reduced compared to an OPV cell with UV irradiation. The PCE with and without UV light irradiation depends on the type of TiO_x , amorphous or anatase TiO_x . With UV irradiation the PCE improves to 2.13 % for the amorphous TiO_x and to 2.48 % for the anatase TiO_2 which might be caused by a difference in carrier density.¹⁰¹

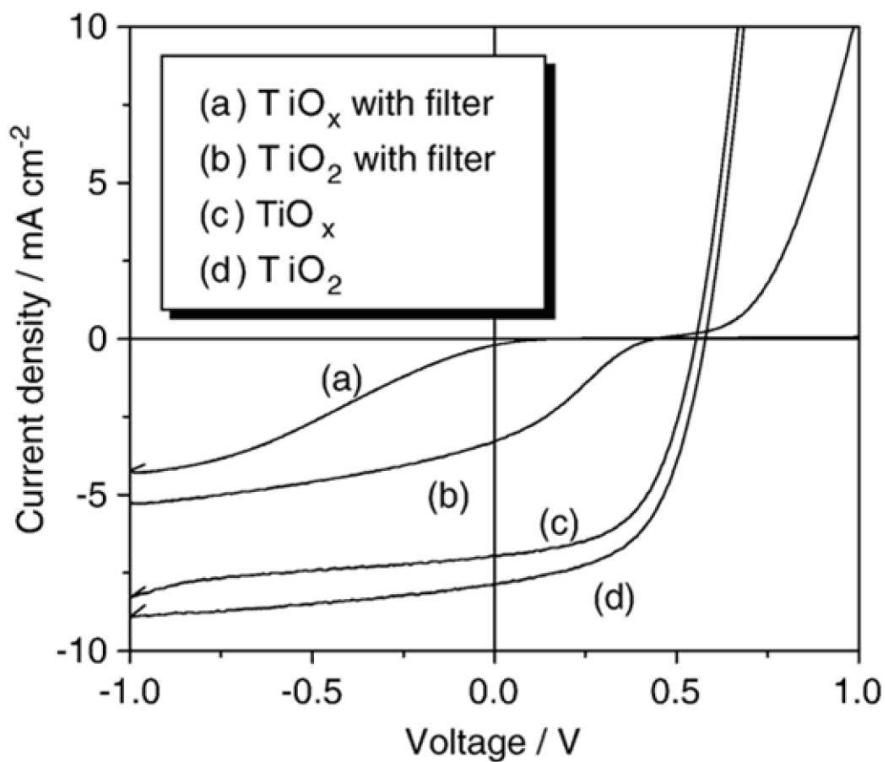


Figure 3-11: Photo I-V curves of the FTO/amorphous $\text{TiO}_x/\text{P3HT:PCBM/PEDOT:PSS/Au}$ and FTO/anatase $\text{TiO}_2/\text{P3HT:PCBM/PEDOT:PSS/Au}$ type solar cells under irradiation of AM 1.5–100 mW/cm² with and without UV filter (440 nm). Adapted with permission from [101]. Copyright 2008 Elsevier.

The design of 3-dimensional structures of metal oxides is another approach to improve the PCE and many groups compare 2-dimensional ZnO layers with 3-dimensional nanostructures¹⁰²⁻¹⁰⁶. The increased interface acceptor/interfacial layer improves the electron transport and is expected to allow for thicker active layers.¹⁰⁷

Mor et. al. presented a vertically oriented TiO₂ nanotube film with P3HT:PCBM infiltrated into the nanotubes as illustrated in Figure 3-12. PCEs as high as 4.1 % are reported in the inverted structure.¹⁰⁸

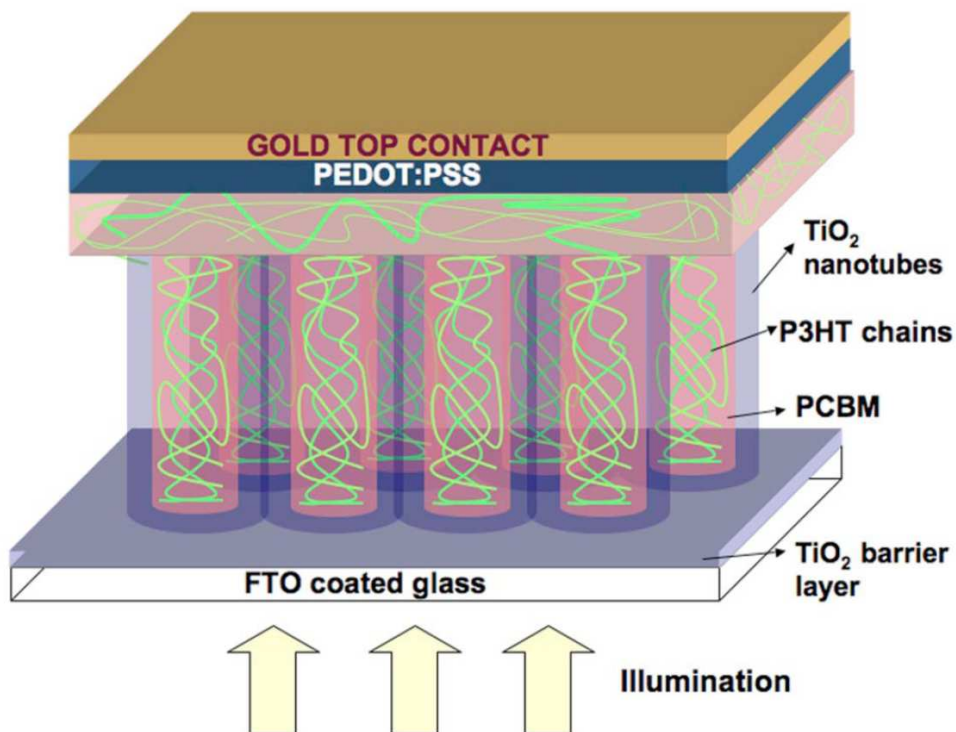


Figure 3-12: Illustration showing the device configuration, materials used, and the direction of illumination. Adapted with permission from [¹⁰⁸]. Copyright 2007 American Institute of Physics.

Another approach for improved PCE is doping of the metal oxide. It is demonstrated that Li₂O doping of TiO₂ improves the conductivity up to 2 orders of magnitude.¹⁰⁹ OPV devices with Cs doped TiO₂ nanocrystals result in a PCE of up to 4.2 %, which is one of the highest reported efficiencies for inverted OPV cells based on P3HT:PCBM as active layer to date.¹¹⁰

3.3.2.2 Organic Layers

Organic semiconducting layers can be distinguished into polymers and small molecules. Small molecules typically are thermally evaporated, while polymers are solution processed. Solution processing of organic interfacial layers is attractive for cheap and fast roll-to-roll processing. Vacuum steps can be avoided but the downside is that orthogonal solvent systems¹¹¹ or cross-linkable polymers have to be used to allow stacking of the individual solution processed layers. P-type interface materials are hole transport materials which can additionally be p-doped, n-type materials are electron transport materials¹¹² which can additionally be n-doped. Small molecules have the advantage that the matrix material and the dopant can be co-evaporated. A good review on doping of organic materials for OLEDs and small molecule OPV is done by Walzer et al.¹¹³ and will not be discussed in detail in this review.

3.3.2.2.1 P-Type Organic Materials

Pedot is widely used as solution processed p-type interfacial layer and transparent electrode material in organic electronics. Usually Pedot is doped with PSS for improved conductivity and solubility in protic solvents.¹¹⁴⁻¹²³ The purpose of the incorporation of PEDOT:PSS as p-type interfacial layer is explained with:

- Improved selectivity of the anode.
- Improved smoothness and coverage of e.g. ITO-peaks.
- Modified work function of the transparent electrode.

Comparable device performances are obtained with alternative organic p-type interfacial layers such as sulfonated poly(diphenylamine)^{118, 119}, polyaniline (PANI)^{120, 121} and polyaniline-poly(styrene sulfonate)(PANI-PSS).¹²²

Figure 3-13 summarizes device parameters (J_{sc} , V_{oc} , FF and PCE) of OPV devices in the normal structure without p-type like interfacial layer and with PEDOT:PSS in different thicknesses. All device parameters show a clear improvement when PEDOT:PSS is used. Because of good transparency and conductivity the device performance is insensitive to the layer thickness of PEDOT:PSS.¹²³ Improvements in conductivity of PEDOT:PSS reduce losses in the serial resistance which in turn results in increased PCE.

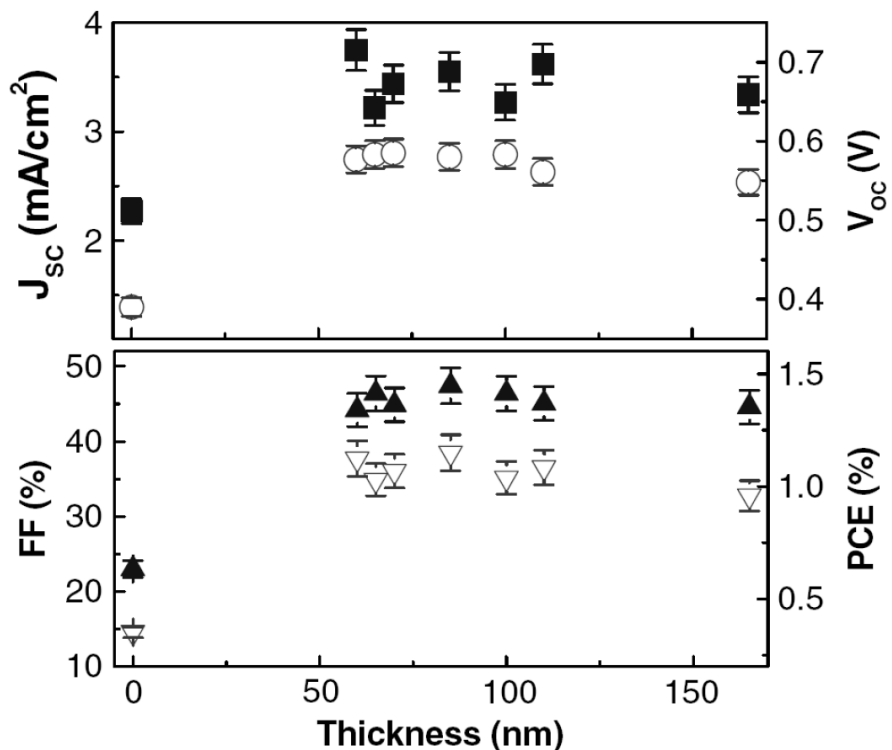


Figure 3-13: J_{sc} (filled squares), V_{oc} (open circles), FF (filled upward triangles), and PCE (open downward triangles) as a function of PEDOT:PSS layer thickness. Adapted with permission from [123]. Copyright 2008 Elsevier.

This makes the material even more suitable as transparent electrode material and, results in better performance. For example, mannitol p-dopes PEDOT:PSS and improves the conductivity and the performance of OPV devices. An increase in device performance from 4.5 % to 5.2 % is reported.¹²⁴ Additives for PEDOT:PSS which improve the conductivity include high-dielectric solvents such as dimethyl sulfoxide and N,N-dimethylformamide, or polar compounds such as glycerol, ethylene glycol, polyalcohols and sorbitol.¹²⁵⁻¹³⁶ The origin of the improvement in PCE and conductivity is mainly explained with morphological changes. Highly conductive PEDOT:PSS which additionally is supported with a metal grid, is demonstrated as transparent electrode in OPV devices.¹³⁷⁻¹³⁹

A major disadvantage of PEDOT:PSS is its intrinsic acidity which can cause degradation within the OPV stack. Jong et al. studied the interface of PEDOT:PSS and ITO by Rutherford backscattering and found that PEDOT:PSS is etching ITO. Annealing and storage of the

sample in air does increase the concentration of indium within PEDOT:PSS.¹⁴⁰ A detailed description of other degradation mechanisms is given elsewhere.¹⁴¹⁻¹⁴³

3.3.2.2.2 N-Type Organic Materials

Little is reported on OPV with n-type doped organic layer. On the other hand, organic n-type materials are very popular within the OLED community and also within the small molecule OPV community. In this review we will highlight only few materials and otherwise refer to the excellent review by Walzer et al.¹¹³ which also includes the n-type doping of organic layers by alkali metals.

Bathophenanthroline (BPhen)¹⁴⁴ and bathocuproine (BCP) are good electron transport layers and good hole blocking materials.^{145, 146, 70, 72} BCP additionally acts as an exciton blocking layer.^{70, 72} Approaches to n-dope organic materials make use of cationic dyes such as Rhodamin B, Pyronin B, Acridine Orange Base and Leuko Kristall Violett¹⁴⁷⁻¹⁵⁰. The feasibility of such materials has already been demonstrated for OPV cells.^{151, 152} The doping of organic materials by metals, e.g the doping of BPhen by Ytterbium (Yb), is successfully demonstrated in OPV devices.¹⁵³

Chan et al. reported on n-doping of C₆₀ with decamethylcobaltocene (CoCp₂) in OPV devices¹⁵⁴ and Figure 3-14 shows the impact of a doped C₆₀ interface layer. FF and Isc could be clearly improved due to the doping of the near contact region.

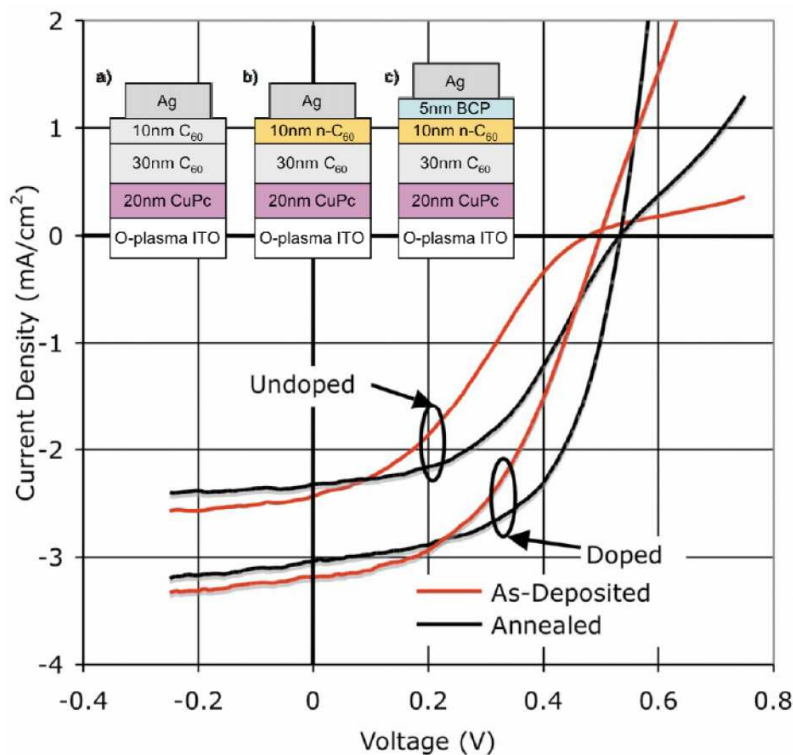


Figure 3-14: Current density vs voltage (J-V) characteristics of the diodes under 1 sun illumination. Inset illustrates device structures in this study. “Undoped” data correspond to structure (a) (ITO/phthalocyanine(CuPc)/C₆₀/Ag). “Doped” data are representative of (b) and (c). Herein C₆₀ is doped by CoCp₂. Adapted with permission from [¹⁵⁴]. Copyright 2009 American Institute of Physics.

3.3.3 Dipole Layers

The modification of the work function of the electrode by dipole layers is an elegant alternative way to generate the required interface and to form an Ohmic contact. The surface treatment of electrode materials by dipole layers can result in a modified electrode work function through surface dipole formation. Figure 3-15 illustrates the simplest case of acid and base treatment of the electrode material. The arrangement of molecules and charges results in a shift of the respective work function. Acidic treatment leads to protonation of the ITO surface and an interfacial dipole pointing away from the electrode is formed with the anions, leading to an increase of the work function of the electrode. Basic treatment forms an interfacial dipole which points towards the electrode and the workfunction is reduced. Large counterions result in a larger surface dipole and thus shift the work function more effectively¹⁵⁵.

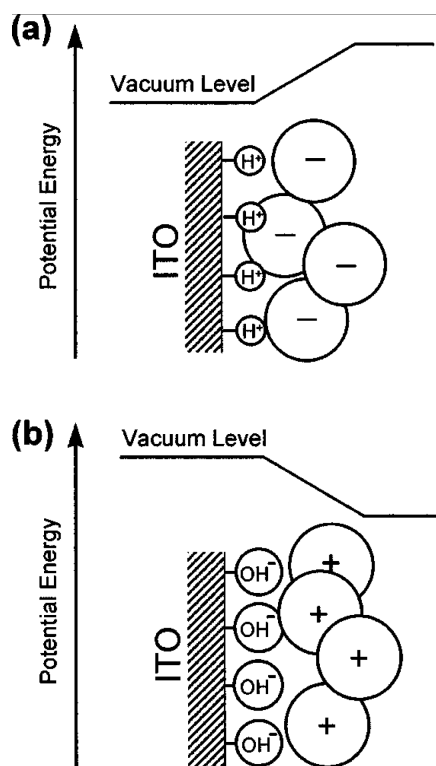


Figure 3-15: Schematic illustration of the monolayer adsorption of Brønsted acids (a) and bases (b) onto the ITO surface. The corresponding qualitative vacuum level shift is also indicated in the graph. Adapted with permission from [¹⁵⁵]. Copyright 1999 American Institute of Physics.

Photoelectron spectroscopy is used to quantify the influence of various acid and base treatments of the ITO surface. The workfunction of untreated ITO is measured at 4.4 eV and remained unchanged when the electrodes are dipped in water (neutral pH). Acidic treatment with nitric acid, hexafluorophosphoric acid and phosphoric acid increased the workfunction up to 5.1 eV, basic treatment with sodium hydroxide and tetrabutylammonium hydroxide decreased the workfunction by 0.2 and 0.5 eV, respectively.

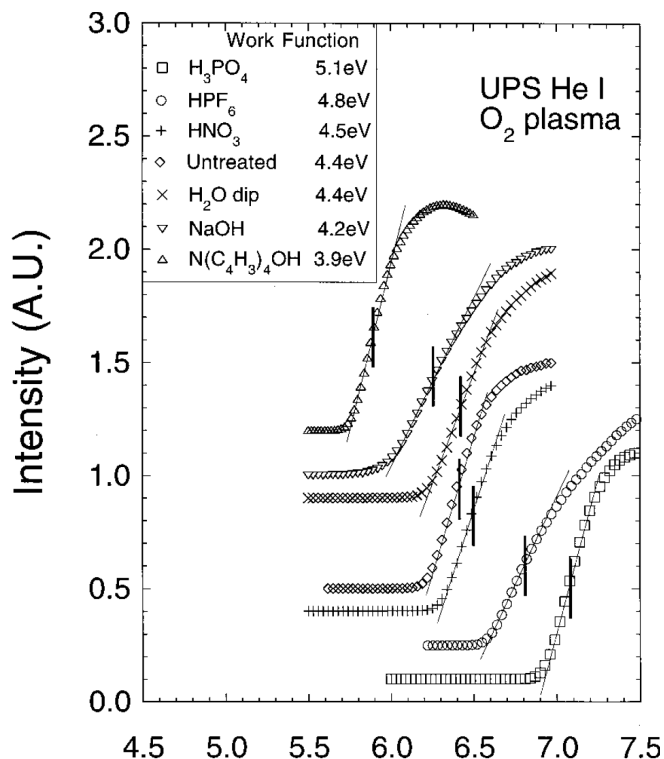


Figure 3-16: He I UPS spectrum of ITO taken with 25.000 V bias applied to the sample. The inelastic cutoff part of the electron energy distribution curve is shown. Different surface treatments as well as the corresponding work functions are indicated in the graph. Adapted with permission from [¹⁵⁵]. Copyright 1999, American Institute of Physics.

3.3.3.1 Self-Assembled Monolayers

The modification of the electrode work function in OPV devices to adjust the barrier height between two layers by self-assembled monolayers (SAMs), i.e. active layer/interfacial layer/electrode, is successfully reported in several publications.^{158, 160} The strength and direction of the dipole determines the resulting work function of the SAM modified substrate and the interface. An adjusted barrier results in improved device performance, a non-adjusted barrier in decreased device performance. Several groups investigated the impact of a variety of SAMs to the work function of the electrodes, the interface electrode/interfacial layer and interfacial layer/active layer as well as the resulting device performance:

The modification of the work function of ITO by 4-chlorobenzoylchloride (CBC), 4-chlorobenzenesulfonyl chloride (CBS) and 4-chlorophenyldichlorophosphate (CBP)¹⁵⁶ as well as with SAMs with a terminal group of -NH₂, -CH₃ and -CF₃¹⁵⁷ results in improved

device performance. The metal/SAM/ZnO interface is modified with lauric acid, mercaptoundecanoic acid and perfluorotetradecanoic acid.¹⁵⁸ Similarly, the interface between TiO_x and P3HT:PCBM is modified with lauric acid, benzoic acid, terthiophene an C₆₀ substituted benzoic acid.¹⁵⁹

Yip et. al modified the interface ZnO/metal electrode by a series of parasubstituted benzoic acid (BA-X) SAMs with negative ($-OCH_3$, $-CH_3$, $-H$) and positive ($-SH$, $-CF_3$, $-CN$) dipoles. The gas-phase dipole moment (D) of BA-X is $-OCH_3$ (-3.9D) < $-CH_3$ (-2.9D) < $-H$ (-2.0D) < $-SH$ (1.5D) < $-CF_3$ (2.1D) < $-CN$ (3.7 D). Table 2 summarizes results for the device structure ITO/PEDOT:PSS/P3HT:PCBM/ZnO/BA-X/Al.

Table 2: Summary of device performance of polymer solar cells with different benzoic-acid-based molecules modified ZnO/Al cathode. Adapted with permission from [¹⁶⁰]. Copyright 2008, Wiley VCH.

Cathode configuration	Voc [V]	Jsc [mAcm ⁻²]	FF	PCE [%]	R _p [Ocm ²]	R _s [Ocm ²]
ZnO/BA-OCH ₃ /Al	0.65	11.61	0.55	4.21	648.8	1.5
ZnO/BA-CH ₃ /Al	0.64	11.63	0.49	3.63	438.0	2.1
ZnO/BA-H/Al	0.64	11.46	0.48	3.48	583.3	2.2
ZnO/Al	0.6	11.29	0.47	3.16	392.5	3.1
ZnO/BA-SH/Al	0.45	10.44	0.42	1.95	184.7	13.3
ZnO/BA-CF ₃ /Al	0.3	8.97	0.31	0.84	64.1	24.2
ZnO/BA-CN/Al	0.27	8.15	0.28	0.62	47.2	14.4

SAMs with a positive dipole moment increase the barrier height between ZnO and Al resulting in a decrease in device performance. SAMs with a negative dipole show a positive effect to the device performance and the PCE increases from 3.16 % for -/ZnO/Al to 4.21 % for -/ZnO/BA-OCH₃/Al. The device performance correlates with the strength of the dipole and the one with the highest dipole have the best performance. The authors present successfully that the right choice of SAMs improves the device performance and makes varying metal electrode materials suitable for OPV.¹⁶⁰

3.3.3.2 Salts

The most prominent approaches for improving the device performance of OPV cells makes use of the salts LiF and Cs_2CO_3 . Especially for LiF two possible origins of the improvement in PCE are under discussion: Doping of the acceptor material by Li and modification of the work function of the electrode through dipole formation.¹⁶¹⁻¹⁶⁶

For the normal structure a prominent cathode is a combination of LiF and Al, both of which are thermally evaporated on top of the active layer. The incorporation of a 0.6 nm thick LiF layer between the active layer and the Al electrode does improve the FF from 53% to 63% and V_{oc} from 0.76 V to 0.83 V for a MDMO-PPV/PCBM solar cell. Even LiF/Au can act as cathode despite the high work function of Au of 5.1 eV.¹⁶¹ LiF is first applied in OLEDs in the structure tris(8-hydroxyquinoline)aluminium (Alq_3)/LiF/Al. It is suggested that the decomposition of LiF leads to chemical doping of Alq_3 by Li¹⁶⁷. Li⁺ ions diffuse into and dope the organic layer. On the one hand this effect is favorable since it allows doping of the active layer by placing the dopant on top of the active layer. On the other hand the diffusing dopant limits the lifetime¹⁶⁸. Cs, also a dopant for organic materials, has a lower diffusivity than Li and promises a higher lifetime.¹⁶⁸ Similar results are reported for doping of BPhen and BCP^{169, 170}.

Cs_2CO_3 is an example of a solution deposited salt. The work function of ITO coated with different salts is depicted in Figure 3-17 and decreases from ITO to ITO/ CS_2CO_3 . V_{oc} and J_{sc} increases with the reduction of the work function of the cathode. V_{oc} and J_{sc} increase from 0.2 V to 0.56 V and J_{sc} from 7.01 mA/cm² to 9.7 mA/cm² when applying a Cs_2CO_3 layer on ITO. Figure 3-17 (b) schematically presents the O-Cs dipole formed which results in a reduction of the work function of the coated ITO.¹⁷¹

This trend holds when reducing the work function of ITO/ CS_2CO_3 further from 3.45 eV to 3.06 eV by an annealing step at 150°C. The reduced work function results in an improvement in PCE from 2.31 % to 4.19 %. V_{oc} is improved from 0.55 V to 0.59 V, J_{sc} from 7.61 mA/cm² to 11.13 mA/cm² and the FF from 55 to 64 %.¹⁷²

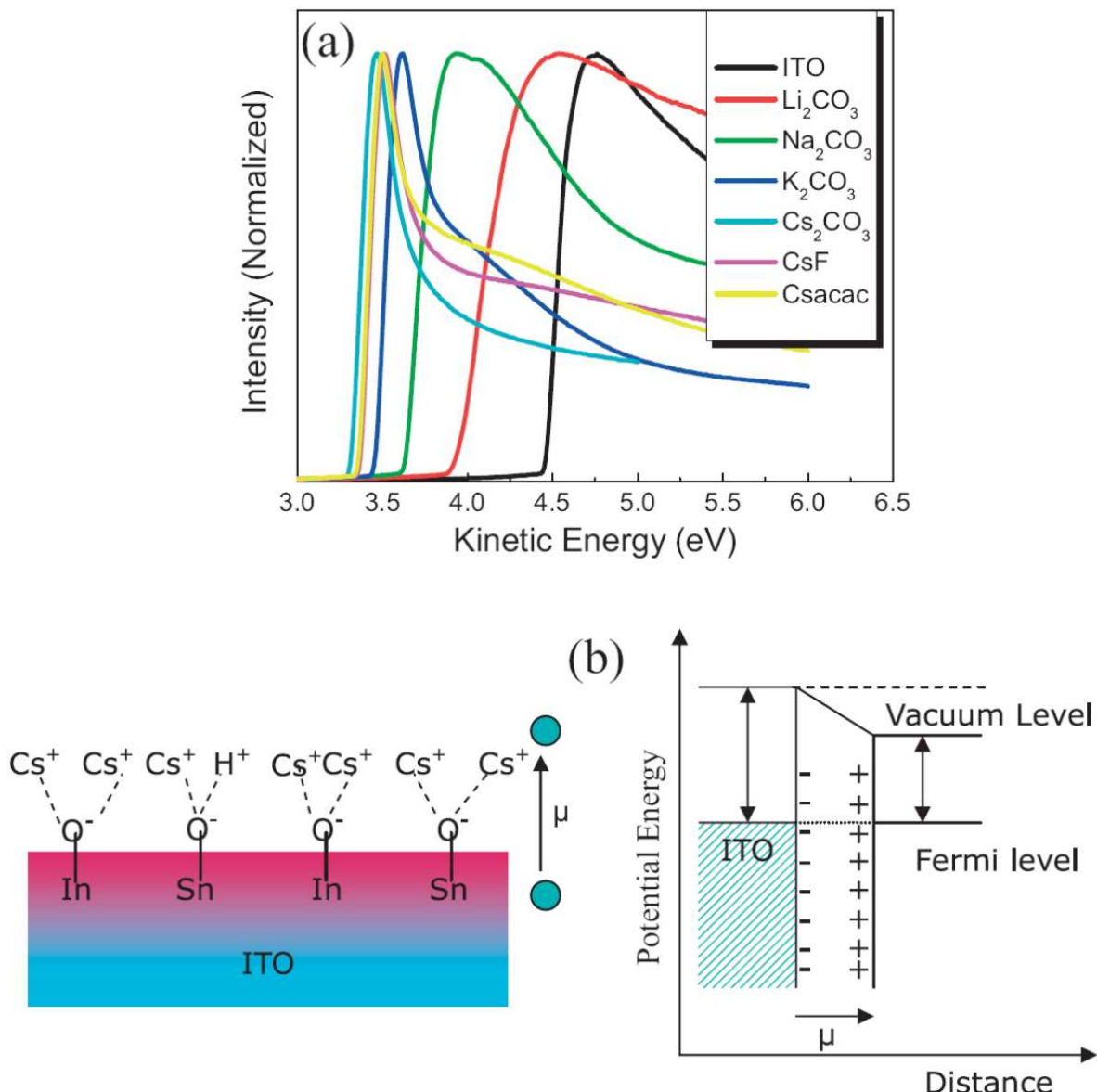


Figure 3-17: a) Evolution of secondary electron edge with different buffer layers on ITO, b) scheme for the formation of dipole layer on ITO. Adapted with permission from [¹⁷¹]. Copyright 2008, Wiley VCH.

3.4 Summary

In summary the function of interfacial layers in organic solar cells is discussed and a wide range of materials applied for OPV are reviewed. It is distinguished between metallic, organic, inorganic, semiconducting, n-type and p-type interfacial layers and the most prominent ones are reviewed. For the development of future OPV structures with increased PCE and lifetime, the right choice of interface materials is of fundamental interest which will be discussed in the next chapters. Many groups demonstrated that improved interfaces are essential for optimized PCE. An excellent interface material is not only characterized by the resulting enhanced PCE of the device, but also by the degradation of the interfacial layer itself and the degradation in combination with the other materials of the OPV cell. The optimization of both, PCE and lifetime, will further improve the potential and attractiveness of OPV. The optimum choice of interface materials is a key factor for highly efficient and stable OPV devices.

4 Impact of the Shunt Resistance on the Performance of Organic Photovoltaic Cells

In this chapter the need of high shunt resistances for organic solar cells is experimentally studied and design rules for OPV cells and modules for both indoor and outdoor applications are presented. Since the light intensities and thus the resulting current densities are much lower for indoor compared to outdoor applications, different design rules can be derived. Further, the impact of the shunt resistance to module shading scenarios and design parameters for organic bypass diodes are discussed. The degradation of single cells under reverse bias conditions is studied in dependence of the shunt resistance. Two types of cells are distinguished depending on the respective shunt resistance in the dark:

- (a) Type I cells have an excellent dark rectification and a high shunt resistance.
- (b) Type II cells have a lower rectification and specifically a smaller shunt resistance.

Figure 4-1 presents varying OPV cells with a wide range of shunt resistances which are processed and measured while this work.

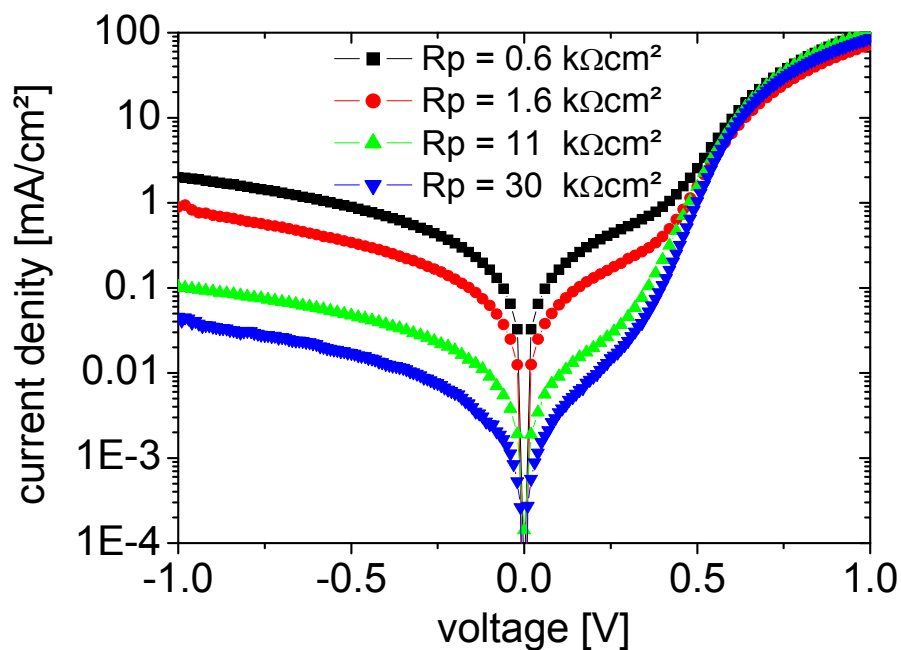


Figure 4-1: Dark J-V characteristics of OPV cells processed while this work with different magnitudes of shunt resistances.

Various cells with different shunt resistances are investigated and design rules for OPV cells for the following applications are derived:

- (a) Module shading mechanisms and reverse bias degradation
- (b) Low light applications
- (c) Bypass diodes

4.1 Hot Spots

The serial interconnection of single solar cells to modules is an elegant and advantageous method to achieve the desirable supply of voltage which is needed for a certain application. Despite the obvious positive effect of cell interconnection in series on the voltage of large area solar modules, it is well known that serial interconnected inorganic modules are sensitive to specific failure mechanisms which otherwise do not arise in single solar cells. The most important one is the so called “shading” failure.^{173, 174} Shading occurs when individual cells of the module or even only a part of a cell in a module under operation is shaded. In such a case, the shaded cells have to transport the current of the module in reverse bias, and the excess photovoltaic power produced by the non-shaded part of the module can become dissipated across the “dark” cell. The formation of hot spots in inorganic PV modules has been known since early space applications.¹⁷⁵ Hot spots are defined as localised regions in a PV module where the operating temperature exceeds the temperature of the surrounding area. Generally speaking, this situation occurs when the cell under investigation generates less current than the rest of cells which are connected in series. In many cases this occurs through partial shading of a module by e.g. leaves, shadows of buildings or trees. Other factors which are leading to hot spots can be cell damage, a mismatch in the size of the single cells and/or power or interconnection failure. In this subchapter the impact of the shunt resistance to this irreversible module failing mechanisms is discussed.

4.1.1 Reverse Bias Testing

As a result of module shading, the shaded cell is reverse biased and behaves like a resistive load which dissipates electrical power generated by the rest of the cells in the form of heat. A well established countermeasure for hot-spots uses bypass diodes in parallel with a group of solar cells in reverse polarity within the module. The number of bypass diodes per solar cells

depends on the cell technology. While Si typically uses one bypass diode for each 12 – 18 cells, the current generation of dye sensitized solar cells does not require bypass diodes. Dye sensitized solar cells are Type II cells with a high leakage current and therefore a low voltage drop under reverse bias voltages. In order to ensure that the PV modules are protected against this damage, international standards require that modules must be subjected to hot-spot endurance tests before their qualification.¹⁷⁶⁻¹⁷⁹ Although numerous publications exist reporting the shading effects of inorganic cells, this has never been addressed for OPV technology. Typical modules investigated in this thesis consist of 10 single cells connected in series with a module voltage of 10 times V_{oc} . A shaded cell within a module acts as load and is driven by the rest of the cells. As such, the maximal voltage that can drop across the shaded cell is the one provided by the non-shaded cells, i.e. 9 times V_{oc} or approximately 5 V for the system under investigation. The shunt resistance or leakage current of the OPV cell then determines the voltage that has to be applied on the shaded cell to transport the current density provided by the non-shaded cells. The dissipated power within a shaded cell is proportional to the shunt resistance of the cell. As such the shunt resistance is an essential number determining the power dissipation within a shaded solar cell. To investigate whether OPV cells pass the hot-spot endurance test within a 10 cell module a reverse voltage of -5 V for 5 h is applied on OPV cells in the dark. These investigations identify whether a high or low shunt resistance is beneficial for passing the hot spot endurance test which is essential for OPV applications.

4.1.2 Degradation under Reverse Bias in Hot Spots

Figure 4-2 presents J-V curves of a typical illuminated (a) and dark (b) flexible organic solar cell before and after reverse bias degradation. After 5 h at -5 V clear signs of degradation are observed. The dark shunt resistance of the cell decreases from $8000 \Omega\text{cm}^2$ to $220 \Omega\text{cm}^2$ by reverse bias degradation. The dark leakage current at -1 V increases from $170 \mu\text{A}/\text{cm}^2$ to $7.3 \text{ mA}/\text{cm}^2$. This strong decrease in the shunt resistance and increase in leakage current results in a significant loss in FF and even V_{oc} is affected. Losses in FF and V_{oc} can be clearly assigned to the decreased shunt resistance. J_{sc} is affected in the range of 10 % from initial value which can not be explained by the shunt resistance. The decreased short-circuit current is related to a different type of degradation. The serial resistance is not affected. In summary,

the increased leakage current is the most severe failure mechanism when reverse biasing an organic solar cell. In the following the origin of the increased leakage current is investigated.

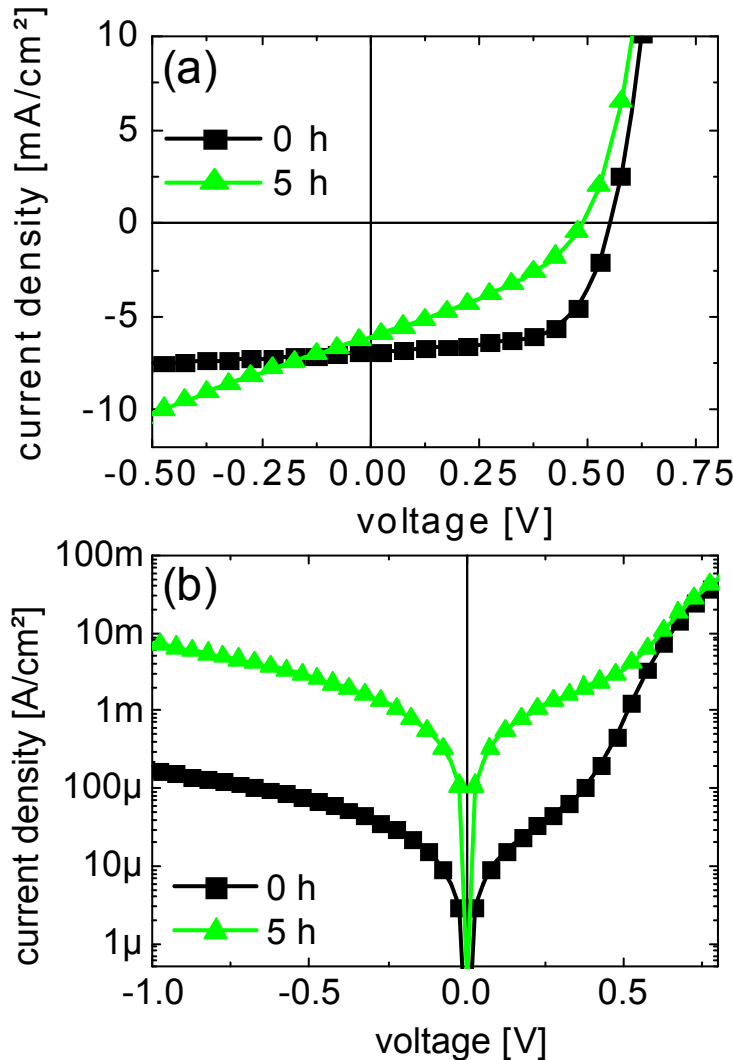


Figure 4-2: Representative J-V characteristics of the solar cell studied under illumination (a) and in the dark (b). The data are plotted in a log-linear representation.

For imaging the heat dissipation within the cell under reverse bias operation, multiple cells are analyzed by high resolution dark lock-in thermography (DLIT). The flexible solar cells are pulsed by a rectangular negative voltage of -5 V at a lock-in frequency of 2 Hz. The spatially resolved heating of the cells due to different levels of energy dissipation is recorded

by an IR camera. Figure 4-3 presents a typical dataset of such a DLIT measurement for an OPV cell before (a) and after (b) reverse bias degradation at -5 V for 5 h.

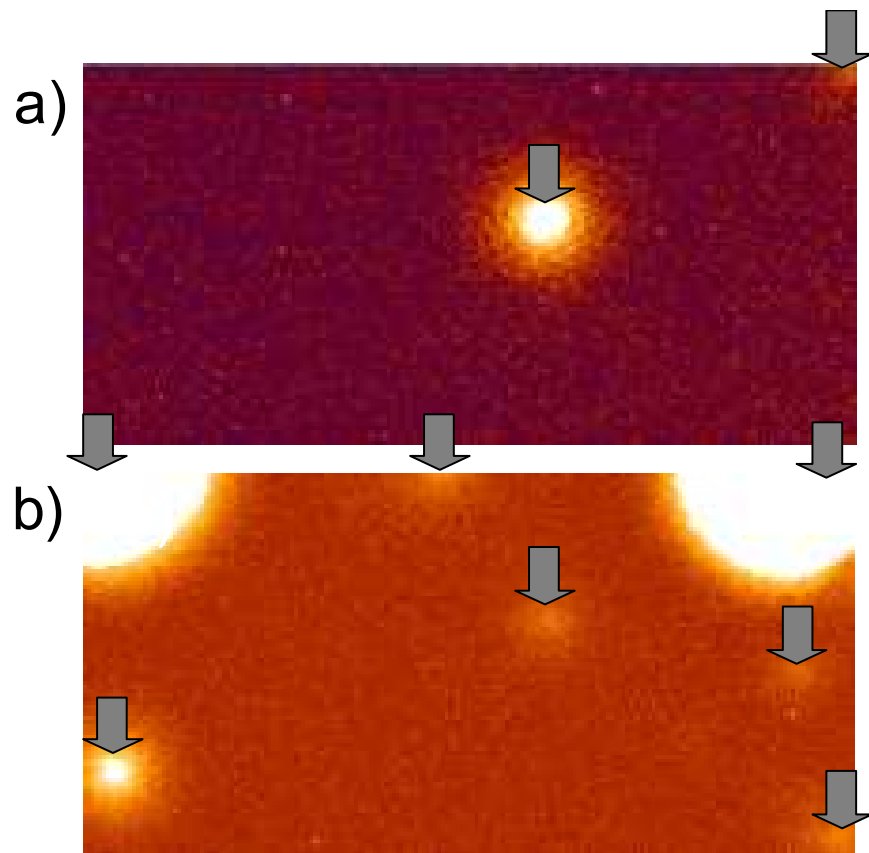


Figure 4-3: DLIT measurement: Image size represents active area of an organic solar cell of 5 mm x 10mm. Light colours correspond to higher temperatures. Different colours are used in the two images. (a) shows the DLIT amplitude image of a non-degraded cell and (b) the map of a degraded cell. The corresponding heat radiation to one colour varies from measurement to measurement. Hot spots are marked by arrows as guide for the eye.

These measurements clearly identify local areas with higher heat dissipation under reverse bias voltage, i.e. hot spots, even for a non degraded cell. The investigated cell exhibits hot spots on the edge as well as within the active area of the device. (Figure 4-3 (a)) Reverse biasing of a cell significantly increases the amount of hot spots which are visible by the high sensitivity of the DLIT measurement setup. In addition, the amplitude signal of the existing hot spots, which correlates with the heat dissipated in the hot spots, increases under these conditions. By comparing the DLIT amplitude image of the cell before and after degradation

it can be concluded that reverse biasing does induce increased local shunting (lower shunt resistance).

The presented results show an increase in the leakage current and in the amount of hot spots with time of degradation. The dissipated power in the dark under reverse bias voltage correlates with the current and as such with the leakage current of the cell. Therefore the increase in the amount and strength of hot spots correlates with the increased leakage current under reverse bias degradation. These results suggest that devices with no or only weak hot spots suffer from less degradation under reverse bias since the initial power dissipation within the device is little.

To correlate the leakage current with reverse bias degradation several cells are degraded under a reverse bias of -5 V for 5 h. An OPV cell with a high shunt resistance or little leakage current dissipates less power under reverse bias voltage. Figure 4-4 compares the reverse bias degradation behavior of various cells with different magnitudes of leakage current, but otherwise identical. Before degradation, the cells are separated into two classes – one with a higher leakage current density ($> 100 \mu\text{A}/\text{cm}^2$ at -1 V) and one with a low leakage current density ($< 100 \mu\text{A}/\text{cm}^2$ at -1 V). Figure 4-4 (b) compares the power conversion efficiencies of the solar cells before and after reverse biasing at -5 V for 5 h. A direct correlation between the leakage current density at time zero and the strength of degradation under reverse bias is found. Cells with a high initial leakage current density ($> 100 \mu\text{A}/\text{cm}^2$ at -1 Volt) have a significantly higher probability of severe degradation by more than 50 % in efficiency under reverse bias stress. These cells typically suffer from a strong increase in the leakage current (lower shunt resistance) which is directly related to a dominant loss in the FF. On the other hand, cells with a low leakage current density ($< 100 \mu\text{A}/\text{cm}^2$ at -1 V) have a much higher probability to survive reverse bias stressing with only little degradation. Statistically, it is found that the leakage currents of these cells do not increase, and, on the average, these cells lose less than 20 % in performance after reverse biasing. The residual losses are mainly due to a slight decrease in FF and J_{sc} , with the FF losses being much lower (~ 10 %) compared to cells with high leakage current densities (~ 40 %). These results suggest that cells with nearly defect-free electrode interfaces and bulk layers do not develop new shunts during degradation and are stable under reverse bias degradation. Contrarily, cells with interface or bulk defects rapidly degrade under reverse bias stressing due to an increase in the leakage current and a reduction of the fill factor.

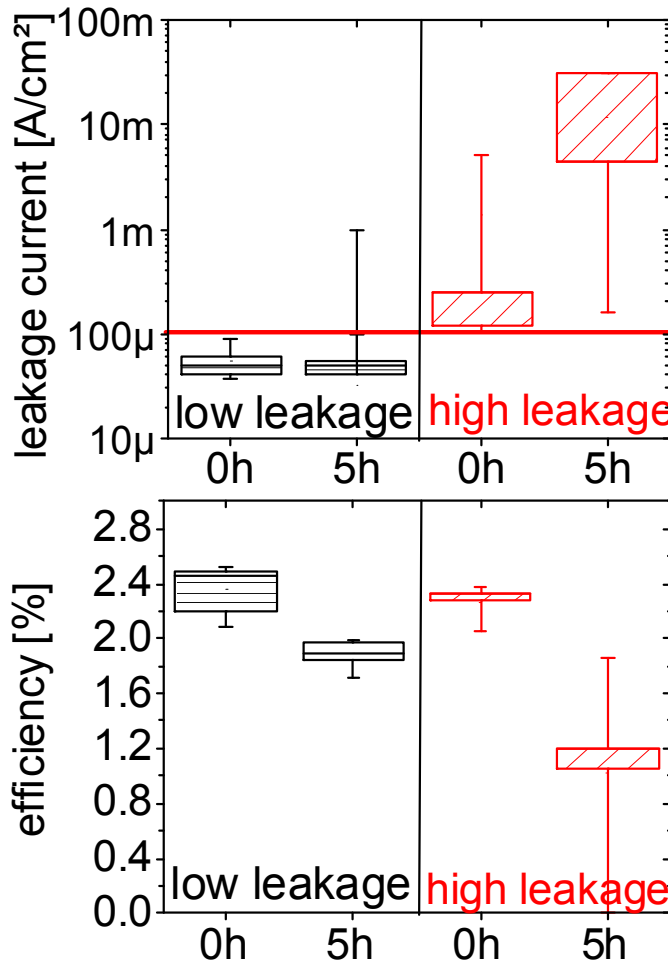


Figure 4-4: The degradation at -5 V for 5 h in dependence of the leakage current is compared. The OPV cells are divided into 2 groups, one with a low leakage current ($< 100 \mu\text{A}/\text{cm}^2$ at -1 V , black color) and one with a high leakage current ($> 100 \mu\text{A}/\text{cm}^2$ at -1 Volt , red color). The upper plot (a) represents the leakage current at -1 V before and after reverse biasing for 5 hours at -5 V . Plot (b) shows the power conversion efficiency before and after degradation for the high and low leakage current cells. Data are presented in box plots.¹⁸⁰

4.1.3 Summary

In summary a dominant contribution of local “low shunt resistance” areas, so called hot spots, to the degradation of bulk-heterojunction solar cells under reverse bias is found. The

leakage current of an organic solar cell is a key parameter to control the dominant FF degradation under reverse bias stressing. Cells with sufficiently low leakage currents at time zero, i.e. $< 100 \mu\text{A}/\text{cm}^2$ at -1 V, remain stable over 5 h under reverse bias stressing at a negative bias of 10 times the V_{oc} . This is equivalent to a shading test for a 10 stripe module, and it can be concluded that a 10 stripe OPV module with a cell leakage current of each cell $< 100 \mu\text{A}/\text{cm}^2$ will show no or only little degradation in FF under 5 h of shading. A further reduction of the leakage current, for instance by improving the quality of the interfaces and the bulk layer, is expected to further increase the reverse bias stability.

4.2 Low Light Applications

In this subchapter the performance and requirements for OPV cells for indoor applications, i.e. low light applications are discussed. OPV cells are well suitable for indoor applications when optimized for these requirements. OPV cells are primarily evaluated and certified for outdoor applications. Standardized tests and evaluations for indoor applications are missing although the requirements for indoor and outdoor applications are different. Since OPV enters the market for indoor and outdoor applications OPV cells have to be optimized for indoor applications as well.

The fundamental difference between indoor and outdoor applications is the spectrum of the light source and the light intensity. For outdoor applications the reference spectrum is the AM1.5 spectrum of the sun, for indoor applications a reference light source is missing. Artificial light sources, e.g. fluorescent lamps, LEDs and incandescent lamps, are used for indoor applications. Fluorescent lamps are widely used for offices and are investigated in detail as artificial light sources in this work. The phosphor layer of the fluorescent lamp converts UV radiation into visible radiation. The spectrums of different fluorescent lamps vary depending on the fluorescent materials used and are completely different to the AM1.5 spectrum of the sun. Figure 4-5 shows the spectrum of a fluorescent lamp and the AM1.5 spectrum of the sun in comparison to the absorption of P3HT.

The illuminance of a fluorescent lamp is measured in lx and is weighted by the sensitivity of the human eye. Typical values of the illuminance requirements for offices range between 200 lx and 1000 lx¹⁸¹, which is a factor 100 – 500 lower than 1 sun illumination. In this

chapter the performance of OPV cells with varying R_s and R_p is discussed and design rules for indoor applications are derived.

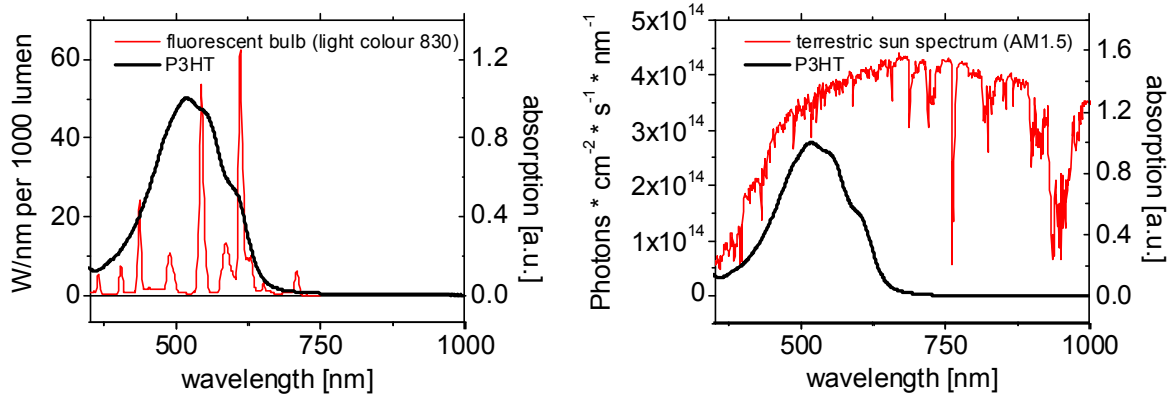


Figure 4-5: Comparison of the spectrum of a fluorescent lamp and the AM1.5 spectrum of the sun with the absorption of P3HT.

4.2.1 Impact of the Shunt Resistance for Low Light Applications

An OPV cell is measured with 1 sun illumination compared with 1000 lx low light conditions using a fluorescent bulb with the light colour 830. The spectrum of a fluorescent lamp and the AM1.5 spectrum of the sun in comparison to the absorption of P3HT are shown in Figure 4-5. OPV cells are characterized with these light sources in this sub-chapter. J_{sc} is reduced from 8 mA/cm^2 for illumination at 1 sun to $70 \mu\text{A/cm}^2$ for illumination at 1000 lx. The measured J_{sc} at 1000 lx is approximately 0.875 % of the one under 1 sun. It must be noted that this value strongly depends on the used light source as will be discussed later in the text. To illustrate the impact of R_s and R_p for indoor and outdoor applications the same value of shunt and serial resistances is numerically calculated to the J-V characteristics of the measured reference OPV cell at 1 sun and 1000 lx. The impact of the serial resistance is investigated by numerically adding a series resistance R_s of $10 \Omega\text{cm}^2$, $25 \Omega\text{cm}^2$ and $50 \Omega\text{cm}^2$ to the measured J-V characteristics. Figure 4-6 (a) and (b) presents results under 1 sun, (c) and (d) for low light at 1000 lx. For 1 sun illumination, the performance of the OPV cell is predominantly limited in FF for all investigated serial resistances. In addition, for high R_s values the J_{sc} becomes affected.

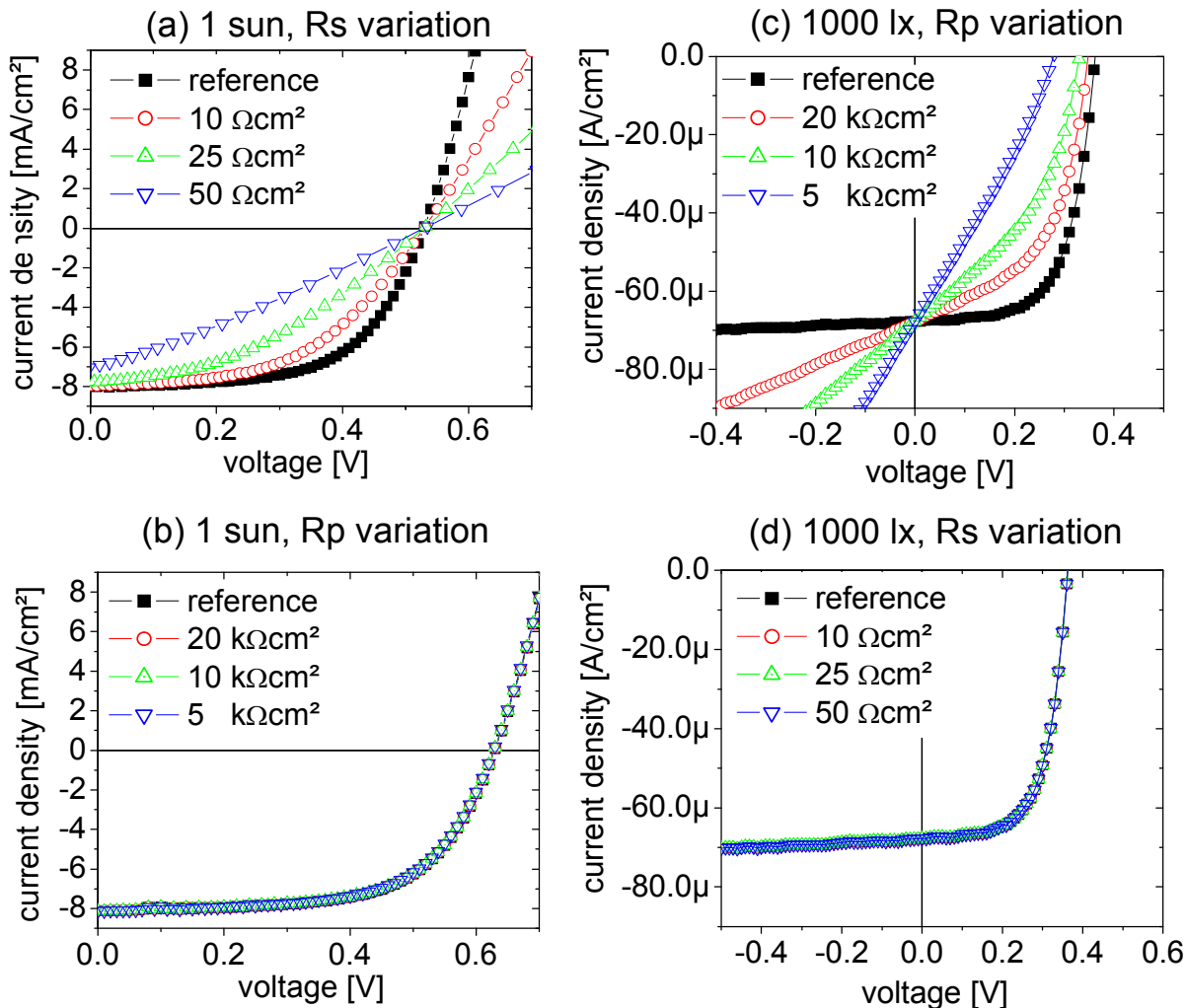


Figure 4-6: Illustration of the impact of R_p and R_s to the J-V characteristics of OPV cells measured at 1 sun and 1000 lx. R_s and R_p are numerically included into to the measured J-V characteristic of the reference OPV cell.

For the measurement at 1000 lx the impact of R_s to the device performance is different. The same serial resistances have no impact on the J-V characteristics in the 4th quadrant. The impact of R_p is investigated by the addition of a resistance of 20 kΩcm², 10 kΩcm² and 5 kΩcm² to the measured J-V characteristics for indoor and outdoor applications. These values of R_p do not limit the performance of the OPV cell in the 4th quadrant for outdoor applications. However, indoor illumination shows a significant limitation in FF with decreasing R_p . Lower R_p values affect V_{oc} . Summarizing initial findings, the impact of the shunt and serial resistance is different for indoor and outdoor applications. It is demonstrated

that low light applications require high shunt resistances to guarantee high efficiency OPV cells. For outdoor applications a lower shunt resistance is required. These results are explained by the reduced J_{sc} for low light applications and will be studied in more detail.

Figure 4-7 summarizes the performance of solar cells with different shunt resistances for different light intensities.

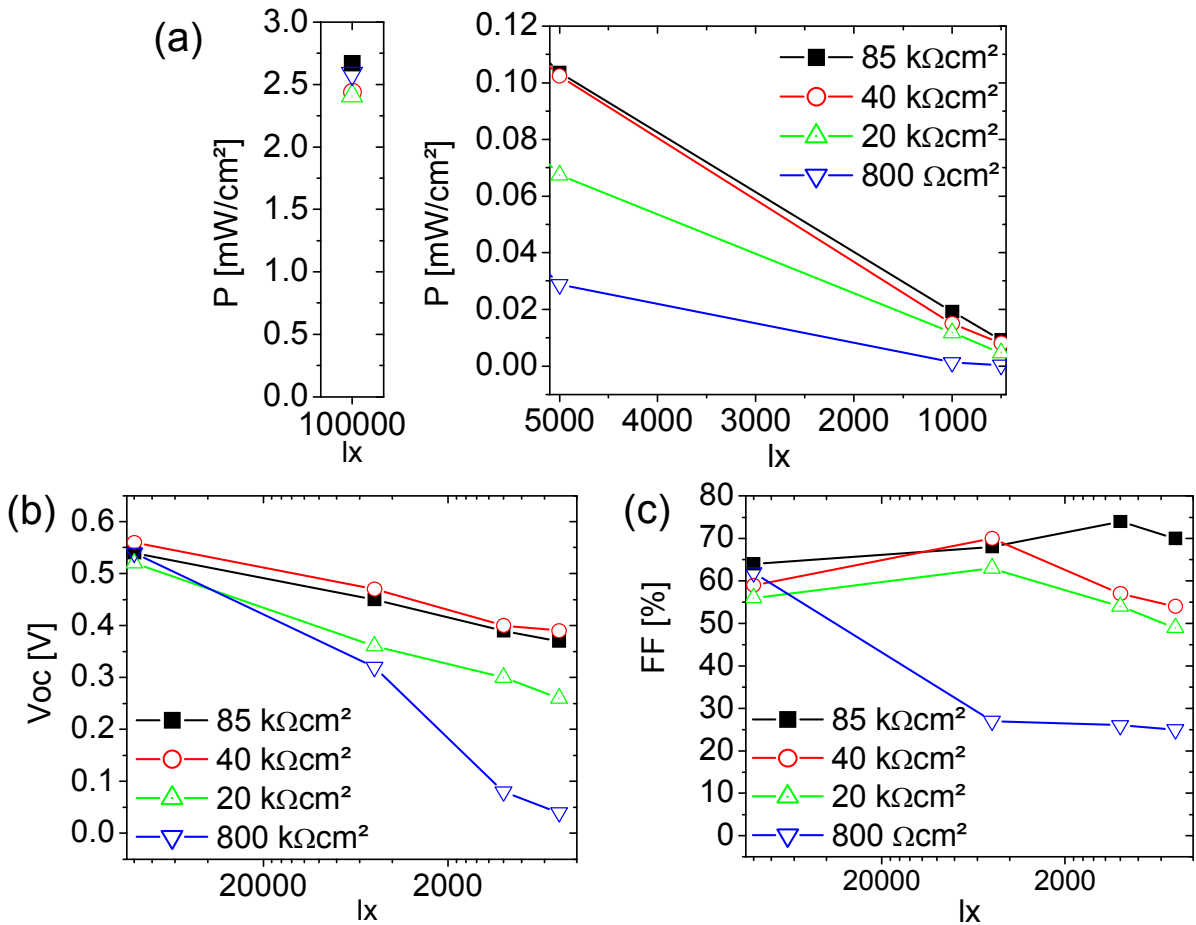


Figure 4-7: Impact of R_p to the (a) power output, (b) V_{oc} and (c) FF of OPV cells. OPV cells with varying R_p are measured at light intensities of 100,000 lx, 5,000 lx, 1,000 lx and 500 lx.

The investigated OPV cells have shunt resistances of $85 \text{ k}\Omega\text{cm}^2$, $40 \text{ k}\Omega\text{cm}^2$, $20 \text{ k}\Omega\text{cm}^2$ and $800 \Omega\text{cm}^2$. R_p is calculated from the slope of the illuminated J-V curve at 0V between the points -0.1 V and 0.1 V. Illumination with 5000 lx, 1000 lx and 500 lx is done with a

fluorescent lamp, for 100,000 lx a metal halogen bulb is used which corresponds for the setup to 1 sun. The power output, V_{oc} and FF are shown in Figure 4-7.

At 100,000 lx the measured cell performance is comparable for all investigated cells. The power output of the organic solar cells at MPP is $2.5 \text{ mW/cm}^2 \pm 10\%$, FF of $55\% \pm 10\%$ and V_{oc} of $550 \text{ mV} \pm 10\%$ under 100,000 lx illumination. For low light intensities the situation is completely different. OPV cells with comparable performance at 100,000 lx show a variation from $1.3 \mu\text{W/cm}^2$ to $19 \mu\text{W/cm}^2$ at 1000 lx. The organic solar cell with the highest shunt resistance has the highest power output, the cell with lowest shunt resistance has the lowest power output at 1000 lx. The situation is similar at 5000 lx and 500 lx. The FF of the cells with a shunt resistance of $800 \Omega\text{cm}^2$ decreases with decreasing light intensity. Interestingly, for a higher shunt resistance the FF increases with decreasing light intensity due to reduced impact of R_s and reaches a maximum. The FF of the OPV cell with a shunt resistance of $40 \text{ k}\Omega\text{cm}^2$ increases from 60 % at 100,000 lx to 70 % at 5000 lx. The organic solar cell with the highest shunt resistance of $80 \text{ k}\Omega\text{cm}^2$ shows an improvement of the FF from 64 % measured at 100,000 lx to 74 % measured at 1000 lx. A further reduction of the light intensity below 1000 lx again leads to a drop in FF. With increasing shunt resistances, this maximum shifts to lower light intensities. All cells in common is a decrease of V_{oc} with decreasing light intensity. OPV cells with lower R_p show a larger drop in V_{oc} . The proportionality of V_{oc} with the logarithmic of the light intensity for a sufficiently high R_p is explained in chapter 2.2.1. The additional dependence of V_{oc} with R_p is illustrated in Figure 4-6. Under low light conditions the impact of R_p to the cell performance increases which results in losses in FF and V_{oc} .

Figure 4-6 shows that high shunt resistances are essential for indoor, i.e. low light, applications whereas R_s is less critical. The situation is exactly opposite for outdoor applications where high light intensities dominate. The increase in FF with decreasing light intensity for an OPV cell with high shunt resistance can be explained by the reduced impact of the serial resistance to the cell performance. As discussed above, for reduced light intensities the impact of high serial resistances is low. Given a sufficiently high shunt resistance, the FF of the cell is improved.

A shunt resistance higher than $85 \text{ k}\Omega\text{cm}^2$ and R_s smaller than $3 \Omega\text{cm}^2$ are required for a solar cell which works for both outdoor and indoor applications. For OPV cells determined only for outdoor applications, a shunt resistance of higher than $1 \text{ k}\Omega\text{cm}^2$ and a serial resistance

lower than $3 \Omega\text{cm}^2$ are sufficient. Otherwise, devices determined only for indoor applications must have a shunt resistance higher than $85 \text{k}\Omega\text{cm}^2$ and a serial resistance below $50 \Omega\text{cm}^2$. The relatively poor requirements with respect to R_s open up the possibility to use transparent electrode materials which have a lower conductivity and are cheaper than ITO. PEDOT:PSS is such a material which provides sufficient conductivity for OPV cells for indoor applications. The use of such alternative electrode materials for low light applications helps reducing production costs. To match the high shunt resistances needed for indoor application, the quality of the deposited layers, including active layer and interfacial layers, has to be very good, i.e. homogeneous and free of pinholes. Moreover, excellent interface materials are a must to provide the selectivity which is required for a high shunt resistance. For outdoor application a high R_p is less important than for indoor applications, but highly conductive electrode material are essential.

The standardization of the PCE of OPV devices under low light is missing since there is no standardized light source. A typical fluorescent lamp has a completely different spectrum compared to the spectrum of the sun. The spectrum of the fluorescent lamp or LED depends on the type of the lamp and the provider. To determine the low light efficiency of the investigated cells, the energy of the fluorescent lamp (Philips F32T8/TL830) is determined to 0.27 mW/cm^2 at 1000 lx with a pyranometer (Eppley model PSP). Thus the best presented cell has an electrical power output of $19 \mu\text{W/cm}^2$. This corresponds to a PCE of 7 % at 1000 lx for the investigated fluorescent lamp.

4.2.2 Summary

The impact of the shunt and serial resistance to the performance of OPV cells is investigated and design rules for both indoor and outdoor applications are proposed. For indoor applications (1000 lx) a shunt resistance of $85 \text{k}\Omega\text{cm}^2$ or higher and a serial resistance of $50 \Omega\text{cm}^2$ or lower is required. For outdoor applications (1 sun) a shunt resistance of $1 \text{k}\Omega\text{cm}^2$ or higher is sufficient and a serial resistance of $3 \Omega\text{cm}^2$ or lower is required. OPV cells which are operated in both, indoor and outdoor illumination require a shunt resistance of $85 \text{k}\Omega\text{cm}^2$ or higher and a serial resistance of $3 \Omega\text{cm}^2$ or lower.

These findings help to further optimize OPV devices. For indoor applications an excellent shunt resistance is of fundamental interest. Typical OPV cells processed in this work in the

reference structure ITO/TiO_x/P3HT:PCBM/PEDOT:PSS/Ag have a shunt resistance in the range of 10 kΩcm² which is sufficient for outdoor applications but not for low light application. Therefore the shunt resistance of OPV cells has to be improved to match the requirements for low light applications. To this end, highly selective, pinhole free layers which have to be improved further are a must to guarantee highly efficient OPV cells with high FF for indoor applications. This part of this work. The impact of the serial resistance is not that dramatic, therefore novel transparent electrode materials become feasible. This allows replacing the expensive ITO by inexpensive materials, such as PEDOT:PSS. For outdoor applications highly conductive electrode materials are a must, but less optimized interface materials are feasible, which may reduce costs for this kind of application.

Another outcome of this study is that the impact of the shunt resistance is less severe for outdoor applications than for indoor applications. In dependence of the shunt resistance OPV cells can be efficient for outdoor applications but not for indoor applications. This has to be taken into account when evaluating OPV cells for indoor and outdoor applications. In addition, a light source with a defined spectrum for indoor applications has to be standardized. A hero PCE of 7 % under low light conditions has been achieved.

4.3 Organic Bypass Diodes

In chapter 4.1 the impact of a reverse bias voltage to the degradation of an organic solar cell is discussed. A correlation of the leakage current of the OPV cell with degradation is found. In this subchapter the discussion of module shading effects are expanded to the power loss of the whole module. From these results design rules for OPV modules and organic bypass diodes are derived to eliminate the adverse shading effects. The use of flexible organic bypass diodes is presented.

According to results from inorganic PV technologies, failure from shading has been divided into two classes. One of them is reversible while the other one is irreversible. To address these two failure mechanisms and their impact on OPV modules it is important to understand the shading-induced processes on a cell level. As stated earlier, a shaded cell has to transport the module photocurrent driven in reverse bias. Depending on the diode characteristics of the shaded cell, two scenarios can be distinguished which are typically called Type I or Type II behaviour.¹⁷⁶⁻¹⁷⁹

- *Type I cells*, on the one hand, have an excellent dark rectification and a high shunt resistance. Shading of one cell will result in a shut down of the module operation. The shaded diode is blocking in reverse bias operation. The shunt resistance R_p of the shaded cell determines the current transported across the cell according to V_{module} / R_p . In case of large R_p , the photovoltaic power of the non-shaded part of the module will be dissipated across the shunt resistance of the shaded cell, and the whole module will be shut down.
- *Type II cells*, on the other hand, have a lower rectification, and specifically a smaller shunt resistance. The photocurrent of the shaded module can be transported across the shaded cell. Thus, the shaded cell is driven into reverse bias until the leakage current of the cell does match the photocurrent of the partially shaded module. Therefore, the module can deliver the photovoltaic power of the shaded module diminished by the power which is required to drive the shaded cell into reverse bias.

In chapter 4.1 it is demonstrated that reverse bias testing of OPV cells and modules have shown that Type II cells are more responsible for irreversible degradation, while Type I cells could pass the IEC hot spot tests.

4.3.1 Design Rules for Organic Bypass Diodes

The impact of a fully shaded organic solar cell to the J-V characteristic is described in the following section. The J-V characteristic of a (partially) shaded cell in the 3rd quadrant determines the J-V characteristic of the entire module: The short-circuit current of a module is determined by the leakage current of the shaded cell at the voltage provided by the non-shaded cells, plus the current generated by the half-shaded module. Thus, the investigated impact of full shading of a cell is the most severe case for a module. Half shading, the most likely case under operation, is less severe to the losses in the power output characteristics and can be discussed analogically. Concentrically connected rings and other novel OPV-module designs¹⁸² can reduce the possibility of a fully shaded single cell within a module and thus reduce the losses in the power output under shading.

The standard method to handle shading failure in PV technologies is to incorporate so called bypass-diodes anti-parallel to the individual solar cells of the module. Under shading and reverse bias, respectively, the bypass diode opens up and forms an alternative electrical path

for the module's photocurrent. The voltage drop on the shaded cell is then limited to the voltage which is required for opening up the bypass diode.^{183, 184}

The processing of monolithically interconnected OPV modules is quite different to the one for inorganic PV modules. OPV modules are manufactured by roll to roll printing processes¹⁸⁵⁻¹⁸⁹ while inorganic solar cells are either processed by wafer based or vacuumbased processing technologies. Integration of inorganic bypass diodes by a pick and place process, as typically applied for inorganic PV modules, would be technically possible for OPV modules as well. However, combining such a discontinuous low speed process with roll to roll printing is anything else than desirable and would eliminate some of the advantages of the OPV technology in terms of processing. Therefore, a hybrid structure should be avoided. A natural solution to that problem is the use of organic, printed diodes as bypass diodes. There are several reports and types of organic diodes.¹⁹⁰⁻¹⁹² Naturally, the most desirable solution is the use of bypass diodes which are based on the same process materials as the photovoltaic modules themselves, i.e. based on the same electrode and semiconductor materials.

In the following, design requirements for organic bypass diodes are discussed which are essential to address module shading issues for OPV modules. First, the bypass diodes have to be integrated in the flexible OPV modules without or with only little additional processing steps. Second, the diode characteristics of the bypass diode must fulfil requirements to overcome shading effects. That point will be elaborated in more detail later when the turn on bias values of various diode technologies are compared with each other. The proper choice of the organic semiconductor and the electrodes will determine the performance of the bypass diodes. Third, there is the process compatibility. Being able to use the same semiconductor for the bypass diodes which is also used for the active layer of the solar cells allows for a “one colour” printing process. Naturally, the use of inverse interconnected organic solar cells is the most attractive concept to overcome shading in OPV modules. Therefore, non-illuminated organic solar cells in reverse operation are used as bypass diodes to address the goal of a fully organic based structure (OPV module plus organic bypass diodes).

As an example, a module with 9 single cells connected in series is discussed as an example here which can be extended to more cells analogical. The difference to modules with a varying number of cells is the reverse voltage applied on the shaded cell. This reverse voltage is proportional to the number of non-shaded cells within a module. It is shown in the

following paragraphs that organic solar cells are suitable for bypass diodes in OPV modules. The properties of an organic solar cell operated as bypass diode are discussed in detail. Organic bypass diodes are compared to the conventional inorganic diodes based on Silicon (Si) and Germanium (Ge) semiconductor technology.

Figure 4-8 (a) compares the dark J-V-curves of the organic, a Ge and a Si bypass diode. The 3 diodes differ in their core parameters, namely the threshold voltage, the J-V characteristic in injection mode and the leakage current.

The characteristics of the diodes are a crucial parameter for the decision whether they can be applied as bypass diodes. The Ge diode has the lowest injection current, while the organic diode shows the highest leakage current. Note that this is an atypically large leakage current for organic solar cells and diodes. OPV cells with excellent leakage currents in the $\mu\text{A}/\text{cm}^2$ regime from -1 V till -5 V are investigated and processed in this work. Too high leakage currents of the bypass diode induce power losses when the module is operated in normal conditions. The magnitude of the power loss in normal operation is the diode's leakage current at the voltage provided by the non-shaded solar cell in parallel multiplied with the corresponding voltage. However, it is decided to work with an average leaking organic diode as bypass diode to better understand the induced loss mechanisms.

For the shading experiments a single cell within a module is shaded by a black card and a bypass diode is circuited anti-parallel to the shaded cell under investigation.

Figure 4-8 (b) shows the current-voltage characteristics of a flexible 9 stripe OPV module with and without shading. For reference, the module characteristics are compared to the same module when only 8 cells are contributing, i.e., the last cell of the module, which intentionally is shaded, is externally shorted. The shading test confirms organic modules as Type I modules. The leakage current of the cells under reverse bias is insufficient to pass by the photovoltaic power of the non-shaded part of the module. As a consequence, the whole module is shut down, with the power being limited by the shaded cell. Figure 4-8 (c) shows the situation of a partially shaded 9 stripe module bypassed by an organic, a Ge or a Si based bypass diode.

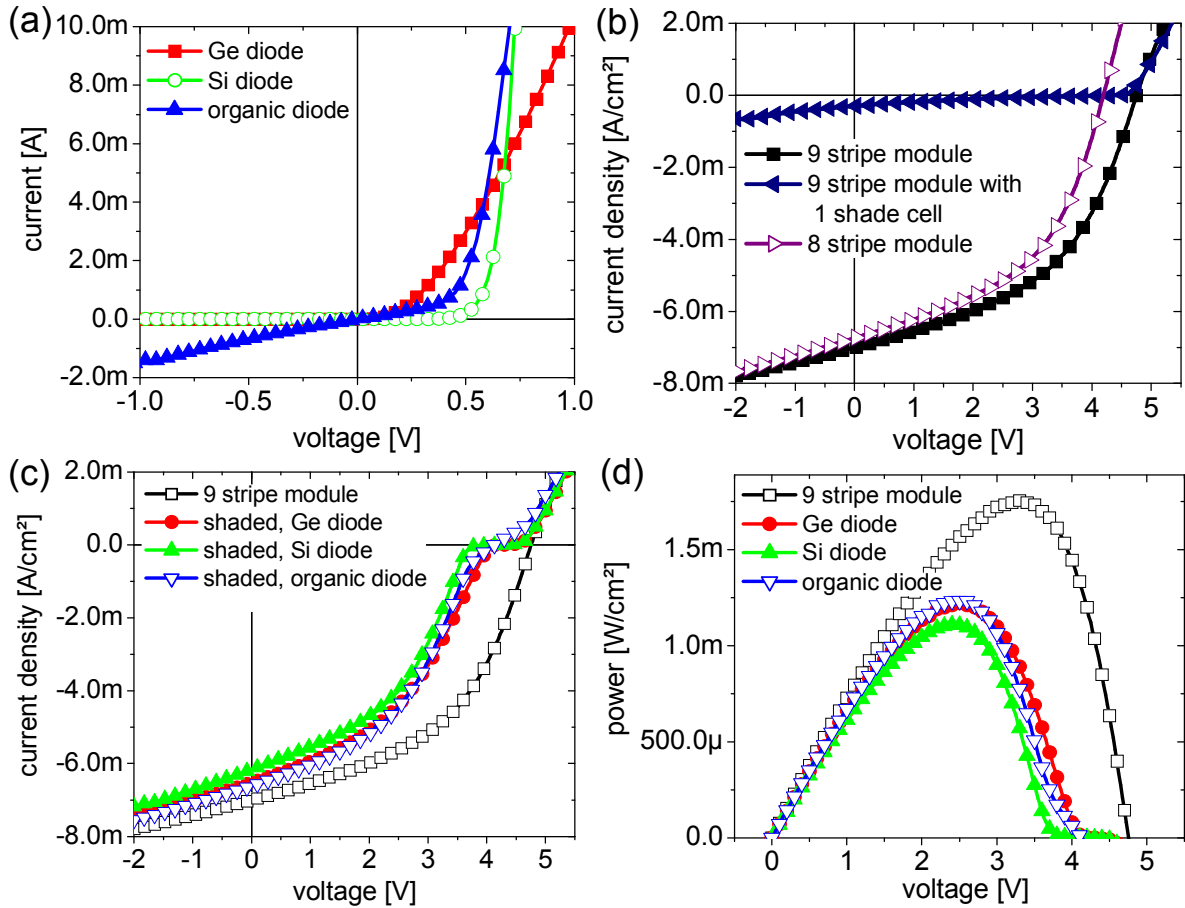


Figure 4-8: (a) Dark J-V characteristic of an organic, a Ge and a Si diode. (b) J-V characteristics of a 9 stripe flexible OPV module with and without shading. For reference, the module characteristic is compared to the same module when only 8 cells are contributing. The last cell of the module is externally shunted. (c) Light J-V-curves and (d) power output-voltage plot of a shaded 9 stripe module when the shaded cell is bypassed by an organic, Ge and Si diode. As reference the non-shaded 9 stripe module is depicted.

The figure of merit for the bypass diodes is the power output of the shaded module under MPP operation. This is depicted in Figure 4-8 (d), where the power generation for the module with the various bypass diodes is compared to the one of the unshaded module which has a power output of 1.76 mW/cm^2 under MPP operation. The significant loss in the power output of the shaded flexible OPV module can be reduced significantly with a bypass diode. The power loss for the module without a bypass diode is as high as 99 %. Using an organic

bypass diode, this loss is reduced to ca. 30 % (1.23 mW/cm^2). Similar values for the power loss are found when inorganic diodes are used as bypass diode which in turn qualifies organic diodes as bypass diodes. The theoretical minimum power loss due to shading in a 9 stripe module is 11 % (1.57 mW/cm^2), which is the geometrical area loss from the shaded cell, given that the bypass diode does not cause any electrical losses. This theoretical optimum is shown in Figure 4-8 (b) by the J-V-curve of a 9 stripe module with only 8 stripes operated. However, bypass diodes can reduce the performance of non-shaded modules for two reasons. First, they occupy some area on the front side of the module. On the other hand, their leakage current reduces the module photocurrent at MPP. The necessary size of the bypass diode is determined by its current carrying capacity in injection, which has to be large enough to let the current pass under forward bias. The necessary voltage at which the bypass diode is able to pass by the photocurrent of the shaded module is taken from the photo voltage of the module under operation and is thus lost for the module operation. The bypass diode must be adjusted at the voltage which is required to pass by the photocurrent; therefore, a low turn on voltage is essential to reduce the bypass diode losses under shading. Naturally, this voltage is higher for small area organic bypass diodes compared to large area organic bypass diodes. Consequently, large area bypass diodes are favourable for little losses in the module voltage under shading. The same time, however, the geometrical fill factor of the device and thus the power output/square of the module is reduced, since it is printed on the module's front side. A 2 cm^2 bypass diode results in a voltage drop of 0.62 V, a bypass diode sized 1 cm^2 results in a voltage drop of 0.7 V. These values are derived from the J-V characteristics in injection mode of the organic bypass diodes as depicted in Figure 4-8 (a).

The impact of the turn on voltage of the bypass diode on the module losses under shading is summarized in Figure 4-9. Another important parameter to determine the optimum bypass diode is the leakage current. Under normal, non-shaded operation, the leakage current of the bypass diode is a loss for the photocurrent. Typical leakage currents of optimized and investigated organic solar cell structures are $\sim 50 \mu\text{A}/\text{cm}^2$ at -0.5 V. For a solar cell operated at its MPP at 450 mV, such a bypass diode results in a permanent ohmic loss of $25 \mu\text{W}/\text{cm}^2$ or less. Compared to the AM 1.5 power output of a P3HT/PCBM solar cell with $\sim 2 - 4 \text{ mW/cm}^2$, this is a loss smaller than 1 % when the active area of the bypass diode and the solar cell are equal. This loss is further decreased when the geometrical size of the organic bypass diode is reduced.

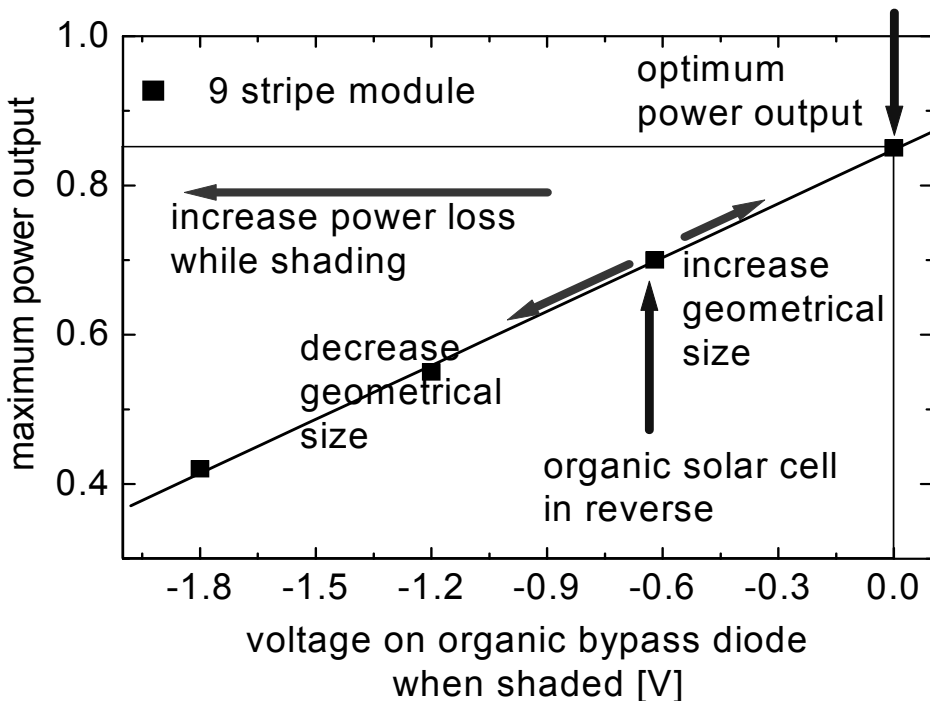


Figure 4-9: Normalized power output versus the voltage that applies on the bypass diode. This voltage is needed to bypass the current of the 8 non-shaded cells. The optimum power output and the power output of the module when the organic bypass diode bypasses the current are depicted. The other data points correspond to organic diodes with higher threshold voltages. For higher voltages on the bypass diode the power loss increases. An increase of the geometrical size of the bypass diode decreases the power loss. A decrease of the geometrical size of the bypass diode increases the power loss. Losses by the geometrical size of the bypass diodes are neglected in this graph.

Note that good organic diodes have leakage currents in the very low $\mu\text{A}/\text{cm}^2$ regime, in which case the organic bypass diode losses for a solar cell will be negligibly small. Geometrical fill factor losses by the size of the bypass diode are neglected in this calculation. In this chapter it is presented that organic solar cells in reverse polarity are excellent bypass diodes for organic PV modules preserve the advantages of this technology. The module power losses under normal operation due to an organic bypass diode are well below the 1 % regime.

4.3.2 Summary

The shading of organic PV modules is investigated. It is found that OPV modules show Type I behaviour, where the whole module will be shut down if one cell becomes shaded (99 % power loss). It is further demonstrated that organic bypass diodes are the most elegant and practical technology to reduce the shading losses to ~30 %. No substantial advantage is found when using inorganic diodes (Si and Ge) as bypass diodes. In the sum of the properties, organic bypass diodes are shown to be superior to their inorganic counterparts:

- The module losses under shading were as low as for the inorganic diodes.
- The leakage current and current carrying capacities are sufficient to keep the module losses well below 1% under normal operation.
- Highly favourable for a one colour printing process.

4.4 Type of Shunts in Organic Photovoltaic

In this sub-chapter the origin of the shunt (area of low shunt resistance) in OPV cells is discussed and a method developed to identify the defective layers responsible for the hot spots. Information about the origin of the shunt is necessary to further improve OPV cells, decrease and guarantee low leakage current cells which importance is discussed in chapter 4. In chapter 4.1 the dark lock-in thermography (DLIT) amplitude image of OPV cells is discussed and an investigation in hot spots is presented. The cause of the shunts can either be defects in the photo-active layer (bulk shunt), or in one or both the interfacial layers (interface shunt). For definition of these two types of shunts the active area of the solar cell is virtually divided in little pixels. A pixel consists of the semiconductor layer, the interfacial layers and the electrode materials. Each pixel (“each single solar cell”) is assigned to an equivalent circuit, with all the pixels connected in parallel. The schematic is illustrated in Figure 4-10, whereas the pixels show a resistance for each layer. The power dissipation within a pixel is proportional to the square of the voltage divided by the resistance of the pixel. The voltage applied on each pixel is same. Therefore, the lower the resistance of the pixel the higher the heat dissipation within a pixel compared to the others. The resistance of a pixel is the sum of the resistances of the interfacial layers and the photo-active layer. For an interface shunt the photo-active layer is intact and one or both interlayers of the pixel are affected or missing. A typical example of an interface shunt would be a non-homogeneous

coating of the interfacial layers. For a bulk shunt, the photo-active layer is affected or missing and the interfacial layers can be either affected. A typical example of a bulk shunt would be a direct contact of the two electrode materials at a given area.

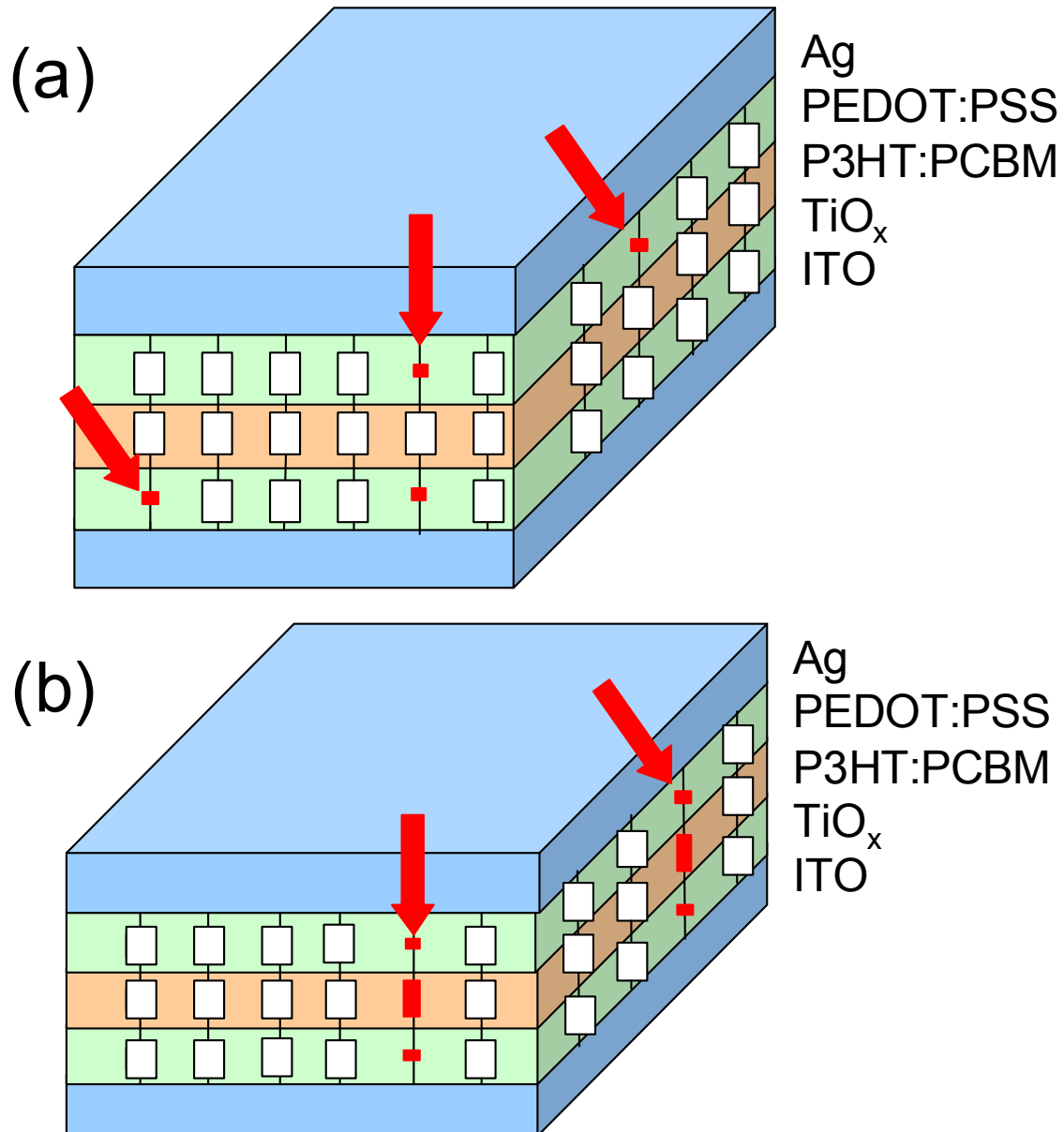


Figure 4-10: Schematic illustration of a device with different types of shunts. The device is virtually divided in little pixels with all the pixels connected in parallel by the electrode materials. The resistance of each layer within one pixel is illustrated by a white square. The whole resistance of a pixel forms the resistance of the interfacial layers (PEDOT:PSS, TiO_x) and the one of the photo-active layer (P3HT:PCBM). Shunts (a lower shunt resistance) are illustrated by a small filled red square marked by arrows. (a) Illustrates interface shunts. (b) Illustrates bulk shunts.

4.4.1 Origin of the Shunt in Organic Photovoltaic Cells

In this work the combination of high resolution LBIC and DLIT measurements is suggested to distinguish between bulk and interface shunts. With DLIT measurements the position and size of a shunt within an OPV cell can be determined. LBIC measurements resolve whether a photocurrent is locally generated within the shunt or not. Therefore, the geometrical resolution of the measurement methods has to be higher than the size of the shunt. Under this assumption, bulk and interface shunts can be distinguished as follows:

- (a) For an interface shunt the photo-active layer material is intact and charge carriers are created within the shunt under illumination. The photo-generated carriers are (partly) extracted to the electrode materials contributing to a photocurrent. Thus the shunt is not clearly visible in the LBIC map as long as R_p of the photo-active layer is large compared to R_s of the electrode materials. For R_p in the range of R_s or lower many photo-generated charge carriers recombine over R_p . Therefore, the external photocurrent which is visible in the LBIC signal is reduced by the amount of charge carriers recombining over R_p . In the case of an interface shunt the current through the shunt has to be transported through the photo-active layer of the size of the shunt, neglecting recombination. Therefore a minimal shunt size can be estimated by the conductivity of the photo-active layer. Provided that the shunt size is smaller than the minimal needed size to transport the current an interface shunt can be excluded.
- (b) For a bulk shunt the photo-active layer material is missing or has defects. Therefore no photocurrent is generated within the shunt. The LBIC map shows a spot in the size of the shunt with a photocurrent of zero.

In the following the suggested and developed method to distinguish between bulk and interface shunt is presented for an exemplarily hot spot:

Figure 4-11 shows the DLIT amplitude image of an OPV cell with only 1 circular shunt. The cell is pulsed with a rectangular voltage with an amplitude of -0.4 V.

To identify the size of the shunt the geometrical resolution of the DLIT setup is increased by the use of magnification optics combined with high lock-in frequencies. For higher lock-in frequencies the heat diffusion is reduced and the visible heat dissipation is limited to the shunt itself and a small area around the shunt.¹⁹³

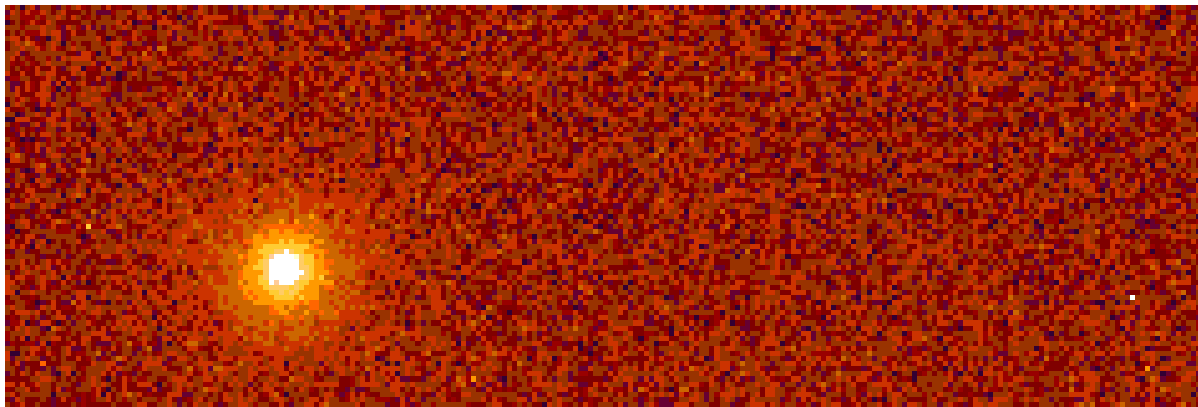


Figure 4-11: DLIT amplitude image. Image size represents active area of an organic solar cell in the size of 2.5 mm x 10 mm. Light colours corresponds to higher temperatures. Light spot is a hot spot.

With magnification optics 1 pixel of the IR detector corresponds to an area of approximately $11 \mu\text{m} \times 11 \mu\text{m}$. Figure 4-12 shows the amplitude signal of the single hot spot visible in Figure 4-11. The DLIT amplitude image of the hot spot is measured at lock-in frequencies of 10 Hz and 44.56 Hz. For both lock-in frequencies a plateau in the amplitude signal with a diameter of approximately $80 \mu\text{m}$ is observed despite different heat diffusion lengths. This value is taken as the estimated diameter of the shunt. The estimation of the shunt diameter might contain a certain error. A higher shunt diameter of 4 - 6 pixels is possible which would result in a shunt diameter of up to $140 \mu\text{m}$. A lower shunt size than $80 \mu\text{m}$ also cannot be fully excluded.

The leakage current is $110 \mu\text{A}$ at -0.4 V for the discussed cell. From the DLIT amplitude image in Figure 4-11 the heat is dissipated within one hot spot. Other current paths beside the shunt are estimated in the following: Several cells are monolithically integrated on a substrate. This leads to a cross-conductivity between the bottom and the top electrodes. A cross-conductivity below $1 \mu\text{A}$ is found. The saturation current of the diode is determined by equation 2.1 to well below $1 \mu\text{A}$. Therefore, the cross-conductivity and the saturation current of the diode can be neglected. The leakage current of the cell is driven through the shunt, i.e. $110 \mu\text{A}$ for the investigated cell. The conductivity of the photo-active layer P3HT:PCBM is measured in ambient air based on an interdigitated contact structure presented in chapter 2.5.2. The conductivity is determined to 10^{-4} S/cm . This value can vary depending on the doping level of P3HT:PCBM, contact resistances of the measurement setup etc..

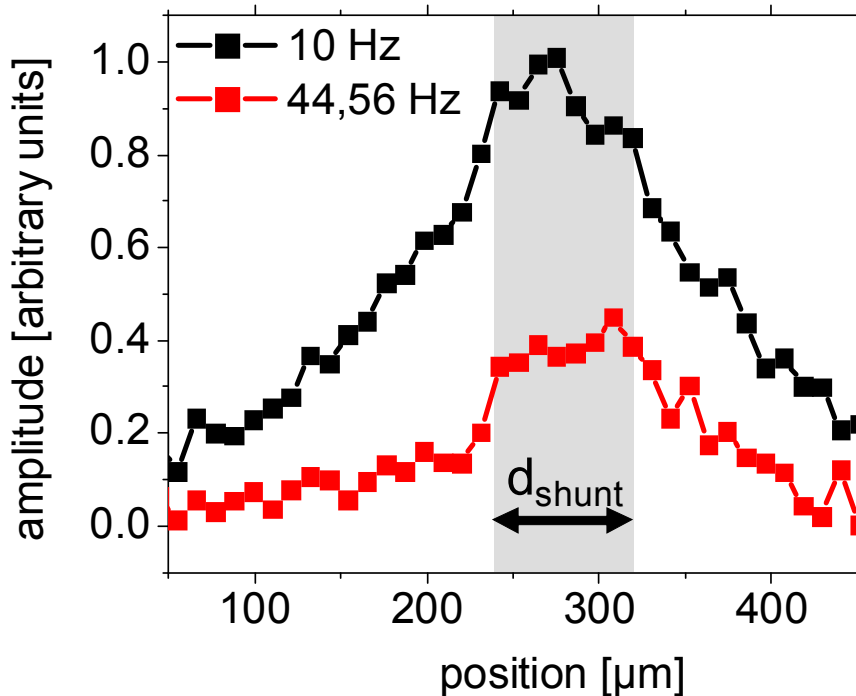


Figure 4-12: Amplitude signal of the hot-spot presented in Figure 4-11. The hot spot is measured with help of magnification optics. 1 pixel of the IR detector corresponds to an OPV cell area of $11 \mu\text{m} \times 11 \mu\text{m}$.

With a conductivity of 10^{-4} S/cm and an applied voltage of 0.4 V a shunt diameter of $90 \mu\text{m}$ is necessary to transport the leakage current through the photo-active layer according equation 2.3.3. This shunt size varies depending on the measured conductivity of P3HT:PCBM.

Figure 4-13 (a) shows the LBIC map of the investigated OPV cell with a step size of $10 \mu\text{m} \times 10 \mu\text{m}$. The spot size of the laser is below $10 \mu\text{m}$. The position where a hot spot is identified by DLIT measurements is highlighted with a circle. The magnification of this area is shown in Figure 4-13 (b). The LBIC map of the OPV cell shows large inhomogeneities in the photocurrent over the whole device. The area where the hot spot is identified by DLIT measurements shows a photocurrent in the LBIC map. The value of the photocurrent is well within the average photo-current of the surrounding area. The local photocurrent is not reduced to zero which would be the case for a bulk shunt.

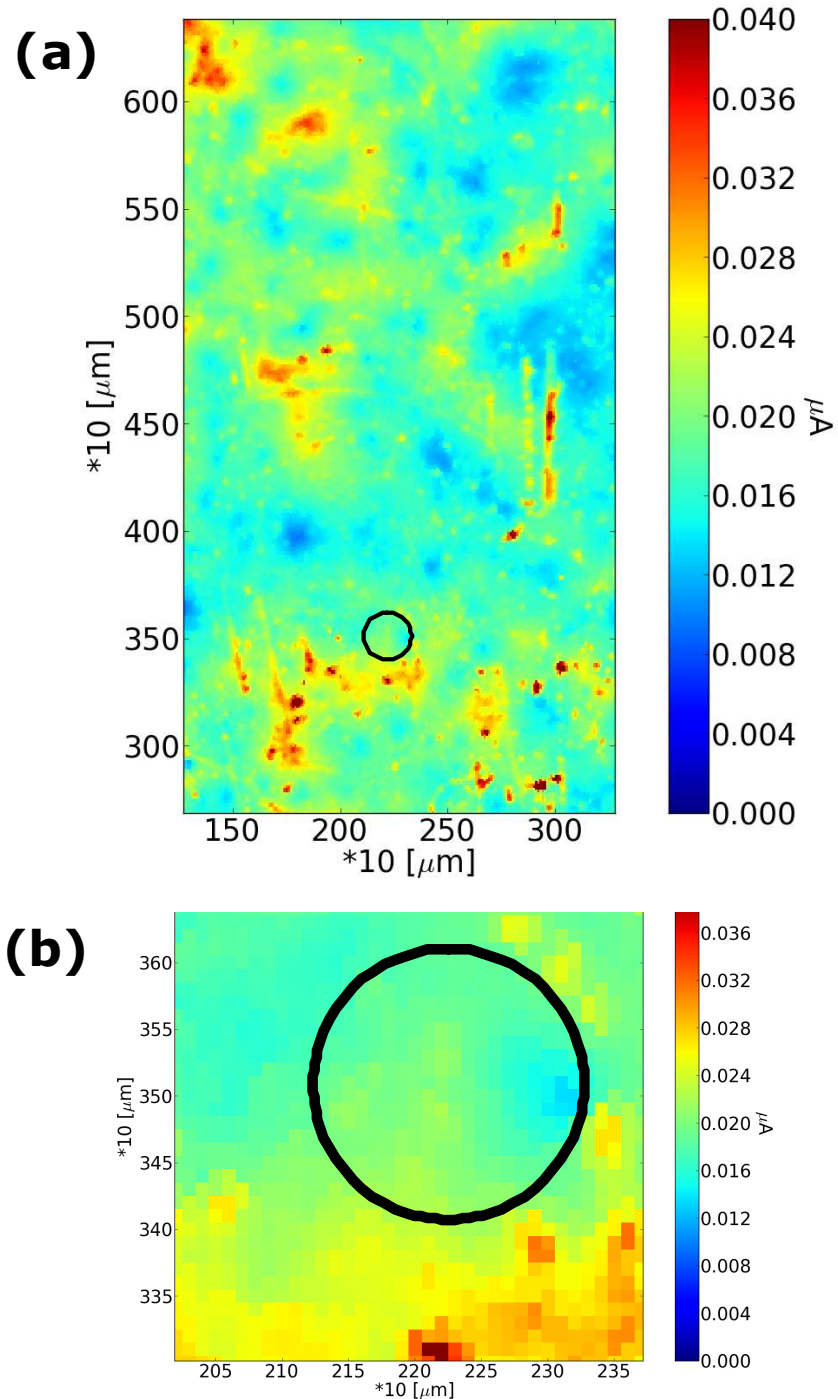


Figure 4-13: LBIC maps with a step size of $10 \mu\text{m} \times 10 \mu\text{m}$. The black circle surrounds the position of the shunt determined by DLIT measurements. (a) The size of the image is part of the photoactive area of the OPV cell and (b) the magnified LBIC map.

For a shunt diameter of larger than 30 µm a bulk shunt has to be visible in the LBIC map as an area with the photocurrent close to zero. This is not observable in the LBIC map. According to this, the shunt is an interfacial shunt.

In the presented data there is a certain error in the size of shunt and a shunt diameter below 30 µm cannot be clearly excluded. Especially the determination of the area of the shunt from the DLIT amplitude image has some uncertainty. Combined with the fact that the current densities in the shunt area are at the limit of the conductivity of P3HT:PCBM, the presence of an interface shunt is not clearly proved.

But with an estimated shunt diameter of 80 µm and no point with a photocurrent of 0 in the LBIC map with a resolution of 10 µm x 10 µm the shunt is assigned to an interface shunt. The conductivity of the photo-active layer is high enough to transport the current densities through a shunt.

4.4.2 Summary

In summary a method is suggested and developed to distinguish between bulk and interface shunts in OPV devices by combining DLIT and LBIC measurements. For a bulk shunt, i.e. a missing or defective photo-active layer, the photocurrent has to be zero within the shunt. In the case of an interface shunt, i.e. when the photo-active layer is intact, charge carriers are generated within the shunt and extracted (partly) to the electrodes. Knowledge about the exact shunt size is crucial to distinguish between interface and bulk shunt but the estimation of the shunt size can have a large error which makes it difficult. For the exemplarily shown data for the hot spot with a shunt size larger than 80 µm no correlation between the LBIC map and DLIT map is found. The conductivity of P3HT:PCBM is high enough to transport the leakage current of the cell through the shunt. This finding suggests that the discussed hot spot is an interface shunt, i.e. the active layer is intact and the interfacial layers are damaged. Therefore, the improvement of the interfacial layers will improve the shunt resistance of the OPV cell.

The developed technique allows distinguishing between bulk and interface shunts and therefore to determine which layers within an OPV cell have to be optimized for improved shunt resistances which importance is demonstrated in this work.

5 Interface Engineering

A high shunt resistance is found to be essential for OPV including outdoor and indoor applications, reverse bias stability and organic bypass diodes. The first part of this chapter presents that stacking of organic and inorganic interfacial layers leads to improved shunt resistance and device performance. The origin of this improvement is discussed. In the second part of this chapter it is demonstrated that unadjusted interface materials lead to losses in device performance. TiO_x is such an interface material which can be switched by UV irradiation from an unadjusted interface material to an excellent interface material. The origin of this behavior is discussed.

5.1 Interface Modification for Highly Efficient Organic Photovoltaics

In the previous chapter it is shown that one key property to further improve OPV cells such for 1 sun and low light conditions, the reverse bias stability as well as the quality of organic bypass diodes is the shunt resistance. A major contribution here comes from the interface materials, which provide the high selectivity of the contacts and increase the shunt resistance of the device. The electron selective contact, the cathode, is the most challenging interface for the normal as well as for the inverted geometry. For instance, the efficiency of an inverted cell is still below that of a normal cell despite using the same active layer. One reason for this are not well optimized interfacial layers for the inverted structure. Therefore, it is worthwhile to further improve the interfaces to match the PCE of the inverted geometry to the PCE of the normal geometry. Within the investigated interfacial layers for the inverted structure TiO_x is a promising material as electron selective and conducting material. For the reference structure glass/ITO/ TiO_x /P3HT:PCBM/PEDOT:PSS/Ag efficiencies as high as 3.1 % have been reached in this work. Glass is used as the substrate for the evaluation of new interface materials because of its higher transmittance and easier processing. Provided that the conversion temperatures are low enough there are no issues in transferring the process to flex substrates.

5.1.1 Improved Interfaces by Stacking of Solution Processed Organic and Inorganic Layers

The combination of a well performing reference device structure with an additional interfacial layer is investigated. Polyoxyethylene tridecyl ether (PTE) is investigated as additional interfacial layer at the cathode. The aim in stacking of solution processed metal oxide and organic interfacial layers are to create a homogeneous, pinhole free selective contact for electrons improving the shunt resistance. A better contact of the interfacial layers to the active layer or electrode also improves the carrier injection and extraction which results in improved R_s . The modified device structure

Glass/ITO/PTE/TiO_x/P3HT:PCBM/PEDOT:PSS/Ag is presented in Figure 5-1:. For comparison, the reference device Glass/ITO/TiO_x/P3HT:PCBM/PEDOT:PSS/Ag without the organic interfacial layer is also illustrated.

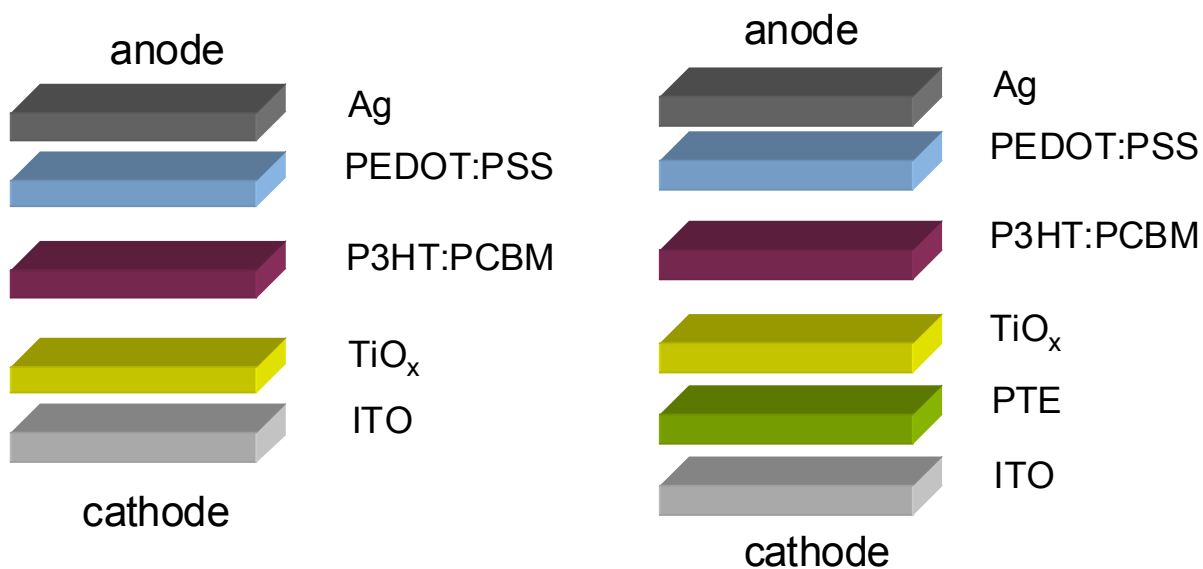


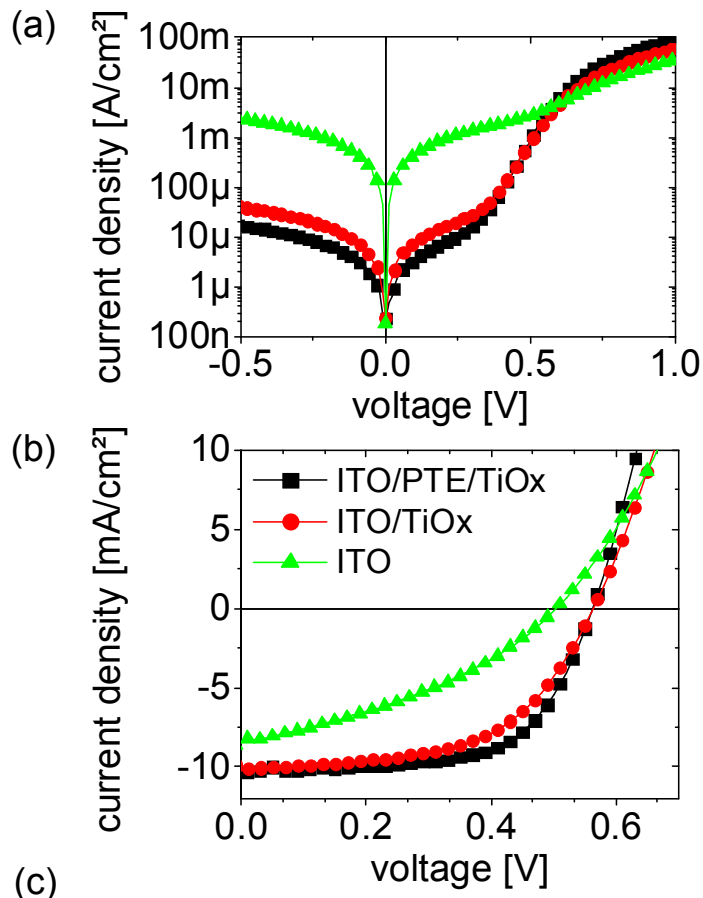
Figure 5-1: Device structure of the inverted OPV structure with and without PTE as electron selective contact.

In the present study, PTE [$C_{13}H_{27}(OCH_2CH_2)_{12}OH$, Aldrich], is used as an organic interfacial layer to modify the interface ITO/TiO_x (see Figure 5-1). The organic interfacial layer (0.1 wt % in water) is doctor bladed onto the glass/ITO substrate and results in an ultrathin layer of ~3nm as estimated from UPS measurements. Since the detectable depth of analysis by

UPS is in the range of 1 – 10 nm (depends on the elements) and the ITO beneath the PTE is detectable the layer thickness of PTE can be estimated.

Devices with PTE as interfacial layer between ITO and TiO_x (Glass/ITO/PTE/TiO_x/P3HT:PCBM/PEDOT:PSS/Ag) are compared to devices without PTE (Glass/ITO/TiO_x/P3HT:PCBM/PEDOT:PSS/Ag) and to devices without any electron selective contact, i.e. the semiconducting layer processed directly on ITO (Glass/ITO/P3HT:PCBM/PEDOT:PSS/Ag).

Figure 5-2 shows representative J-V characteristics of the solar cells in the dark (a) and under illumination (b).



	PCE [%]	FF [%]
— ITO/PTE/TiOx/blend/PEDOT:PSS/Ag	3.6	64
— ITO/TiOx/blend/PEDOT:PSS/Ag	3.2	55
— ITO/blend/PEDOT:PSS/Ag	1.6	35

Figure 5-2: Representative dark (a) and light (b) J-V characteristics of the solar cells under study.
(c) Table of PCE and FF of the presented J-V characteristics.

The dark J-V curve for the inverted solar cell without an electron selective interfacial layer (Glass/ITO/P3HT:PCBM/PEDOT:PSS/Ag) shows low current in the forward direction and a high leakage current in the reverse direction. ITO alone does not provide an electron selective contact for the extraction of electrons and blocking of holes. Recombination of charge carriers at the interface ITO/P3HT:PCBM is also possible. By using low temperature solution processed TiO_x (Glass/ITO/ TiO_x /P3HT:PCBM/PEDOT:PSS/Ag) as interfacial layer, the electron selectivity of the bottom contact improves significantly. A high current in the forward direction as well as low leakage currents are achieved. The improved carrier selectivity is also reflected in the FF of the corresponding cells. The best selectivity (highest injection current and lowest leakage current) is achieved for solar cells employing a combination of PTE and TiO_x (Glass/ITO/PTE/ TiO_x /P3HT:PCBM/PEDOT:PSS/Ag). This experimental observation is confirmed with J-V curve analysis according to the one-diode model. Exemplarily, the insertion of a thin PTE layer reduces the serial resistance of the solar cell from $3 \Omega\text{cm}^2$ to $1 \Omega\text{cm}^2$ and increases the shunt resistance from $14 \text{k}\Omega\text{cm}^2$ to $31 \text{k}\Omega\text{cm}^2$ for the OPV cell with the highest power conversion efficiency illustrated in Figure 5-2. The combination of reduced serial resistance and increased shunt resistance is reflected in the higher FF of those diodes with PTE.

Figure 5-3 summarizes the performance parameters of the solar cells. Data are presented in box plots (see Figure 5-3). Each variation, i.e. no electron selective contact, TiO_x and PTE/ TiO_x , consists of 16 solar cells. 50 % of the cells with TiO_x electron selective contact have a PCE of 3.2 % or higher. Solar cells without any electron selective layer have a median PCE in the range of 1.6 %. The best device performance is achieved with a combination of PTE and TiO_x as electron selective contact, with 50 % of the cells having a PCE higher than 3.6 %. Data presented here are from one experimental run but have been reproduced in several runs independent from each other.

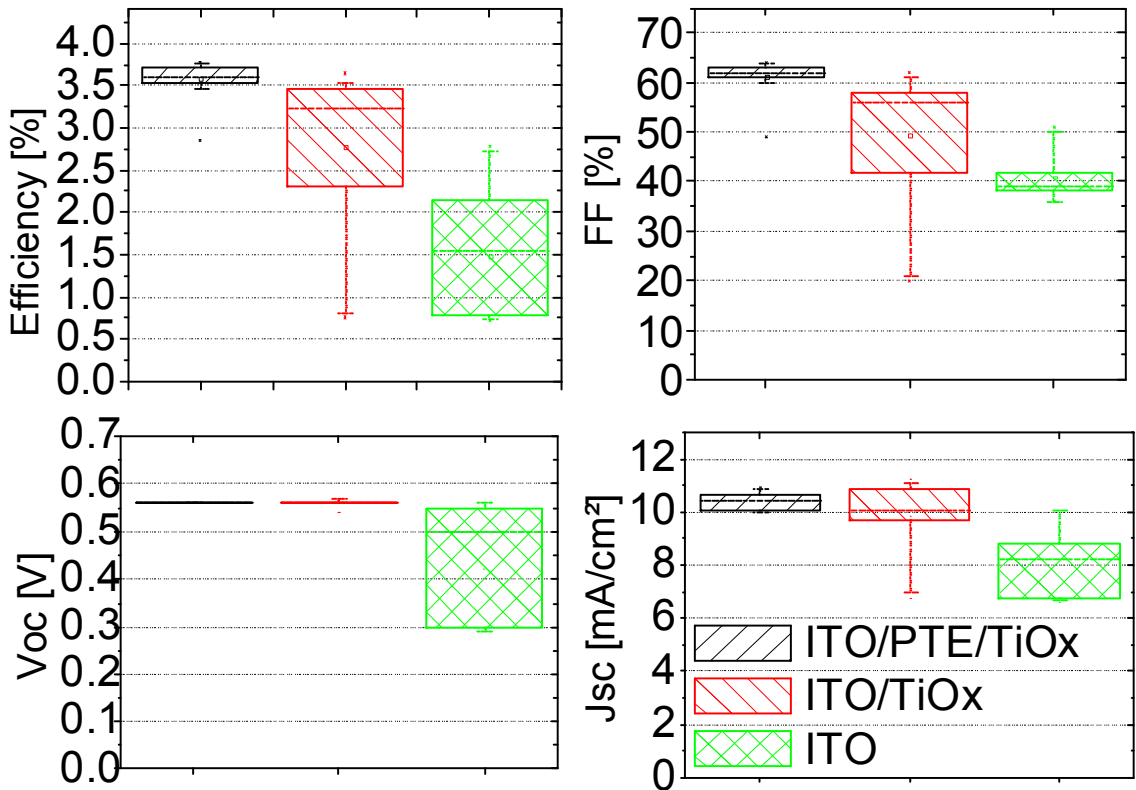


Figure 5-3: Comparison of the power conversion efficiency, fill factor, open circuit voltage and short circuit current density for the solar cells under study. Data are presented in box plots.

5.1.2 Origin of the Improvement with PTE

In this chapter the origin of the improvement of devices structure Glass/ITO/PTE/TiO_x/P3HT:PCBM/PEDOT:PSS/Ag compared to devices without the organic interfacial layer (Glass/ITO/TiO_x/P3HT:PCBM/PEDOT:PSS/Ag) is discussed. 3 different possible reasons are considered and investigated:

- (a) Chemical interaction of PTE with TiO_x. To investigate a possible chemical interaction between TiO_x and PTE, XPS measurements are performed.
- (b) Modification of the work function of the interfacial layers. The work functions of the interfaces are measured by UPS and V_{bi} is determined from J-V curve analysis.

(c) Change in the morphology of TiO_x caused by a different coating surface. AFM images of the TiO_x surface in different configurations are measured to identify whether the surface morphology changes.

Several measurements to clarify the origin of the improvement by the incorporation of PTE between ITO and TiO_x are performed. XPS measurements provide information on the chemical interaction between the PTE and TiO_x . The investigated structures are processed in ambient atmosphere and then transferred into a vacuum chamber for XPS measurements. Thus the surfaces of the investigated samples are covered by a ubiquitous surface contamination layer which typically consists of hydrocarbons and to a less extent of species containing oxygen and other trace elements. Figure 5-4 presents the XPS spectrum for a binding energy from 280 to 292 eV for the investigated interfacial layers ITO/PTE/ TiO_x and ITO/ TiO_x .

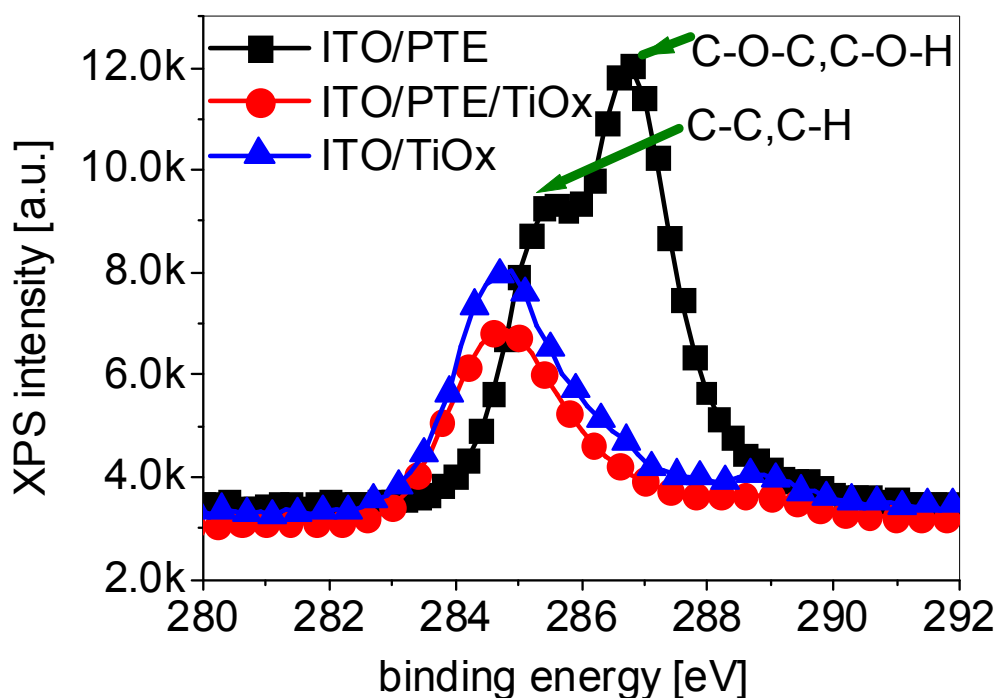


Figure 5-4: Binding energy vs. counts for the structures under investigation measured by XPS.

The XPS spectrum of the structure ITO/PTE shows peaks related to C-C, C-H, C-O-C and C-O-H bonds. These peaks originate from PTE since these peaks are not visible for the other structures which are also processed in ambient atmosphere. From the strength of the In peak

before and after coating PTE on ITO the thickness of PTE is estimated to 3 nm (not shown). The peak at 284.8 eV is present in both samples and stems from atmospheric contaminations and from residual alkoxy ligands from the sol-gel precursor which is not completely removed by the hydrolysis reaction in the employed low-temperature process. The pattern of PTE is not visible when TiO_x is coated on top which is indicative of a uniform coverage of the oxide. Figure 5-5 presents the XPS spectra for a binding energy from 454 to 468 eV for the investigated interfacial layers ITO/PTE/ TiO_x and ITO/ TiO_x .

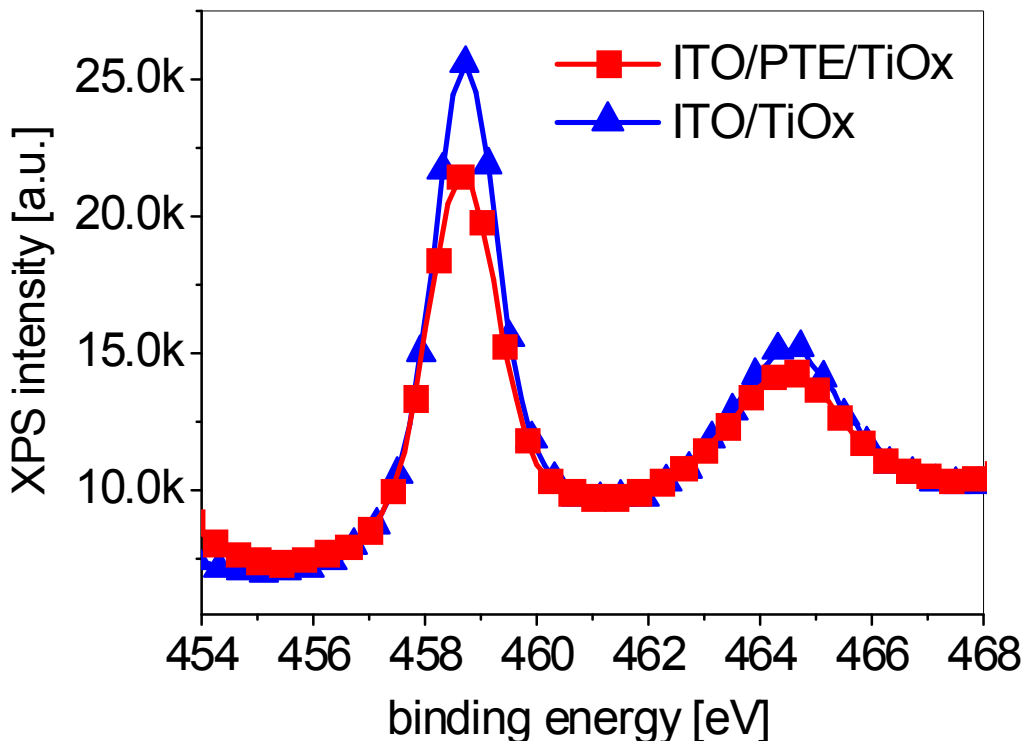


Figure 5-5: Binding energy vs. counts for the structures under investigation measured by XPS.

Because the energetic position of the XPS signal of TiO_x in the spectra of ITO/ TiO_x and ITO/PTE/ TiO_x are very similar in this regime there is no evidence for an influence of a chemical reaction between PTE and TiO_x which propagates throughout the TiO_x layer. Information on deeper TiO_x slices is not accessible with XPS. However, it is expected though that the hydroxyl group and the ether moiety of the PTE coordinatively interact with TiO_x at the interface.

To further investigate the effect of the PTE interfacial layer on ITO/PTE/ TiO_x interface photogenerated-current-voltage measurements are performed. The photogenerated-current-

voltage measurements reveal no difference in V_{bi} for the devices using ITO/TiO_x and ITO/PTE/TiO_x as electron selective contact. For both cases the V_{bi} is found to be 0.64 V.

UPS measurements of the work function of the TiO_x layers with and without PTE interlayer are presented in Figure 5-6.

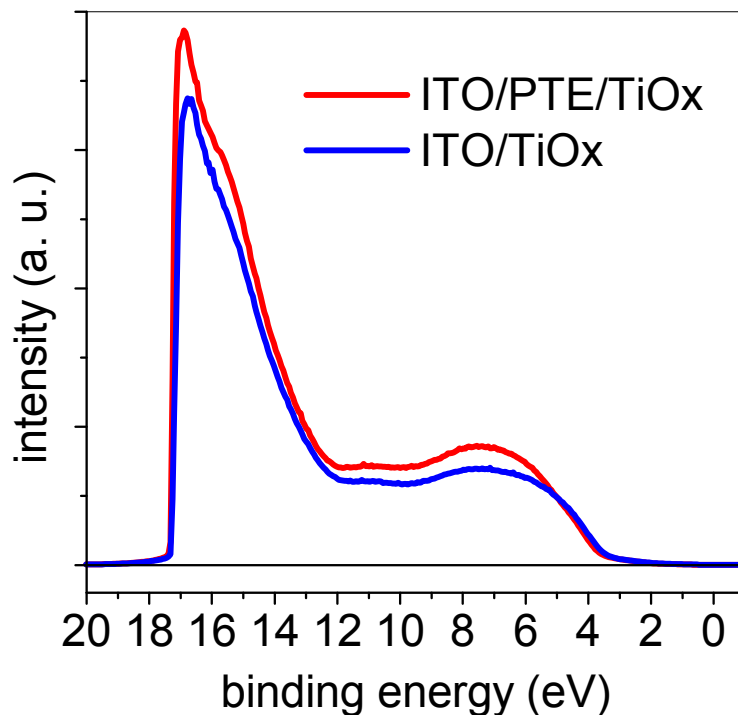


Figure 5-6: Binding energy vs. counts for the structures under investigation measured by UPS.

The HeI line with energy of 21.2 eV is used. Therefore, the work function of both electrodes is 4.1eV in the dark. The results suggest that the underlying mechanism of the improved electron selectivity by incorporation of PTE between ITO and TiO_x interface (ITO/PTE/TiO_x/P3HT:PCBM/PEDOT:PSS/Ag) can be related to an improvement of the overall surface quality (roughness and/or surface energy) of the ITO/PTE/TiO_x bottom electrode since no chemical interaction or change in the work function between the PTE and TiO_x is observable. Indications that the surface morphology of the TiO_x is altered when coated on the top of PTE compared to ITO are found from atomic force microscopy studies. (Figure 5-7). Both pictures show features in the topography which can be described as peaks with valleys in between.

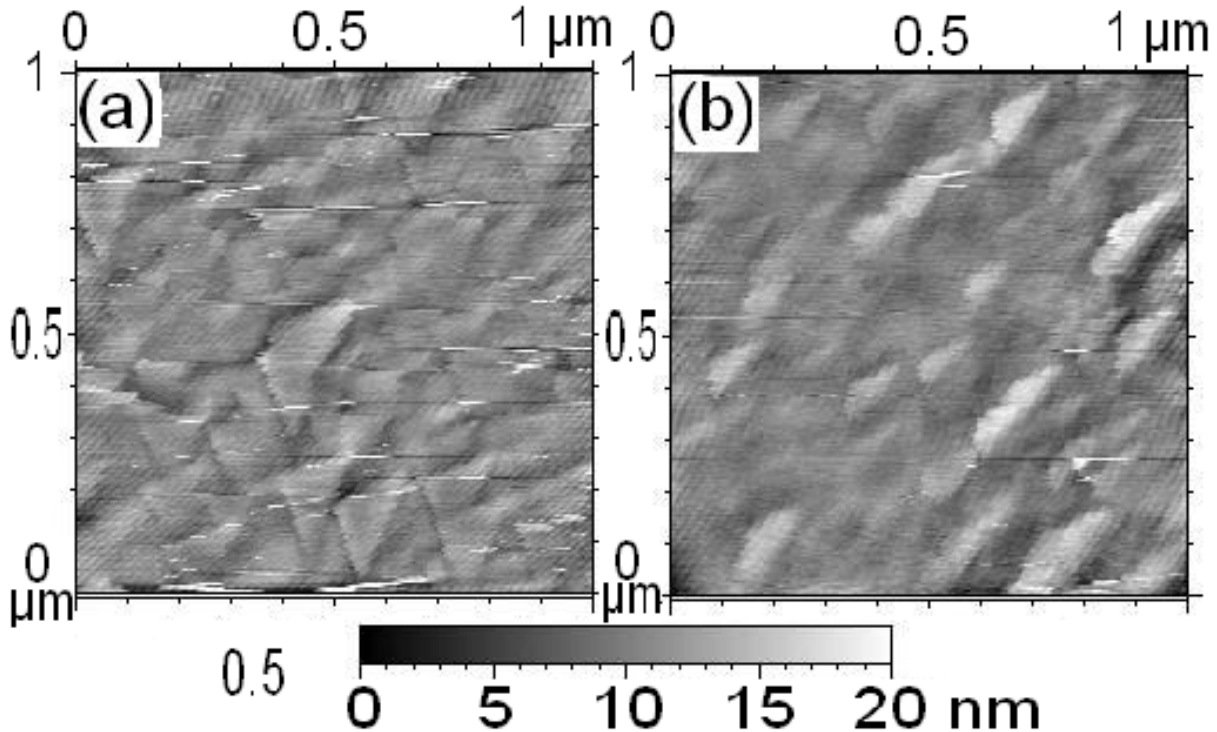


Figure 5-7: Topographic atomic force microscope image (contact mode) of the TiO_x surface coated on top of ITO (a) and on top of PTE (b). The scan range is $1 \mu\text{m} \times 1 \mu\text{m}$.

Although the surface roughness of the TiO_x coated on the top of ITO and PTE has the same rms value of 2.2 nm, the distance between the peaks and valleys is different. The improvement in the electron selectivity of the ITO/PTE/ TiO_x bottom electrode is attributed to the PTE coating step, allowing for a better wetting of the TiO_x precursor solution and therefore a more intimate interface with the photoactive layer. This more intimate interface and homogeneous interfacial layer results in the reported improvement in the power conversion efficiency, the increased shunt resistance and decreased serial resistance.

5.1.3 Summary

In summary, a PTE interface modification is beneficial for the electron selective bottom contact layer TiO_x . The improved electron selectivity with the incorporated PTE interfacial layer between ITO and TiO_x is reflected in higher FF, higher R_p and reduced R_s of the OPV structure Glass/ITO/PTE/ TiO_x /P3HT:PCBM/PEDOT:PSS/Ag. No change in the work

function or chemical interaction between TiO_x and PTE is found. The change of the surface morphology of TiO_x when coated onto PTE suggests a better wetting of the TiO_x precursor when coated on top of PTE. By incorporating a PTE interfacial layer between ITO and TiO_x , a PCE of 3.6 % for inverted bulk-heterojunction solar cells has been achieved compare to 3.2 % without PTE as additional interfacial layer.

5.2 S-Shape Current-Voltage Characteristics in Organic Photovoltaic Cells

In this chapter the effect of UV irradiation on the FF of OPV devices is discussed. Without UV irradiation devices show an S-shape J-V characteristic, i.e. the current density for voltages around V_{oc} is limited when compared to devices with UV-VIS irradiation. The dynamics of the cell parameters with and without UV irradiation is discussed and these results are correlated with the change in the properties of the TiO_x layer. Based on these findings a model is presented which allows simulating and describing the J-V characteristic with and without an S-shape. Experimental results are presented in which the interfaces are modified in such a way, that both, weakly and strongly pronounced S-shaped J-V characteristics can be generated.

5.2.1 Introduction

All J-V characteristics presented in the previous chapters have been taken after 20 min of UV-VIS irradiation. In this chapter the J-V characteristics of OPV cells with and without UV irradiation are discussed and analyzed. Figure 5-8 presents the J-V characteristics of OPV cells with and without UV irradiation, i.e. with and without S-shape J-V characteristics. The presented J-V-curves discussed in chapter 5.1 are recorded after 20 min of UV-VIS radiation. The illumination of these solar cells with 20 min of UV-VIS radiation is necessary to reach the reported efficiency of up to 3.1 % and a FF of 55 % for the device structure Glass/ITO/ TiO_x /P3HT:PCBM/PEDOT:PSS/Ag. With the improved device structure Glass/ITO/PTE/ TiO_x /P3HT:PCBM/PEDOT:PSS/Ag efficiencies of up to 3.6 % and FF of 64 % are reached. Without UV-VIS irradiation the performance of the OPV cells is clearly limited. Prior to the measurement without UV radiation the OPV cell is stored in the dark. The transmission of this UV filter is shown in Figure 5-9. After that, the J-V characteristic is recorded under a solar simulator.

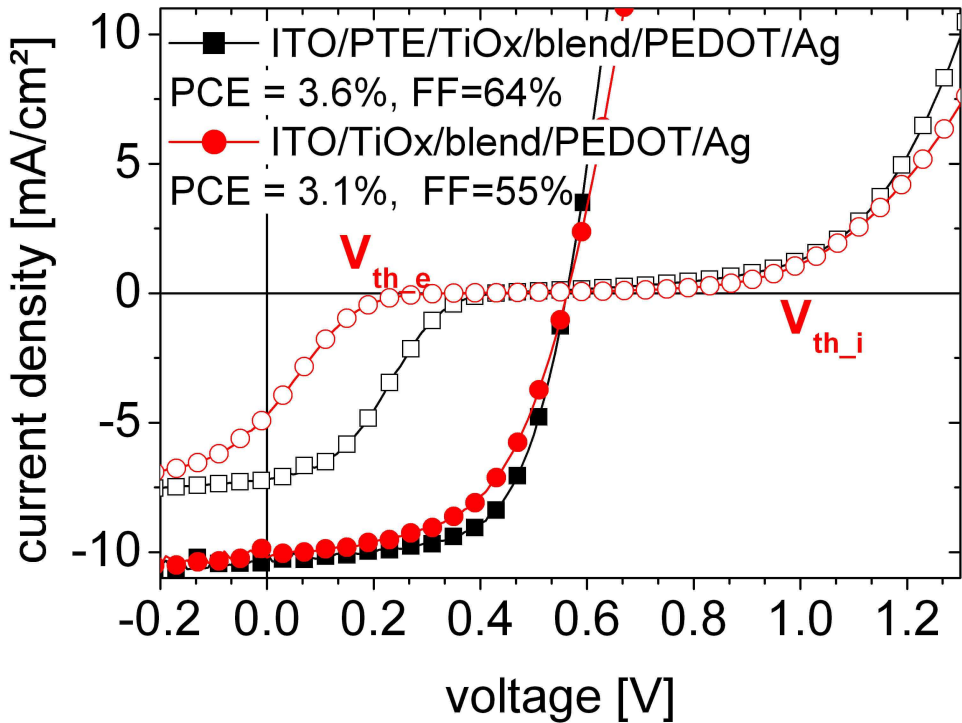


Figure 5-8: J-V characteristics of OPV cells with the device structures ITO/PTE/TiO_x/P3HT:PCBM/Pedot/Ag (black squares) and ITO/TiO_x/P3HT:PCBM/Pedot/Ag (red circles) with (solid symbols) and without (open symbols) 20 min UV-VIS irradiation.

The significantly lower current of the non-UV irradiated samples is a result of the UV filter foil which is laminated on a PET carrier film which has a poor transmission in the VIS spectrum.

Without UV-VIS irradiation the devices show a clear S-shape J-V characteristic. Charge injection and extraction are strongly limited for voltages close to V_{oc} compared to devices with UV-VIS irradiation. As a consequence, little injection current at +1V and small FF are good indications for the appearance of the S-shape J-V characteristic. These parameters play an important role to identify the S-shape J-V characteristics and will be investigated in detail. In analogy to diodes the definition for the threshold voltage for extraction V_{th_e} and the threshold voltage for injection V_{th_i} are introduced. These voltages have to be provided in order to extract or inject a significant part of charge carriers, respectively. V_{th_e} and V_{th_i} are

marked in Figure 5-8. For the S-shape J-V characteristics 3 regions can be distinguished, depending on the size of the externally applied voltage:

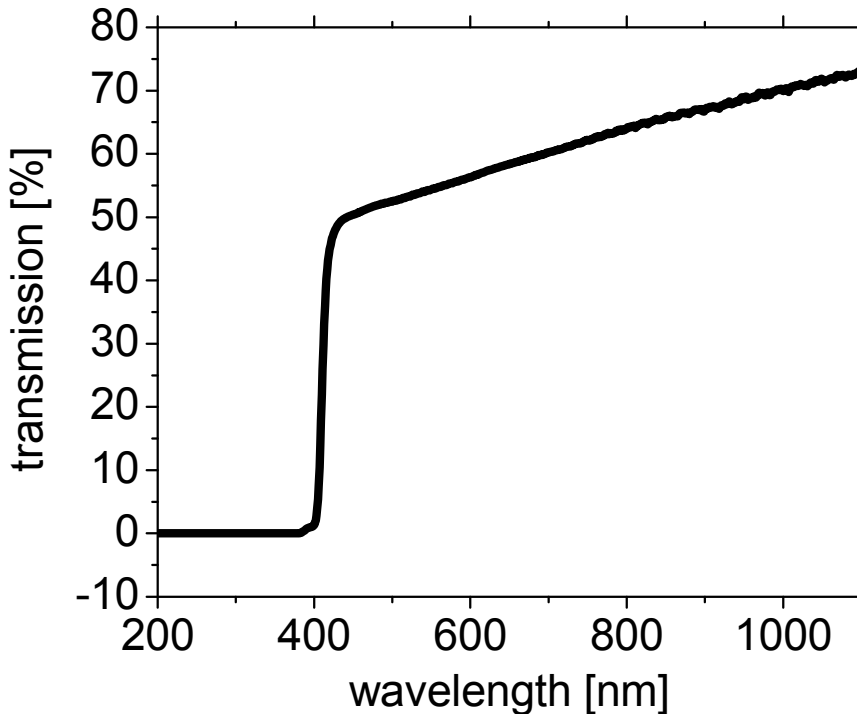


Figure 5-9: Transmission of the UV-filter foil used for VIS irradiation of the OPV cell.

$V < V_{th_e}$: The photo-generated carriers are extracted. For a sufficiently low voltage V , the current density with and without S-shape are equal. The difference in current density for low voltages shown in Figure 5-8 is due to absorption losses by the UV-filter foil.

$V_{th_e} < V < V_{th_i}$: For this regime the current density is close to 0.

$V_{th_i} < V$: The solar cell operates in injection mode. Carriers are injected into the solar cell.

For an OPV cell with UV irradiation the regime 2 ($V_{th_e} < V < V_{th_i}$) disappears, i.e.

$V_{th_e} = V_{th_i} = V_{oc}$. It must be noted that the slope in region (1) and (3) can vary depending if the OPV cell is illuminated by UV-VIS radiation or not.

The extent of S-shape formation is defined as the difference between V_{th_e} and V_{th_i} . It strongly depends on the processing and the kind of TiO_x which is formed during processing. Especially in a sol-gel process the hydrolysis of TiO_x is difficult to control and strongly depends on e.g. relative humidity and temperature control. Kuwabara et al. found that the

strength of the S-shape characteristics depends on the crystallinity of the TiO_x .¹⁰¹ As such, the effect of the S-shape characteristics is investigated qualitatively.

5.2.2 Behavior of Organic Photovoltaic Cells under UV-VIS Irradiation

In the following, the origin of the S-shape J-V characteristic as well as the removal of the S-shape J-V characteristic by UV-VIS irradiation are investigated. The time dependence of the device parameters with and without UV-VIS irradiation are investigated by recording a J-V curve every 30 seconds under a solar simulator. First, the device is covered with a UV filter foil and the performance followed for 15 min. In a second step the UV-filter foil is removed and the OPV cell is irradiated with UV-VIS irradiation and measured again repeatedly. Next the OPV cell is covered again by the UV-filter foil and the device parameters are measured over another 30 min time of VIS illumination only. Figure 5-10 illustrates the OPV cell parameters FF, J_{sc} , PCE, V_{oc} and the injection current at +1V with and without UV irradiation.

The device performance is slightly affected during 13 min of VIS illumination. The injection current at +1 V is very low (in the range of 3 mA/cm^2) and the FF of the device is only 40 % which is a typical poor value for the S-shape J-V characteristic with no UV irradiation. With UV-VIS irradiation the injection current at +1 V increases immediately and saturates after 10 min at a value of 80 mA/cm^2 concomitant with an increase in FF to 56 %. The increase in current density from 6.2 mA/cm^2 to 8.4 mA/cm^2 is explained by the absorption of the used UV-filter in the VIS spectrum. Upon reinserting the UV-filter into the light path, the injection current at +1 V decrease slowly over time. The FF decreases with a delay of several minutes. The sudden decrease in J_{sc} is due to the reduced light intensity reaching the device, mainly due to significant absorption of VIS light by the UV-filter foil. The slow decrease in J_{sc} over time is related to a slight degradation which is typically observed when measurements are performed in air. V_{oc} is slightly affected over the entire experiment. For the S-shape J-V characteristics, a low shunt resistance can result in reduced V_{oc} since the current density close to V_{oc} is small compared to the current density through the shunt. The observations can be summarized as follows:

- (a) VIS illumination does not change the S-shape J-V characteristics. The injection current remains low and the effect on FF is only small.

(b) UV-VIS irradiation improves device performance and the S-shape J-V characteristic vanishes. Both injection current and FF rise promptly and saturate after a few minutes.

(c) VIS illumination of a device without S-shape causes a slow reduction of the injection current with time. The FF remains constant over several minutes until it decreases.

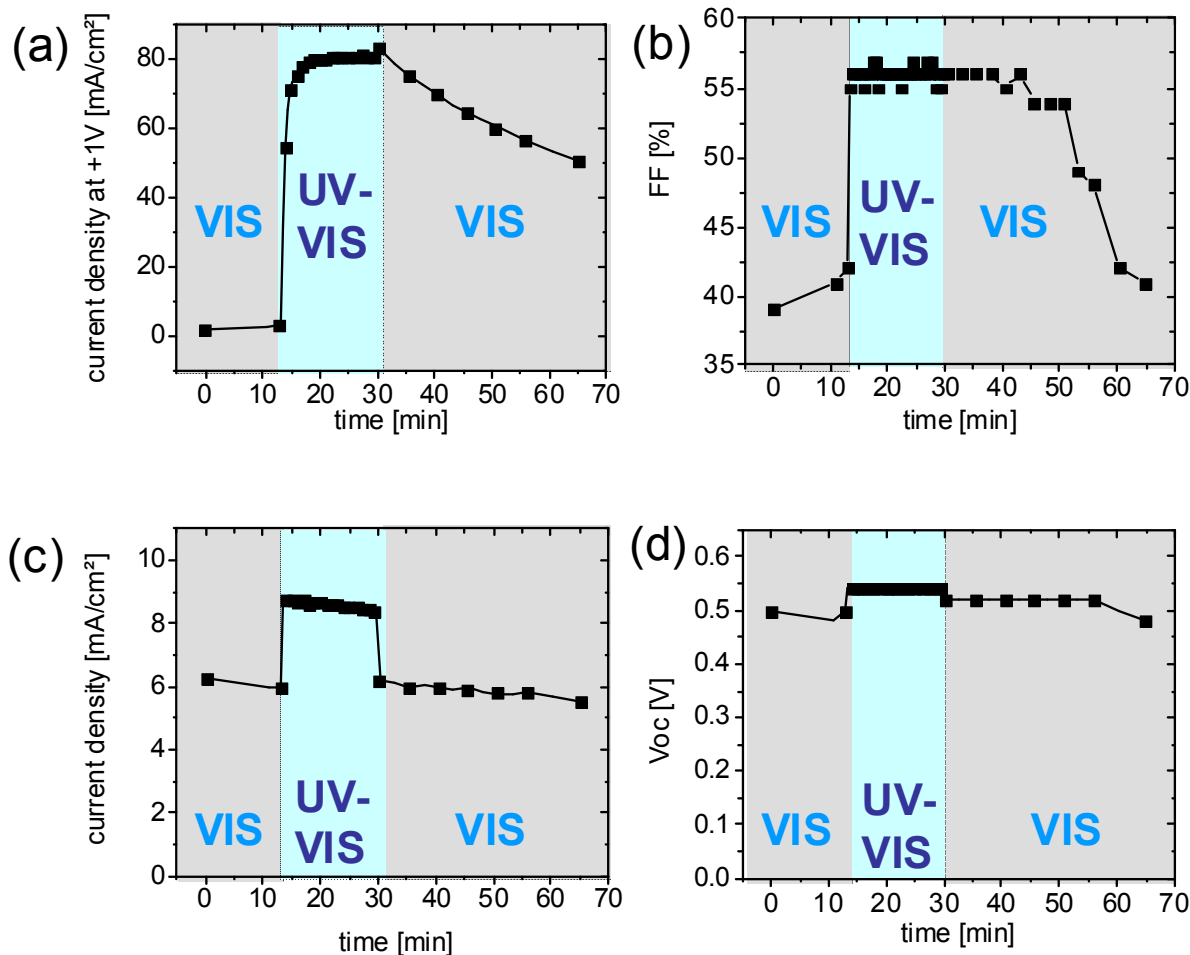


Figure 5-10: Time dependence of the injection current density at +1 V (a), FF (b), J_{sc} (c) and V_{oc} (d) as a function of time of VIS and UV-VIS irradiation.

From these findings, UV irradiation is required for efficient OPV devices in the investigated device configuration. TiO_x has a bandgap of 3.1 eV⁴⁶ and thus absorbs light with energies above 3.1 eV or a wavelength below 400 nm. In contrast to TiO_x the semiconductor and

PEDOT:PSS do absorb light also in the VIS. Therefore, it is most likely that UV radiation changes the properties of the TiO_x interfacial layer.

The conductivity of sol-gel processed TiO_x is measured with and without UV-VIS irradiation by an interdigitated contact structure presented in chapter 2.5.2. Figure 5-11 illustrates results on conductivity measurements under different investigated conditions namely UV-VIS irradiation, VIS irradiation and no irradiation (dark). Measurement points are recorded every 22 s by applying a voltage of 10 V and measuring the current transported by the TiO_x . In order to eliminate the impact of heat under different illumination conditions the sample is placed on a hotplate at 100°C. In a first step, the TiO_x coated substrate is placed under the solar simulator and illuminated with UV-VIS irradiation. In a second step, a UV-filter foil is placed over the sample to eliminate the UV part of the spectrum of the solar simulator. This sequence is repeated. Once the sample reaches its maximum again, the sample is covered with a black cardboard and the conductivity measured as a function of time in the dark.

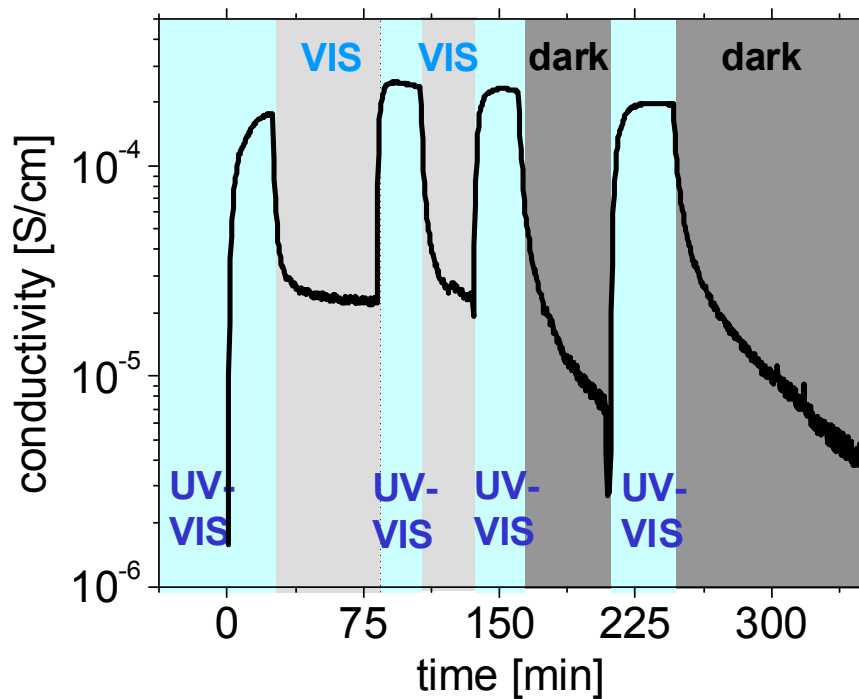


Figure 5-11: Conductivity of sol-gel processed TiO_x with UV-VIS and VIS irradiation as well as in the dark as a function of time.

The conductivity of TiO_x measured in the dark is $2 \mu\text{S}/\text{cm}$. This value is the lowest value measurable with the measurement setup. Upon UV-VIS irradiation the conductivity of TiO_x rises immediately by more than 2 orders of magnitude compared to the conductivity without UV-VIS irradiation and saturates within minutes. When covering the TiO_x by a UV filter foil, the conductivity decreases immediately and levels out at approximately one order of magnitude lower values. This behaviour is reproducible. Without illumination the conductivity of TiO_x drops from the conductivity reached by UV-VIS irradiation to values below VIS irradiation, approaching starting values of $2 \mu\text{S}/\text{cm}$.

In summary it is found that the conductivity of the investigated TiO_x layer increases up to 2 orders of magnitude with UV-VIS irradiation. Covering the TiO_x with a UV filter foil, the conductivity reached by UV-VIS irradiation decreases, but does not reach the initial value in the dark. After extended storage in the dark, the conductivity reaches the initial value. The increase in conductivity with time under UV-VIS irradiation from the initial value in the dark is faster than the decrease of the conductivity in the dark to its initial values. These findings are in agreement with several other studies dealing with the properties of TiO_2 .¹⁹⁴

The changes of conductivity of TiO_x under irradiation with UV light correlate very well with the changes in device performance under the same conditions. A fast increase in device performance correlates with a fast increase in the conductivity of the TiO_x . Once the sample has reached high conductivity, the device performance is stable for some minutes under VIS illumination. The loss in conductivity and device performance is slower than the fast initial increase in conductivity. A loss in conductivity of TiO_x has been indentified as a reason which is causing S-shape J-V characteristics in OPV cells.

5.2.3 Simulation of the S-shape Current-Voltage Characteristic

In this section experimental results are combined with simulations to get a deeper understanding of the S-shape J-V characteristic. The J-V characteristic is simulated with PC1D²⁴, a 1 dimensional simulation program developed for inorganic semiconductor physics. A model structure is applied which allows the simulation of experimental J-V characteristics and discussion of the origin of the S-shape J-V characteristic on a device level.

The donor:acceptor bulk-heterojunction of the OPV cell is simulated by 1 semiconducting layer which we name in the following polymer blend. The valence band of the polymer blend

is determined by E_{ICT+} of the donor polymer, i.e. P3HT. The conduction band is determined by E_{ICT-} of the acceptor, i.e. PCBM. This model assumes that charge separation and generation are uniform throughout the entire bulk-heterojunction.¹⁹ The solar cell is irradiated with a light intensity of 100 mW/cm² by the AM1.5G spectrum of the sun. The active area of the solar cell is set as such that the simulated short-circuit current matches the experimental received one. In chapter 5.2.2 it is discussed that the S-shape J-V characteristic can be eliminated through increasing the conductivity of TiO_x. For simulations of OPV devices with and without S-shape a two semiconductor layer model is applied. This two layer semiconductor model consists of the polymer blend P3HT:PCBM and the wide band gap semiconductor TiO_x. Other layers, e.g. PEDOT:PSS are neglected in this model to concentrate on the relevant materials and effects. Figure 5-12 illustrates the OPV cell model with conduction band, valence band, electron and hole quasi Fermi levels for the investigated configuration under V_{oc} conditions.

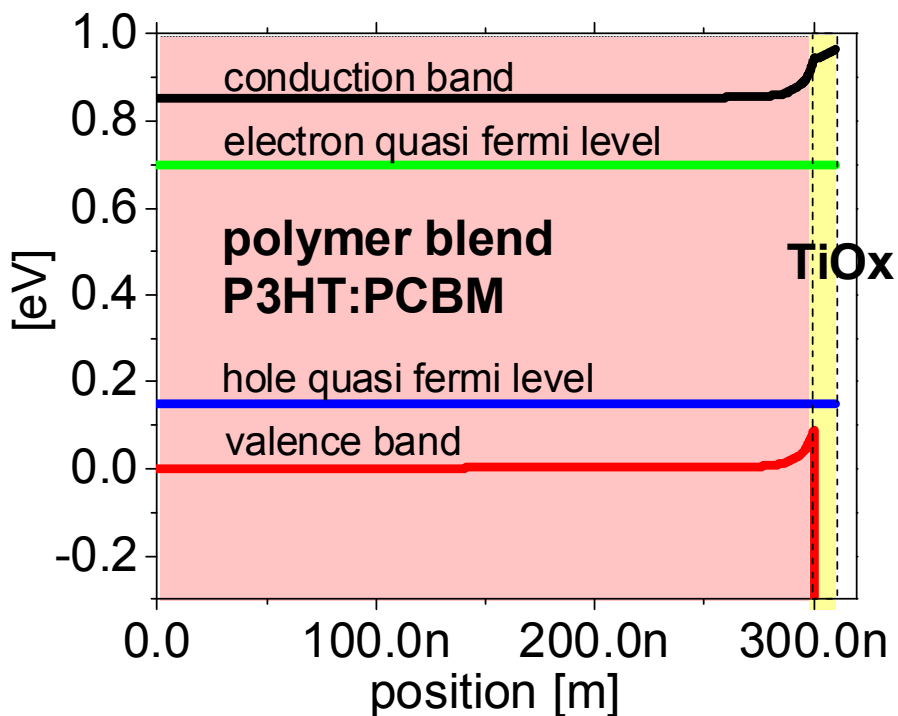


Figure 5-12: Graph of the device structure of the investigated device model. It consists of the polymer blend P3HT:PCBM and the wide band gap semiconductor TiO_x. The band structure with the conduction band, valence band, electron and hole quasi Fermi level at V_{oc} conditions is included in the graph.

The contact of the polymer blend and the TiO_x semiconductors is defined by the electron affinity. The electron affinity is set to the same value of 3.7 eV for both semiconductors. Table 3 summarizes the relevant parameters for the J-V simulations with PC1D.

The polymer blend is slightly p-doped and the band gap is set to 0.85 eV. The carrier lifetime is set to 5 μs . TiO_x is set as n-doped semiconductor with a band gap of 1.3 eV.

Table 3: List of relevant parameters for the simulation performed with PC1D.

	polymer blend P3HT:PCBM	interfacial layer TiO_x
layer thickness	300 nm	10 nm
electron affinity	3.7 eV	3.7 eV
band gap	0.85 eV	1.3 eV
electron mobility μ_e	$3 \times 10^{-3} \text{ cm}^2/\text{Vs}$	free parameter
hole mobility μ_h	$6.5 \times 10^{-4} \text{ cm}^2/\text{Vs}$	$6 \times 10^{-4} \text{ cm}^2/\text{Vs}$
intrinsic concentration	10^{12} cm^{-3}	10^8 cm^{-3}
background doping	10^{15} cm^{-3}	free parameter
R_s	8.5 ohm	-
R_p of semiconductor	1000 ohm	-

This value for the bandgap of TiO_x is lower than the literature values of ~ 3.1 eV. However, the simulation is unstable and does not converge for a band gap greater than 1.3 eV. The wide band gap semiconductor still acts as electron transport layer since the band gap of the polymer blend and TiO_x show a difference of 0.45 eV which is assumed to be sufficient for studying the S-shape J-V effect. The values for the electron and hole mobilities of the polymer blend are determined by fitting the measured J-V characteristics with the simulated ones. The electron and hole mobilities are kept constant over the semiconductor layer for 1 sun illumination. It has been presented above that TiO_x changes its conductivity, i.e. the product of carrier density and mobility, upon UV-light irradiation. The simulation of J-V

curves with and without S-shape characteristics is thus performed by varying either the charge carrier mobility or the doping level of the TiO_x layer.

Figure 5-13 presents the measured J-V-curves with and without UV irradiation. The first measurement without UV radiation is performed with a UV-filter foil. The sample is then illuminated for 20 min with UV-VIS radiation, covered with a UV-filter foil and measured again. No S-shape is observed for several minutes after such a UV-VIS treatment. With this measurement method similar J_{sc} values for the J-V characteristic with and without S-shape are obtained. The measured J-V curves are shown in Figure 5-13 together with the simulated J-V curves with and without S-shape.

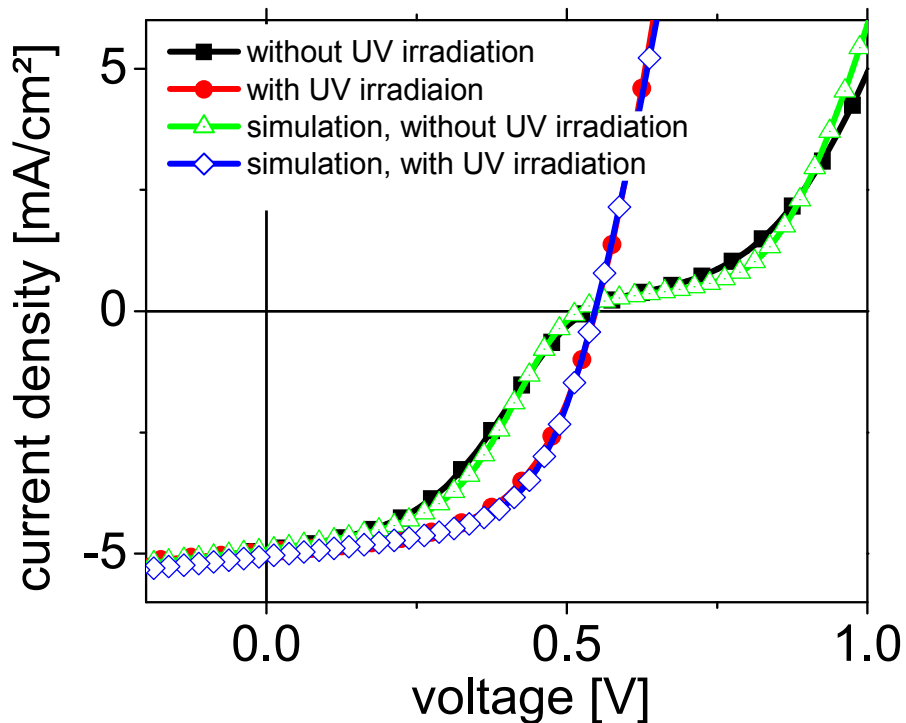


Figure 5-13: The simulated (open symbols) together with the measured (full symbols) J-V curves with and without S-shape J-V characteristics are presented. The experimental processed OPV cells are in the device structure ITO/ TiO_x /P3HT:PCBM/PEDOT:PSS/Ag. The impact of UV irradiation is simulated by the change in the doping of the TiO_x layer from $5 \times 10^{14} \text{ cm}^{-3}$ to $5 \times 10^{17} \text{ cm}^{-3}$.

The electron mobility and doping of TiO_x is set to $8 \times 10^{-5} \text{ cm}^2/\text{Vs}$ and $5 \times 10^{14} \text{ cm}^{-3}$, respectively to simulate the S-shape J-V characteristics. All other relevant parameters are listed in Table 3. A change of the doping of the TiO_x layer from $5 \times 10^{14} \text{ cm}^{-3}$ to $5 \times 10^{17} \text{ cm}^{-3}$

causes the S-shape to disappear. The same behavior is observed when the mobility is changed from $8 \times 10^{-5} \text{ cm}^2/\text{Vs}$ to $8 \times 10^{-2} \text{ cm}^2/\text{Vs}$. The J-V curves with and without S-shape J-V characteristics can be simulated by increasing the mobility or the doping of the TiO_x layer by 3 orders of magnitude as the only parameter. To further verify the model and gain a deeper understanding on the origin of the S-shape J-V characteristics a more pronounced S-shape J-V characteristics is simulated. The J-V characteristics with and without S-shape are measured with an UV-filter foil. Due to the optical absorption of the UV-filter foil J_{sc} is different. Results are presented in Figure 5-14.

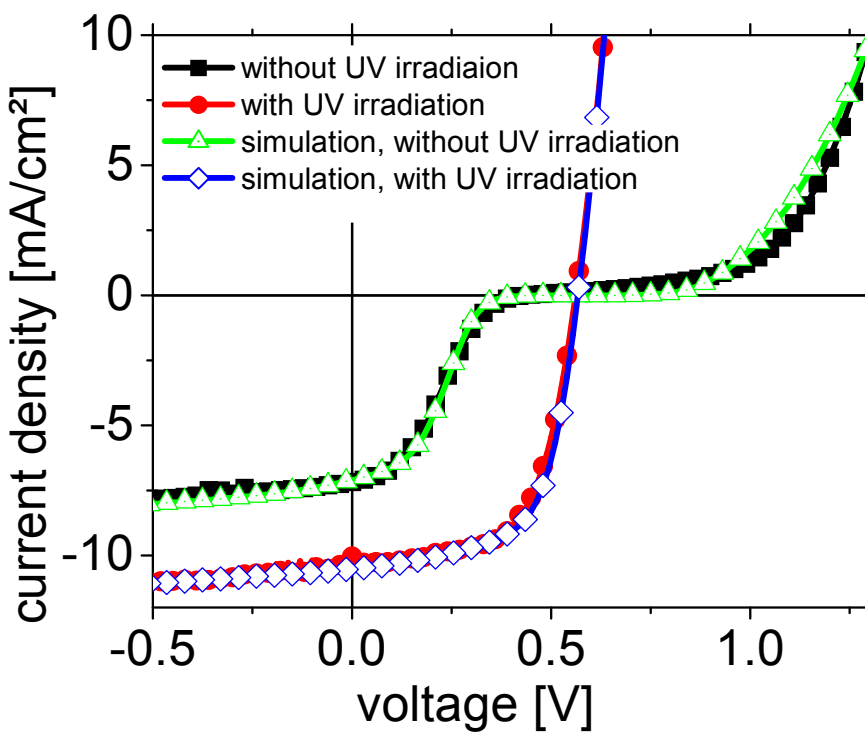


Figure 5-14: The simulated (open symbols) together with the measured (closed symbols) J-V curves with and without S-shape J-V characteristics are presented. The experimental processed OPV cells are in the device structure ITO/ TiO_x /P3HT:PCBM/PEDOT:PSS/Ag with slightly modified processing of the TiO_x layer compared to the presented J-V characteristics in Figure 5-13. The impact of UV irradiation is simulated by the change in the doping of the TiO_x layer by 6 orders of magnitude.

The parameters of the polymer blend are slightly modified compared to the less pronounced S-shape but are set to constant values for the simulation of the J-V characteristic with and without S-shape J-V characteristics. The changing of the doping or mobility of TiO_x by 6

orders of magnitude allows switching between S-shape and no S-shape. These results suggest that a more pronounced S-shape J-V characteristic is related to a lower conductivity of the TiO_x layer. The conductivity of sol-gel processed TiO_x is reported to be sensitive to e.g. the doping, the atmosphere and the adsorbed water on the TiO_x layer.¹⁹⁴ The S-shape J-V characteristic is also suggested to depend on whether amorphous or anatase TiO_x is formed.¹⁰¹ Therefore these results do not contradict our observations since for a sol-gel process the hydrolysis of TiO_x is difficult to control.

In the following the origin of the S-shape is investigated by simulating the band structure and the distribution of the electrical field within the device.

4 working points are chosen to study the band structure and the electrical field of an OPV cell with and without S-shape J-V characteristics in detail. The 4 positions are marked in Figure 5-15.

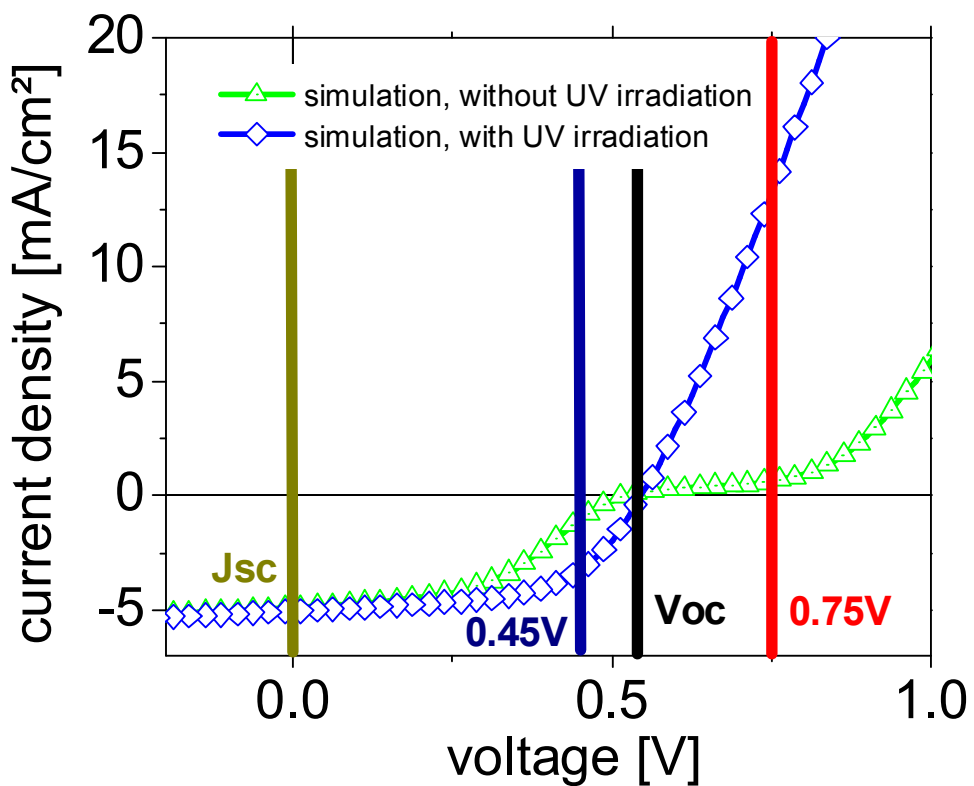


Figure 5-15: Simulated J-V characteristics of an OPV cell with and without S-shape. At J_{sc} and V_{oc} the current densities for a S-shape and non S-shape J-V characteristic are same. At biases of 0.45 V and 0.75 V the current densities for the J-V characteristics with and without S-shape are different.

The investigated voltages describe the following situations:

- **V_{oc} :** No charge is extracted or injected to or from the outer circuit. The current densities for the J-V curves with and without S-shape are equal.
- **J_{sc} :** All photo-generated carriers are extracted to the outer-circuit. The current densities for the J-V curves with and without S-shape are equal.
- **0.45 V:** The OPV cell generates charge carriers which are extracted to the outer circuit. For the S-shape J-V characteristic the extraction current density is as low as 1 mA/cm^2 while compared to 3.2 mA/cm^2 for the J-V characteristics without S-shape.
- **0.75 V:** The OPV cell operates in injection mode. Charge carriers are injected from the outer circuit into the OPV cell. The current density for the S-shape characteristic is clearly limited to 0.6 mA/cm^2 while the OPV cell without S-shape has a current density of 13.2 mA/cm^2 .

It has been shown above that the S-shape J-V characteristic vanishes when the conductivity of the TiO_x layer is increased by 3 orders of magnitude, i.e. either by an increase of the doping of TiO_x from $5 \times 10^{14} \text{ cm}^{-3}$ to $5 \times 10^{17} \text{ cm}^{-3}$ or increase the mobility of TiO_x from $8 \times 10^{-5} \text{ cm}^2/\text{Vs}$ to $8 \times 10^{-2} \text{ cm}^2/\text{Vs}$. To understand this behaviour the band structure and electric field distribution for the points V_{oc} , 0.75 V, 0.45 V and J_{sc} are shown with and without S-shape J-V characteristics (increased doping or mobility case).

The simulated graph of the band structure includes the conduction band, the valence band, electron and hole quasi Fermi levels. The contact of the two semiconductors is determined by their common electron affinity. Thus, the band structure at the interface is determined in dependence of the doping level because the Fermi levels have to be identical for the TiO_x layer and the polymer blend. With increasing doping concentration, the energy difference between the conduction band and the quasi Fermi level for electrons decreases. Therefore, the doping of the TiO_x is clearly visible in the band structure comparing Figure 5-16 (a) and (b).

- (**V_{oc} condition, Figure 5-16**): For the V_{oc} case, the derivative of the electron and hole quasi Fermi levels are zero over the whole device, therefore no carriers are extracted to the electrodes or injected from the electrodes. The solar cell operates under flat band conditions. The conduction band and valence band show a gradient at the interface $\text{TiO}_x/\text{polymer blend}$ which depends on the doping level of the TiO_x . The sum of drift and diffusion is zero.

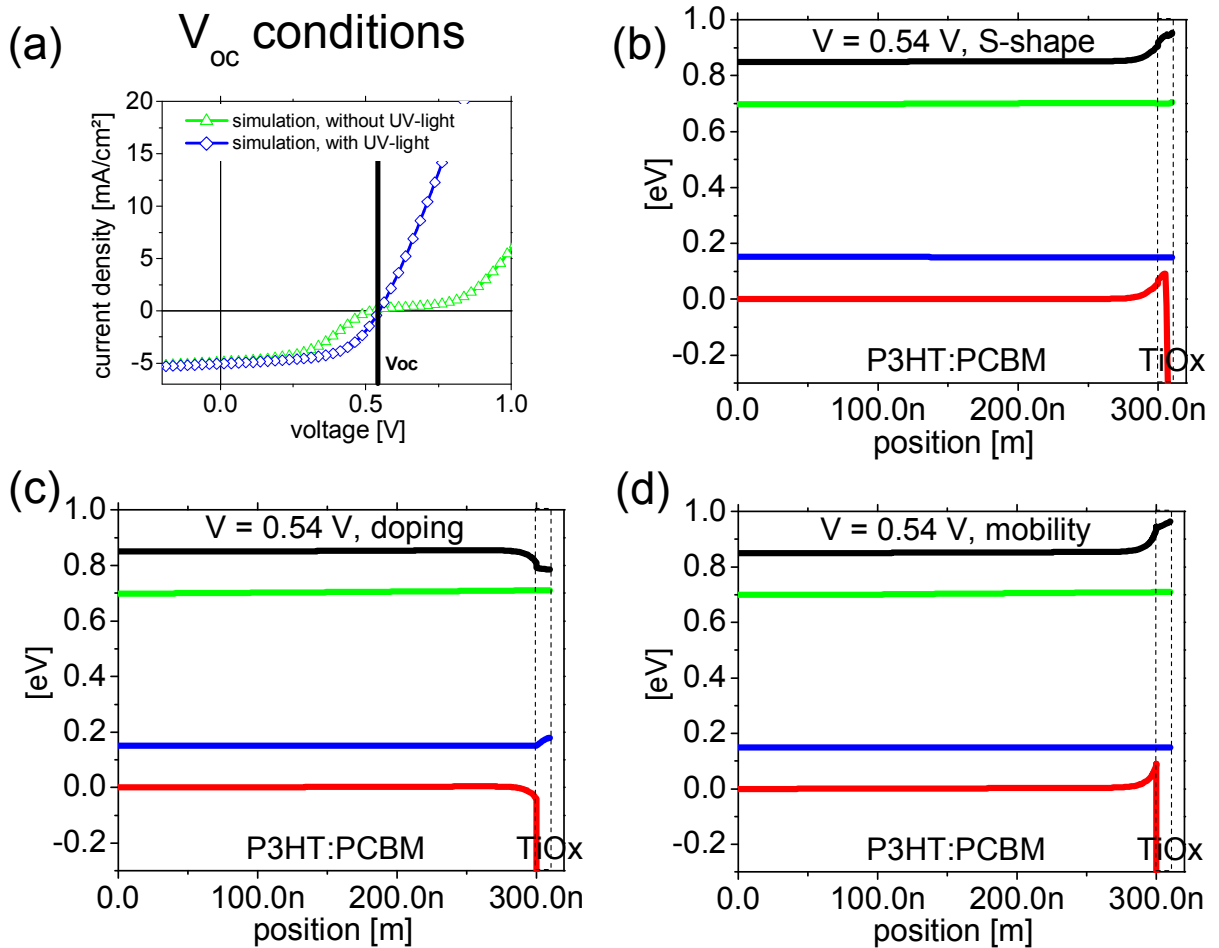


Figure 5-16: (a) presents the simulated J-V characteristics with and without S-Shape. The graph of the band structure at 0.55 V is illustrated for the J-V characteristics with (b) and without (c, d) S-shape. In (b) the TiO_x layer has low conductivity and mobility. In (c) the doping of the TiO_x layer is increased. In (d) the mobility of the TiO_x layer is increased. The black line represents the conduction band. The red line represents the valence band. The green line represents the quasi Fermi level for electrons. The blue line represents the quasi Fermi level for holes.

- (**J_{sc} conditions, Figure 5-17**): The effective voltage V_{effective} (V_{bi} - V) drops within the OPV device. Both, for J-V characteristics with and without S-Shape, the same amounts of photo-generated carriers are extracted to the electrodes. The derivative of the quasi Fermi levels as well as the one of the conduction and valence band is high enough to extract all photo-generated carriers.

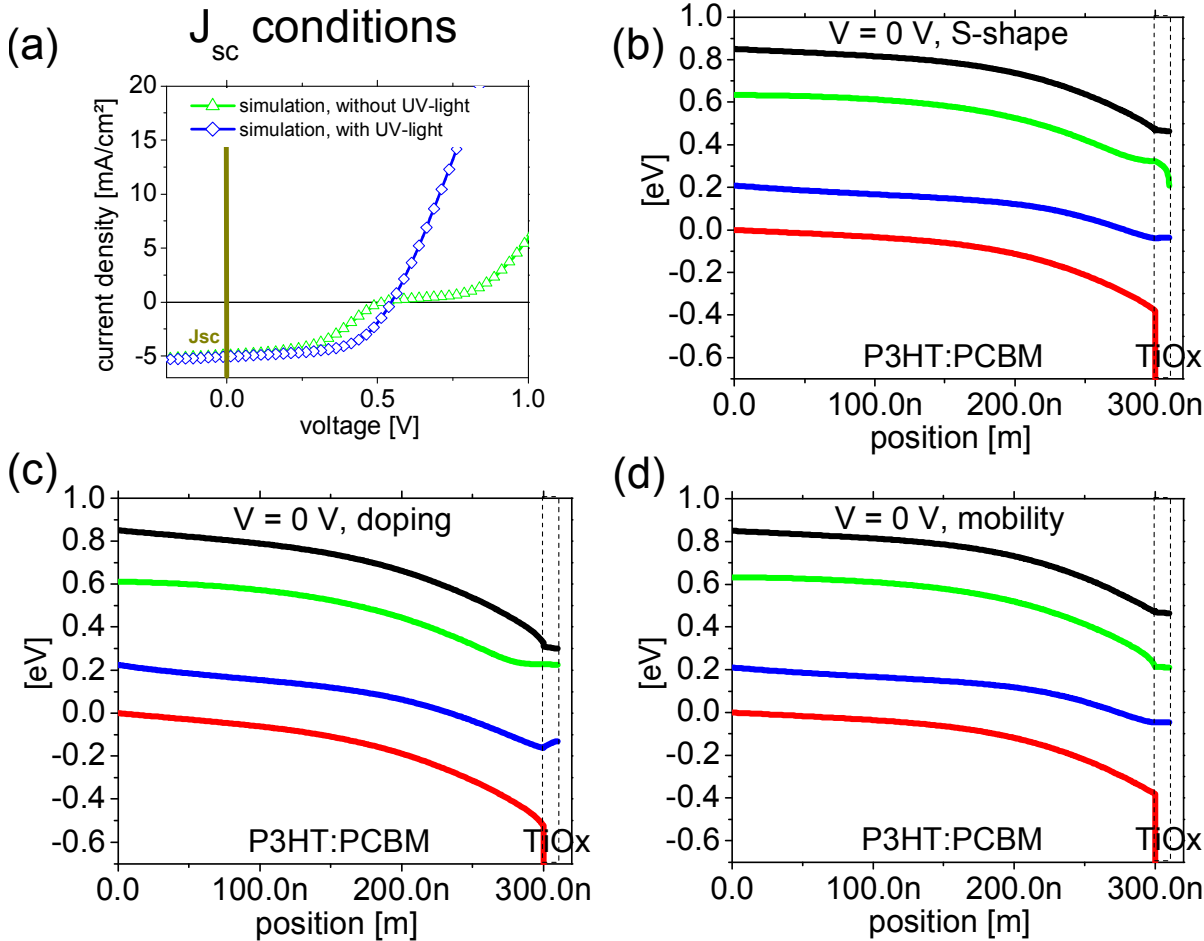


Figure 5-17: (a) presents the simulated J-V characteristics with and without S-Shape. The graph of the band structure at 0 V is illustrated for the J-V characteristics with (b) and without (c, d) S-shape. In (b) the TiO_x layer has low conductivity and mobility. In (c) the doping of the TiO_x layer is increased. In (d) the mobility of the TiO_x layer is increased. The black line represents the conduction band. The red line represents the valence band. The green line represents the quasi Fermi level for electrons. The blue line represents the quasi Fermi level for holes.

- Extraction ($V = 0.45$ V), Figure 5-18: For the S-shape J-V characteristics less current is extracted to the outer circuit comparing the current density with and without S-shape. For the case of the S-shape J-V characteristics, the quasi Fermi level for electrons is almost flat within the polymer blend and shows a gradient only within the TiO_x layer. For doped TiO_x or a TiO_x layer with high mobility the situation is different: The quasi Fermi level for electrons

shows a gradient over almost the entire polymer blend layer. This results in a higher extraction current.

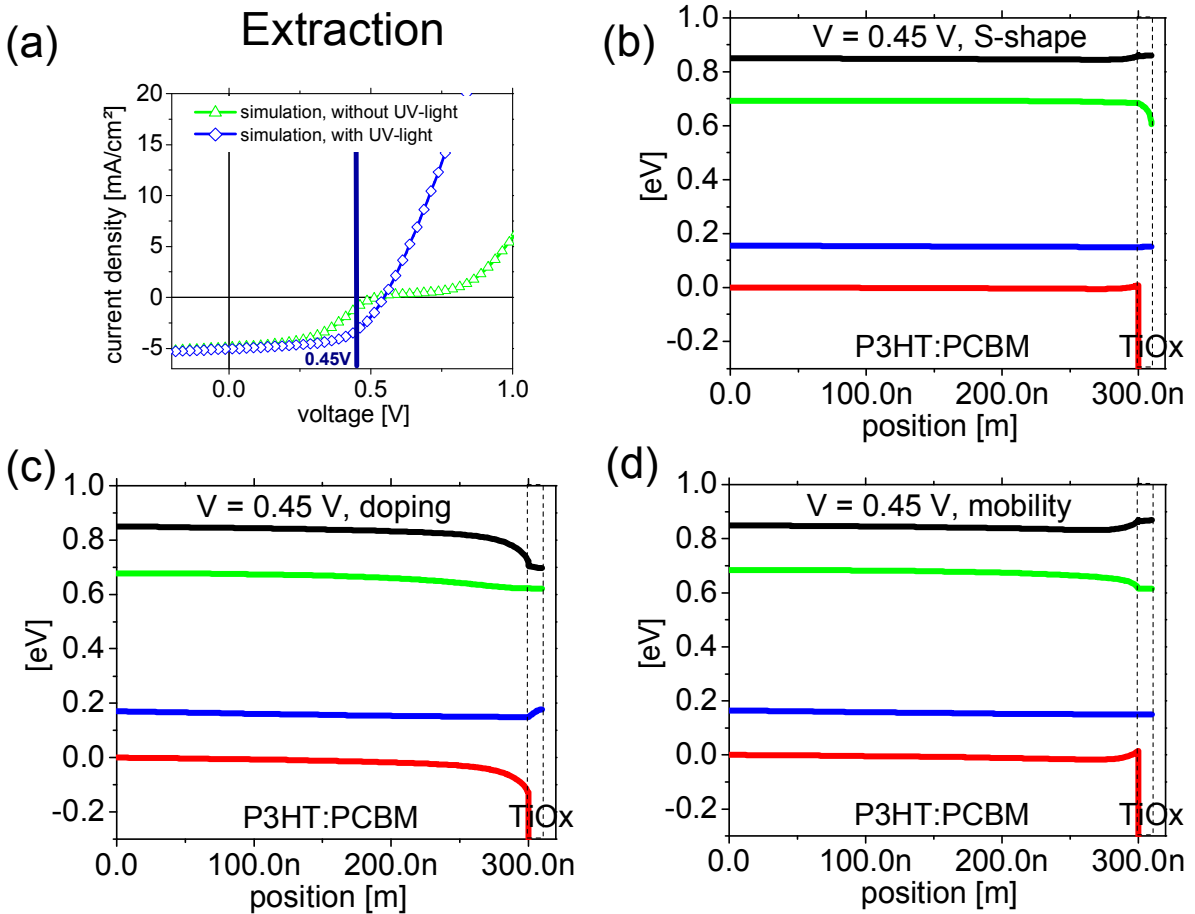


Figure 5-18: (a) presents the simulated J-V characteristics with and without S-Shape. The graph of the band structure at 0.45 V is illustrated for the J-V characteristics with (b) and without (c, d) S-shape. In (b) the TiO_x layer has low conductivity and mobility. In (c) the doping of the TiO_x layer is increased. In (d) the mobility of the TiO_x layer is increased. The black line represents the conduction band. The red line represents the valence band. The green line represents the quasi Fermi level for electrons. The blue line represents the quasi Fermi level for holes.

- Injection ($V = 0.75$ V), Figure 5-19: At 0.75 V the device operates in injection mode where electrons are injected from the electrode over the TiO_x layer. For the the S-shape case the conduction band and the quasi Fermi level for electrons drop solely over the TiO_x and at the interface between polymer blend and TiO_x, respectively. Within the polymer blend the

quasi Fermi levels as well as the conduction and valence band are flat. For the non S-shape J-V characteristics the bands are not flat within the polymer blend: The gradient is distributed equally over the polymer blend leading to an electron current flow from the TiO_x into the active layer of the device.

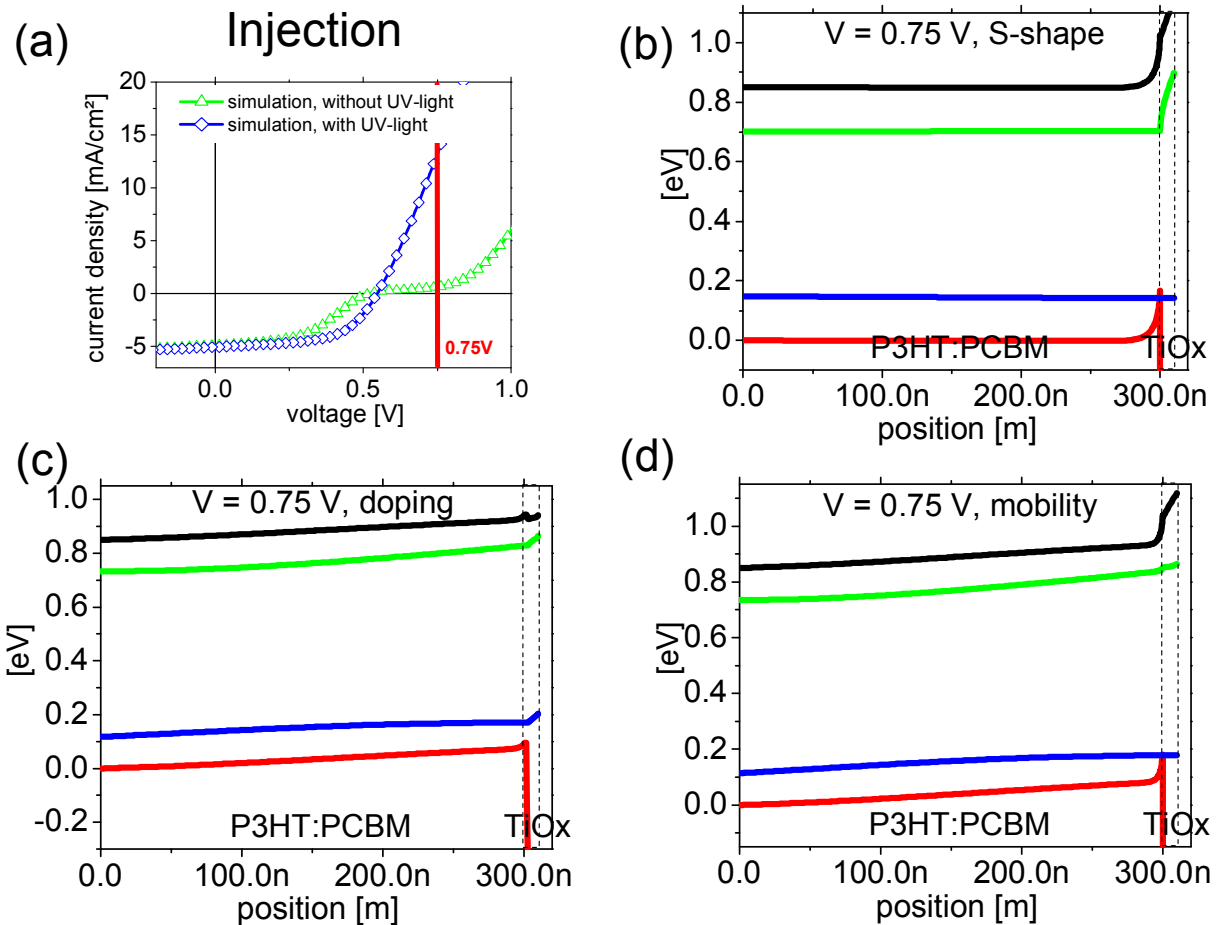


Figure 5-19: (a) presents the simulated J-V characteristics with and without S-Shape. The graph of the band structure at 0.75 V is illustrated for the J-V characteristics with (b) and without (c, d) S-shape. In (b) the TiO_x layer has low conductivity and mobility. In (c) the doping of the TiO_x layer is increased. In (d) the mobility of the TiO_x layer is increased. The black line represents the conduction band. The red line represents the valence band. The green line represents the quasi Fermi level for electrons. The blue line represents the quasi Fermi level for holes.

In conclusion the band structures within the OPV cell for the S-shape and the non S-shape J-V characteristics are investigated. For the S-shape J-V characteristics a small or no gradient

of the quasi Fermi levels is found for the voltages 0.45 V, V_{oc} and 0.75 V. The same is true for the conduction and valence bands within the polymer blend. The band structure is flat within the polymer blend for this voltage range. The band structure shows mainly a gradient over the TiO_x and near the interface between the polymer blend layer and TiO_x layer. For devices without S-shape J-V characteristics, i.e. TiO_x with higher mobility or doping levels, the quasi Fermi levels as well as the conduction band and valence band exhibit a gradient throughout the device.

The drop of the electric field within the polymer blend and within TiO_x is investigated for simulated J-V characteristics with and without S-shape. Figure 5-20 illustrates the electric field distribution within the OPV cell in the relevant voltage regime in direct comparison of the S-shape and non S-shape J-V characteristics.

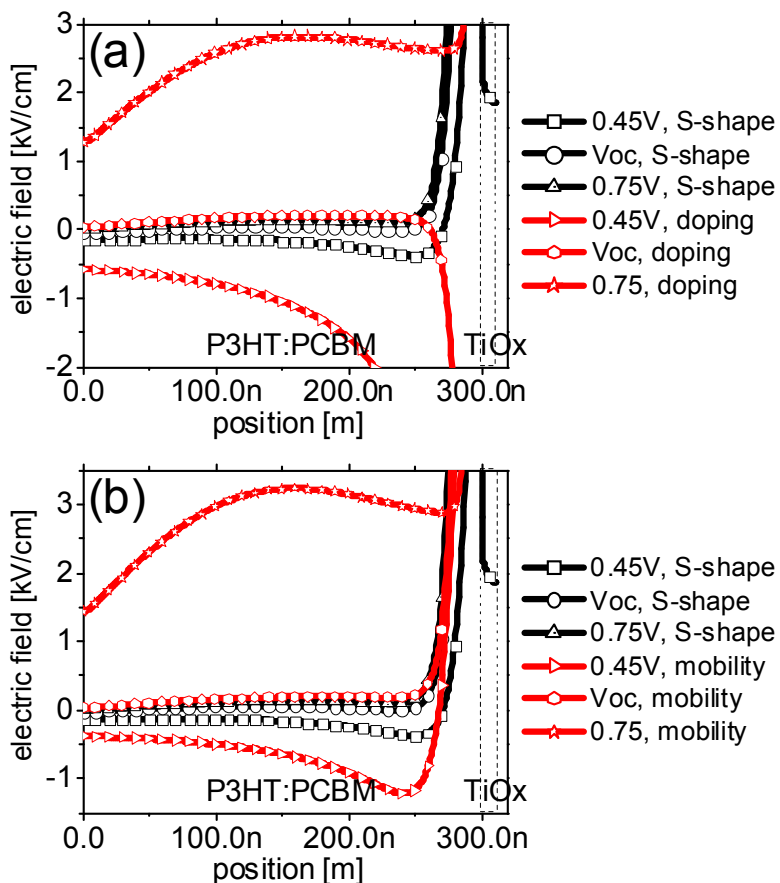


Figure 5-20: Simulated electric field distribution within the polymer blend and the TiO_x layer. The black lines illustrate the electric field within the OPV cell for the S-shape J-V characteristic. The red lines illustrate the electric field distribution within the OPV cell without S-shape J-V characteristics for a TiO_x layer with higher doping (a) and higher mobility (b) compared to the properties of the TiO_x layer resulting in the S-Shape J-V characteristics.

At V_{oc} conditions, no current is extracted to the outer electrodes. The drop of the electric field within the polymer blend is small for all investigated cases. For the S-shape characteristics the drop in the electric field at 0.45 V and 0.75 V is small in the middle of the polymer blend. The electric field drops at the interface polymer blend/TiO_x and within the TiO_x layer. The electric field distribution at 0.45 V and 0.75 V is comparable to the one at V_{oc} conditions. As such the extracted current is very little and an S-shape in the J-V characteristic appears. For the non S-shape J-V characteristics the electric field is much higher in the polymer blend at 0.45 V and 0.75 V, e.g. 3 kV/cm compared to 0.12 kV/cm for the S-shape J-V characteristics at 0.75 V.

At J_{sc} all photo-generated charge carriers are extracted to the electrodes for the J-V characteristics with and without S-shape. Consequently, the electric field within the device has to be sufficiently high to transport the charge carriers to their respective electrodes. Figure 5-21 illustrates the electric field distribution within the device for J-V characteristics with and without S-shape.

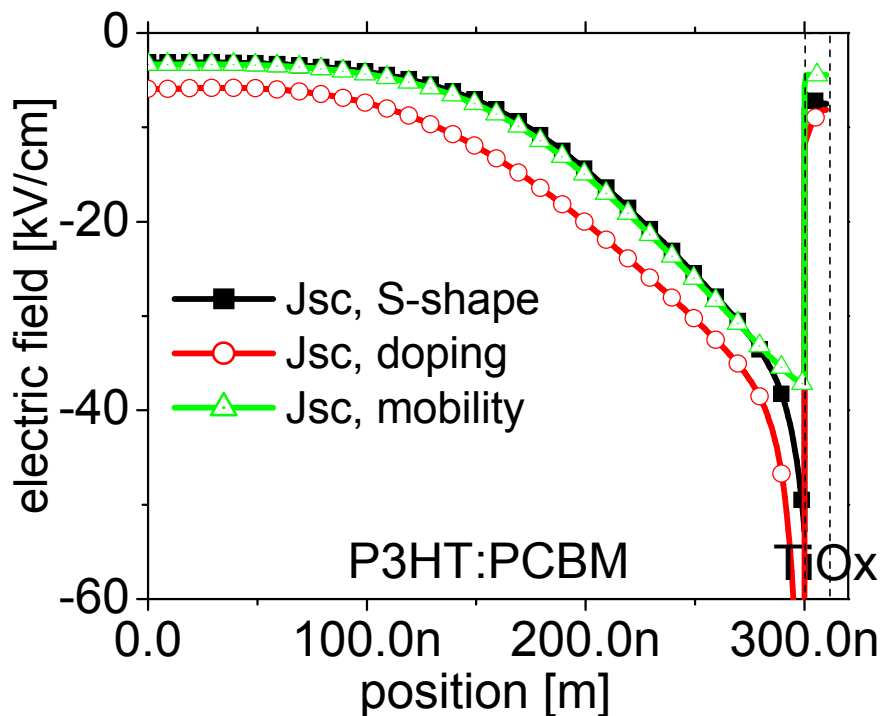


Figure 5-21: Simulated electric field distribution within the polymer blend and the TiO_x layer at J_{sc} conditions.

Throughout the device the electric field is higher than 3 kV/cm which is sufficient to extract all charge carriers to the corresponding electrodes as discussed above.

In summary, simulations of a model device consisting of a polymer blend and TiO_x interlayer allow the simulation of devices with and without S-shape J-V characteristics. Keeping all device parameters constant, an S-shape J-V characteristic can be simulated by decreasing the conductivity of TiO_x . For the S-shape J-V characteristics the drop of the electric field is very small within the polymer blend for the voltage range $V_{\text{th_e}}$ to $V_{\text{th_i}}$ and comparable to V_{oc} conditions. The electric field drops mainly in the TiO_x layer and near the interface polymer blend/ TiO_x . Charge carriers are generated in the polymer blend but not transported to the electrodes in the extraction mode. In the injection mode, charge carriers which are injected into the polymer blend are not transported through the polymer blend. For voltages lower $V_{\text{th_e}}$ or higher $V_{\text{th_i}}$ for the S-shape J-V characteristics as well as for the non S-shape J-V characteristic the electric field within the polymer blend is significantly higher.

The non-uniform electric field over the OPV device, i.e. the drop of the electric field mainly in and near the interfacial layer, is the main reason for the occurrence of the S-shape J-V characteristics.

5.2.4 Experimental Simulation of the S-shape Current-Voltage Characteristic

It is shown in chapter 5.2.3 that the occurrence of an S-shape J-V characteristic is related to a reduced mobility or doping of the interfacial layer. To further strengthen this theoretical finding, the conductivity of the interfacial layer of a device which shows no S-shape J-V characteristic is experimentally decreased. To this end, TiO_x is replaced with a novel hole blocking layer (HBL) which results in comparable device parameters. The major advantage of utilizing this material is that it does not exhibit S-shape J-V characteristics in the absence of UV radiation. This is highly favourable when the factors leading to an S-shape are studied experimentally. The interface is modified with a thin layer of SiO_x at different positions at the cathode side of the OPV cell. SiO_x is chosen because it is regarded as an inert material which decreases the conductivity at the interface. SiO_x is inserted through thermal evaporation of SiO_2 at different positions of the device, namely (ITO/ SiO_x /HBL/P3HT:PCBM/PEDOT:PSS/Ag), (ITO/HBL/ SiO_x /P3HT:PCBM/PEDOT:PSS/Ag) and

(ITO/SiO_x/P3HT:PCBM/PEDOT:PSS/Ag). For each variation a layer thickness of SiO_x of 0.5 nm, 1 nm, 2 nm and 3 nm is investigated. It must be noted that the thicknesses do not represent accurate values. The thickness is estimated from the change in frequency of the quartz crystal microbalance which is integrated in the evaporation system. However, determination of the tooling factor and the layer quality with e.g. AFM is not accessible for such thin layers. Figure 5-22 illustrates the J-V characteristics of devices with different thicknesses of SiO_x inserted between ITO and HBL.

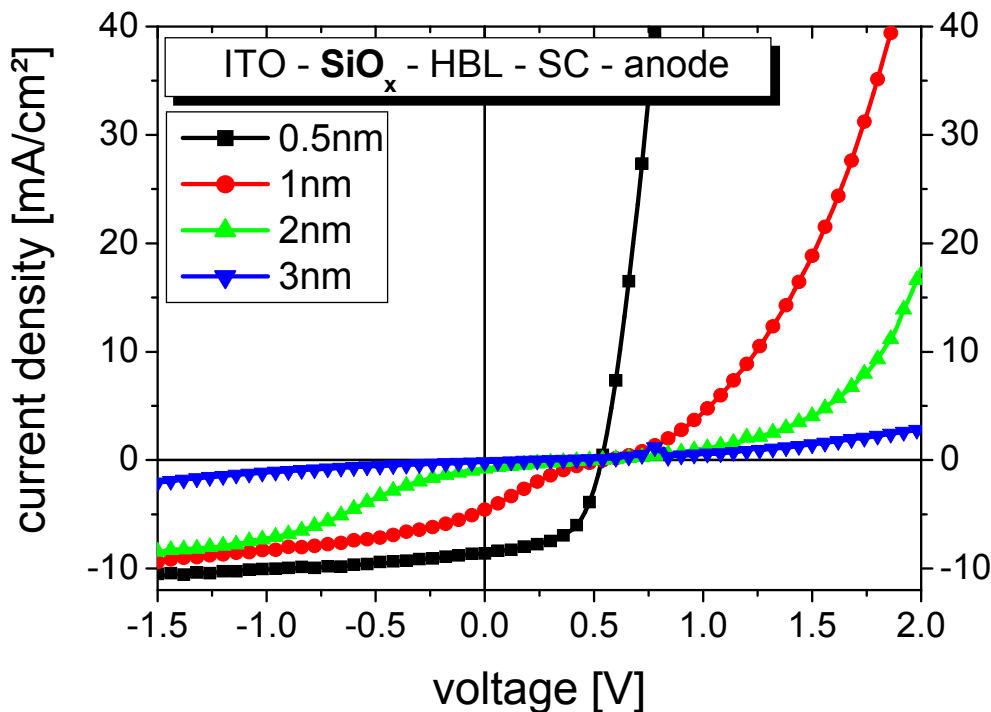


Figure 5-22: J-V characteristics of OPV cells in the inverted device structure ITO-SiO_x-HBL-SC-anode. An SiO_x layer thickness of 0.5 nm, 1 nm, 2 nm and 3 nm is investigated.

For an SiO_x layer thickness of 0.5 nm the J-V characteristic is not affected and the device shows no S-shape J-V characteristics. This suggests that SiO_x does not fully cover the ITO surface and therefore does not affect the performance of the OPV device. An increase in the layer thickness of SiO_x to 1 nm results in an S-shape characteristic which becomes more pronounced with thicker layers. With increasing SiO_x layer thickness the required voltage to extract all carriers increases i.e. V_{th_e} decreases concomitant with an increase in V_{th_i} , the voltage at which the diode opens. V_{oc} remains constant for all layer thicknesses which is an

indicator that SiO_x indeed does not change V_{bi} . A similar effect is observed when SiO_x is inserted between HBL and the semiconducting layer, neglecting slight differences at a SiO_x layer thickness of 1 nm. (Figure 5-23)

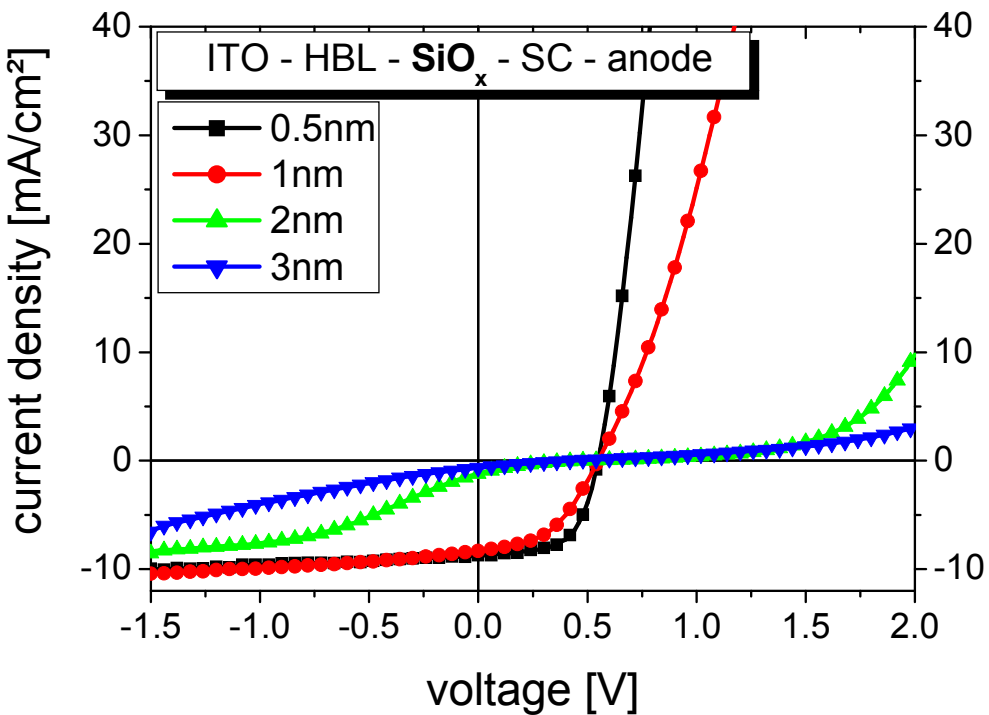


Figure 5-23: J-V characteristics of OPV cells in the inverted device structure ITO-HBL- SiO_x -SC-anode. An SiO_x layer thickness of 0.5 nm, 1 nm, 2 nm and 3 nm is investigated.

An increase in the layer thickness of SiO_x from 1 nm to 3 nm results in a more pronounced S-shape J-V characteristics. Moving the layer from one position in the cell stack to the other proves that the S-shape is introduced by the SiO_x layer and not by a change in surface morphology or wettability of the HBL. The slightly different S-shapes compared to the structure ITO/HBL/ SiO_x and ITO/ SiO_x /HBL either stem from different effective layer thicknesses or a different coverage of the SiO_x . The more pronounced S-shape J-V characteristic with increased SiO_x layer thickness for both cases is in excellent agreement with experimental J-V-curves presented in chapter 5.2.3 as well as with the simulations where it is shown that the increase in the degree of S-shape characteristics correlates with a decrease in conductivity. An increase in layer thickness of the SiO_x suggests an increased resistance through a passivation of the interface. This results in a decreased conductivity of

the interfacial layer stack. Figure 5-24 illustrates J-V characteristics without HBL, i.e. of a device ITO/SiO_x/P3HT:PCBM.

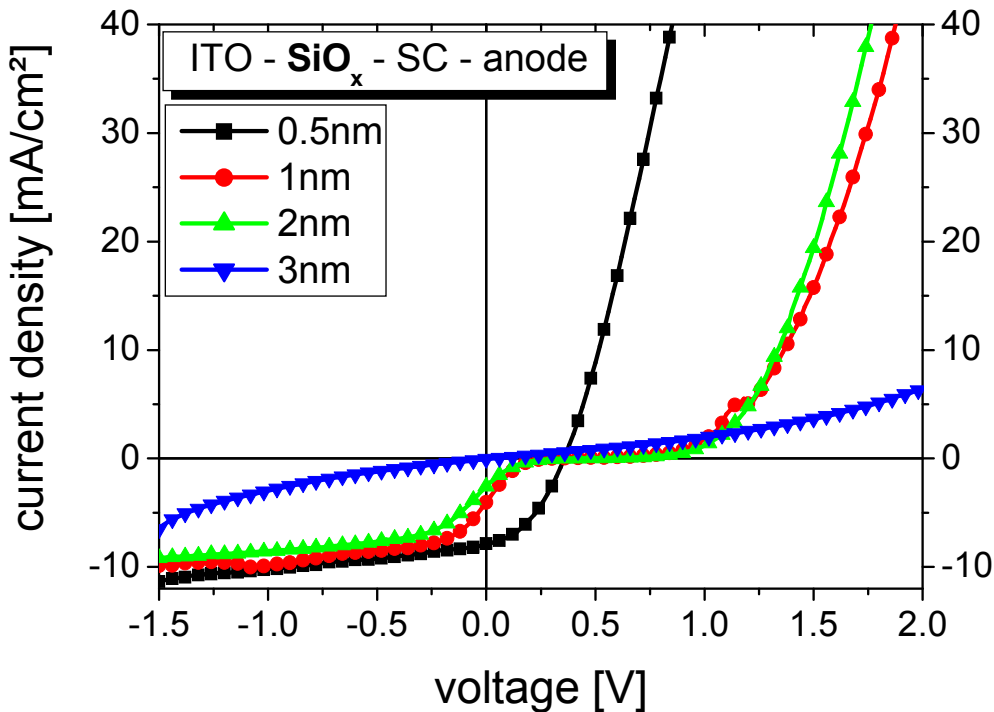


Figure 5-24: J-V characteristics of OPV cells in the inverted device structure ITO-SiO_x-SC-anode. An SiO_x layer thickness of 0.5 nm, 1 nm, 2 nm and 3 nm is investigated.

V_{oc} is reduced compared to devices with HBL which is explained by the non-adjusted interface. Excluding the loss in V_{oc} , the same tendency as for devices with HBL and SiO_x is observable. The incorporation of a thicker layer of SiO_x at the interface results in more pronounced S-shape J-V characteristics which are related to a lower conductivity at the interface. In conclusion it is shown that S-shape J-V characteristics can be produced by purposely lowering the conductivity of the interfacial layer at the cathode by evaporating thin layers of SiO_x. S-shape J-V characteristics are observed irrespective of the position of SiO_x, i.e. below or on top of the HBL. Results can be summarized as follows:

- (a) The insertion of an SiO_x layer thicker than 1nm results in an S-shape J-V characteristics.

Introducing the SiO_x at different positions of the cathode excludes morphological reasons of the HBL as origin of the S-shape.

- (b) An increase of the SiO_x layer thickness results in a more pronounced S-shape J-V characteristics. With increasing SiO_x layer thickness $V_{\text{th_e}}$ shifts to lower voltages and $V_{\text{th_i}}$ shifts to higher voltages. V_{oc} is constant.
- (c) The combined results support that a reduced conductivity is one major reason for the occurrence of the S-shape J-V characteristics.

5.2.5 Summary

TiO_x is investigated as interfacial layer, which is switchable by UV irradiation from an unadjusted and device performance limiting interfacial layer to an excellent interfacial layer. The S-shape J-V characteristic with VIS light illumination and the vanishing of the S-shape J-V characteristics with UV-VIS irradiation is investigated. The change in the performance of the OPV device is correlated with the change in the properties of the TiO_x interfacial layer. UV-VIS irradiation of TiO_x does increase significantly the conductivity of TiO_x while irradiation without UV radiation leads to a decrease of the conductivity of TiO_x from the high conductivity state. The change from a performance limited OPV cell to a non-limited OPV cell is correlated with an increase in the conductivity of the TiO_x . A high conductivity of TiO_x is essential for the non-S-shape J-V characteristic. These experimental findings are substantiated by simulations where the S-shape J-V characteristic vanishes by a change in the conductivity of the TiO_x interfacial layer and vice versa. For the S-shape J-V characteristic the electrical field within the device drops over and nearby the TiO_x interfacial layer and become very little within the photo-active layer. For J-V characteristics without S-shape the electrical field is high within the photo-active layer. These results are corroborated by experimental results, where the incorporation of thin layers of SiO_x and the concomitant decrease of the conductivity of the interfacial layers, results in the S-shape J-V characteristics which does not vanish by UV-VIS irradiation.

6 Summary and Conclusion

Organic photovoltaic (OPV) is a promising technology that converts light into electricity. OPV is especially attractive for future energy supply scenarios because of low cost roll-to-roll production on flexible substrates and little energy pay back times. In this work design rules for OPV cells for several applications of OPV and for the integration of single cells to modules are derived.

The shunt resistance of an OPV cell is identified as important parameter in this work for matching the requirements of an OPV module which is operated either in low light or under 1 sun illumination. The shunt resistance is profoundly impacted by interface materials which can drastically limit the device performance. Unadjusted interface materials can drastically limit device performance.

It is demonstrated that a high shunt resistance and a low leakage current of a single cell is essential for the reverse bias stability which is an important parameter in the case of partial module shading. OPV cells with a leakage current higher than $100 \mu\text{A}/\text{cm}^2$ at -1 V show a fast degradation under reverse bias stressing at -5 V for 5 h by a decrease of the shunt resistance under formation of so-called hot spots. The amount and strength of such hot spots increases under reverse bias stressing. OPV cells with a sufficiently low leakage current ($< 100 \mu\text{A}/\text{cm}^2$ at -1 V) do survive reverse bias stressing at -5 V for 5 h without further increase in the leakage current.

For indoor applications, i.e. low light applications, a high shunt resistance is required. Cells with comparable performances at 1 sun but different shunt resistances show different performance under low light conditions. Only those cells with a sufficiently high shunt resistance will supply power under indoor illumination. For low light applications a shunt resistance of $85 \text{k}\Omega\text{cm}^2$ compared to a shunt resistance of $1 \text{k}\Omega\text{cm}^2$ for illumination at 1 sun is required. The serial resistance is less important for low light applications compared to illumination at 1 sun. A serial resistance of below $50 \Omega\text{cm}^2$ is required compared to $3 \Omega\text{cm}^2$ for illumination at 1 sun. The less severe impact of the serial resistance to the device performance for low light conditions allows the use of less conductive electrode and interfacial materials. Therefore, alternative and cheaper materials with better properties might become feasible.

It is demonstrated that OPV cells with a sufficiently high shunt resistance are feasible for organic bypass diodes and competitive to inorganic ones. The monolithic integration of organic solar cells as bypass diodes in modules retains the advantages of organic photovoltaic since a “one colour” printing step of modules and bypass diodes on a flexible substrate is possible.

For determination of the origin of hot spots a measurement method is developed utilizing the combination of lock-in thermography with light beam induced current measurements. This method allows distinguishing between an interface shunt and bulk shunt. Results on the OPV cells under study suggest an interface shunt as origin of the hot spots, i.e. the active layer is intact and the interfacial layers are damaged.

An approach to improve the interfaces and thus avoid interface shunts is also demonstrated. Stacking of solution processed titanium oxide (TiO_x) and polyoxyethylene tridecyl ether (PTE) at the electron selective contact results in an improvement in both the shunt resistance and cell efficiency because of higher fill factor (FF). The power conversion efficiency increases to 3.6 % compared to 3.2 % without PTE in the inverted device geometry. The improvement is related to a better layer quality of the TiO_x by incorporation of PTE between ITO and TiO_x .

The impact and need for the right choice of interface materials is discussed in detail for TiO_x as electron selective contact. This material enables closer investigations of an interface material because it is switchable by UV irradiation from a performance limiting interfacial layer to an excellent interfacial layer. OPV cells with TiO_x show an S-shape current-voltage (J-V) characteristic with VIS illumination and no S-shape J-V characteristic with UV-VIS irradiation. The TiO_x layer changes its conductivity with UV irradiation which correlates with the vanishing and occurrence of the S-shape J-V characteristics. This behaviour is elucidated with simulations and it is found that in the presence of an S-shape J-V characteristic the drop of the electric field is confined to the interfacial layer. For the J-V characteristics without S-shape the drop of the electric field within the photo-active layer is higher. This result is further substantiated by an experimental decrease of the conductivity of the interfacial layer: The incorporation of silicon oxide at the electron selective contact leads to an S-shape J-V characteristic which does not vanish by UV-VIS irradiation. From the experiments it is concluded that the S-shape J-V characteristic originates from the low conductivity of the TiO_x interfacial layer.

In conclusion, this work demonstrates that the appropriate choice of interface materials is of paramount importance for OPV cells and modules to guarantee high performance. The right choice of interface materials significantly contributes to the stability and performance of OPV devices. An unadjusted interfacial layer can reduce the efficiency of an OPV cell by e.g. introducing S-shape J-V characteristics. A literature review is presented which summarizes the present status of interfacial materials used for OPV.

Only OPV cells with optimized PCE and lifetime will further increase the potential and attractiveness of the OPV technology and make this technology to be competitive to other photovoltaic technologies and energy sources. The development of novel interfacial materials must go hand in hand with the development of high-efficiency active layer materials.

Abbreviations and Symbols

Alq ₃	tris(8-hydroxyquinoline)aluminium
AM	air mass
BA-X	parasubstituted benzoic acid
BCP	bathocuproine
BPhen	bathophenanthroline
c	specific heat capacity
CBC	4-chlorobenzoylchloride
CBP	4-chlorophenyldichlorophosphate
CBS	4-chlorobenesulfonyl chloride
CO ₂	carbon dioxide
CoCp ₂	decamethylcobaltocene
D	gas-phase dipole moment
DLIT	dark lock-in thermography
e	elementary charge
E	electrical field
E _b	binding energy
E _{ICT-}	negative integer charge-transfer states
E _{ICT+}	positive integer charge-transfer states
E _k	kinetic energy
FF	fill factor
f _{li}	lock-in frequency
G	generation rate
GPEC	global primary energy consumption
HBL	hole blocking layer
HOMO	highest occupied molecular orbital
I	current
I ₀	saturation current
I _{photogenerated}	photo-generated current
IR	infrared

Abbreviations and Symbols

ITO	indium tin oxide
J	current density
J_{sc}	short-circuit current density
k_B	boltzmann constant
LBIC	light beam induced current (LBIC)
LUMO	lowest occupied molecular orbital
m	mass
MDMO-PPV	poly(2-methoxy-5-(3',7'-dimethyloctyloxy)-1,4-phenylenevinylene)
MIM	metal-insulator-metal
MPP	maximum power point
n	negative charge carrier density
n_i	ideality factor
OLED	organic light emitting diode
OPV	organic photovoltaic
p	positive charge carrier density
P3HT	poly(3-hexylthiophene)
PANI	polyaniline
PCBM	[6,6]-phenyl C61 butyric acid methyl ester
PCE	power conversion efficiency
PEDOT	poly(3,4-Ethylenedioxythiophene)
P_{el}	electrical power
P_{IN}	luminous power hitting the cell
P_{OUT}	electric power output at the MPP
PSS	poly(styrene-sulfonate)
PTE	polyoxyethylene tridecyl ether
PV	photovoltaic
Q	amount of energy transferred through heat
R	recombination rate
R_p	shunt resistance
R_s	serial resistance
SAM	self-assembled monolayer
SiO_x	silicon oxide

T	temperature
TiO _x	titanium oxide
UPS	ultraviolet photoelectron spectroscopy
UV	ultraviolet
V	voltage
V _{bi}	built-in voltage
VIS	visible
V _{oc}	open-circuit voltage
V _{th_e}	threshold voltage for extraction
V _{th_i}	threshold voltage for injection
XPS	x-ray photoelectron spectroscopy
σ	conductivity
Φ	work function
ρ	net charge
ε	dielectric constant
Λ	thermal diffusion length
ρ_d	density
λ	thermal conductivity
$h\nu$	energy of photon
μ_n	electron mobility
μ_p	hole mobility

List of Figures

Figure 1-1: Comparison of the available renewable energy sources to the global primary	1
Figure 1-2: Global annual PV market growth (policy driven scenario).	2
Figure 2-1: Chemical structure of polyacetylene.	8
Figure 2-2: Scheme of light harvesting and charge generation in OPV cells.....	10
Figure 2-3: One diode model of a solar cell.	12
Figure 2-4: Impact of R_s and R_p on the performance of OPV cells at 1 sun.	13
Figure 2-5: Comparison of the AM1.5 spectrum of the sun with the absorption of P3HT.	15
Figure 2-6: Comparison of the absorption of P3HT with the spectrum of a fluorescent lamp	16
Figure 2-7: Schematic illustration of the doctor-blade technique.	17
Figure 2-8: Chemical structure of (a) PCBM, (b) P3HT, (c) PEDOT and PSS.	19
Figure 2-9: (a) Inverted device structure investigated in this work and acting as reference ...	19
Figure 2-10: Exemplary layout of the investigated OPV cells.	20
Figure 2-11: Schematics of a serially interconnected 3 stripe module.	21
Figure 2-12: Schematic illustration of the principle of the conductivity measurement.	22
Figure 2-13: Schematic illustration of the DLIT measurement setup.	24
Figure 3-1: Dependence of the work function of molecule-coated substrates	28
Figure 3-2: Schematic illustration of the evolution of the energy-level alignment	29
Figure 3-3: a) V_{oc} versus acceptor strength and b) V_{oc} versus electrode work function.	32
Figure 3-4: V_{oc} of different bulk-heterojunction solar cells plotted versus the oxidation....	33
Figure 3-5: Device structure in the normal (left) and inverted structure (right).	34
Figure 3-6: J-V curves in a semilogarithmic representation for the normal.....	35
Figure 3-7: Schematic representation of the spatial distribution of the squared optical	37
Figure 3-8: V_{oc} , FF, and normalized efficiency vs negative electrode type..	39
Figure 3-9: Work function of the elementary solids.	40
Figure 3-10: Energy level diagram of p-type and n-type metal oxides incorporated.....	41
Figure 3-11: Photo I-V curves of the FTO/amorphous TiO_x /P3HT:PCBM/PEDOT:PSS/Au	43
Figure 3-12: Illustration showing the device configuration, materials used	44
Figure 3-13: J_{sc} (filled squares), V_{oc} (open circles), FF (filled upward triangles).....	46
Figure 3-14: Current density vs voltage (J-V) characteristics of the diodes under 1 sun.....	48
Figure 3-15: Schematic illustration of the monolayer adsorption of Bro.nsted acids	49
Figure 3-16: He I UPS spectrum of ITO taken with 25.000 V bias applied to the sample.	50
Figure 3-17: a) Evolution of secondary electron edge with different buffer layers on ITO....	53
Figure 4-1: Dark J-V characteristics of OPV cells processed while this work with.	55
Figure 4-2: Representative J-V characteristics of the solar cell studied under illumination... <td>58</td>	58
Figure 4-3: DLIT measurement: Image size represents active area of an organic solar cell... <td>59</td>	59
Figure 4-4: The degradation at -5 V for 5 h in dependence of the leakage current.....	61
Figure 4-5: Comparison of the spectrum of a fluorescent lamp and the AM1.5 spectrum	63
Figure 4-6: Illustration of the impact of R_p and R_s to the J-V characteristics of OPV cells....	64
Figure 4-7: Impact of R_p to the (a) power output, (b) V_{oc} and (c) FF of OPV cells.	65
Figure 4-8: (a) Dark J-V characteristic of an organic, a Ge and a Si diode.....	72
Figure 4-9: Normalized power output versus the voltage that applies on the bypass diode.. .	74
Figure 4-10: Schematic illustration of a device with different types of shunts.	76

List of Figures

Figure 4-11: DLIT amplitude image	78
Figure 4-12: Amplitude signal of the hot-spot presented in Figure 4-11.....	79
Figure 4-13: LBIC maps with a step size of $10 \mu\text{m} \times 10 \mu\text{m}$	80
Figure 5-1: Device structure of the inverted OPV structure with and without PTE	84
Figure 5-2: Representative dark (a) and light (b) J-V characteristics of the solar cells.....	85
Figure 5-3: Comparison of the power conversion efficiency, fill factor	87
Figure 5-4: Binding energy vs. counts for the structures under investigation	88
Figure 5-5: Binding energy vs. counts for the structures under investigation	89
Figure 5-6: Binding energy vs. counts for the structures under investigation	90
Figure 5-7: Topographic atomic force microscope image (contact mode) of the TiO_x	91
Figure 5-8: J-V characteristics of OPV cells with the device structures.....	93
Figure 5-9: Transmission of the UV-filter foil used for VIS irradiation of the OPV cell.	94
Figure 5-10: Time dependence of the injection current density at +1 V (a), FF (b)	96
Figure 5-11: Conductivity of sol-gel processed TiO_x with UV-VIS and VIS irradiation	97
Figure 5-12: Graph of the device structure of the investigated device model.....	99
Figure 5-13: The simulated (open symbols) together with the measured.....	101
Figure 5-14: The simulated (open symbols) together with the measured.....	102
Figure 5-15: Simulated J-V characteristics of an OPV cell with and without S-shape.	103
Figure 5-16: (a) presents the simulated J-V characteristics with and without S-Shape.....	105
Figure 5-17: (a) presents the simulated J-V characteristics with and without S-Shape.....	106
Figure 5-18: (a) presents the simulated J-V characteristics with and without S-Shape.....	107
Figure 5-19: (a) presents the simulated J-V characteristics with and without S-Shape.....	108
Figure 5-20: Simulated electric field distribution within the polymer blend.....	109
Figure 5-21: Simulated electric field distribution within the polymer blend.....	110
Figure 5-22: J-V characteristics of OPV cells in the inverted device structure	112
Figure 5-23: J-V characteristics of OPV cells in the inverted device structure	113
Figure 5-24: J-V characteristics of OPV cells in the inverted device structure	114

List of Tables

Table 1: Device operation parameters for devices with different types of anodes.....	42
Table 2: Summary of device performance of polymer solar cells with different.....	51
Table 3: List of relevant parameters for the simulation performed with PC1D.	100

Bibliography

- 1 Set for 2020, European Photovoltaic Industry Association, 2009.
- 2 F. Nitsch, Technologische und energiewirtschaftliche Perspektiven erneuerbarer Energien, Deutsches Zentrum für Luft- und Raumfahrt (DLR), 2007.
- 3 Meteotest, database Meteonorm, www.meteonorm.com.
- 4 <http://www.desertec.org/en/>.
- 5 Global market outlook for photovoltaics until 2013, European Photovoltaic Industry Association, 2009.
- 6 C. Brabec, D. Dyakonov, U. Scherf, Organic Photovoltaics, WILEY-VCH, 2008, 978-3-527-31675-5.
- 7 <http://www.konarka.com>.
- 8 <http://www.solarmer.com>.
- 9 J. A. Hauch, P. Schilinsky, S. A. Choulis, S. Rajoelson and C. J. Brabec, *Appl. Phys. Lett.*, 2008, 93, 103306.
- 10 C. Hoth, S. A. Choulis, P. Schilinsky, and C. J. Brabec, *Adv. Mater.*, 2007, 19, 22, 3973.
- 11 C. N. Hoth, Pavel Schilinsky, Stelios A. Choulis and Christoph J. Brabec, *Nano Lett.*, 2008, 8, 9, 2806.
- 12 H. Shirakawa, E. J. Louis, A. G. MacDiarmid, C. K. Chiang, A. J. Heeger, *Chem. Commun.*, 1977, 578.
- 13 C. K. Chiang, C. R. Fincher, Jr., Y. W. Park, A. J. Heeger, H. Shirakawa, E. J. Louis, *Phys. Rev. Lett.*, 1977, 39, 1098.
- 14 http://nobelprize.org/nobel_prizes/chemistry/laureates/2000/.
- 15 C. W. Tang, *Appl. Phys. Lett.*, 1986, 48, 183.
- 16 C. Gärtner, Organic Lased Diodes – Modelling and Simulations, Universitätsverlag Karlsruhe, 2009, 978-3-86644-345-7.
- 17 A. J. Heeger, *Angew. Chem. Int. Ed.*, 2001, 40, 2591.
- 18 P. W. M. Blom, V. D. Mihailetschi, L. J. A. Koster and D. E. Markov, *Adv. Mater.*, 2007, 19, 1551.
- 19 Pavel Schilinsky, Loss Analysis of the Power Conversion Efficiency of Organic Bulk Heterojunction Solar Cells, http://oops.uni-oldenburg.de/frontdoor.php?source_opus=180.
- 20 P. Schilinsky, C. Waldauf, C. J. Brabec, *Adv. Funct. Mater.* 2006, 16, 1669.
- 21 P. Schilinsky, C. Waldauf, and C. J. Brabec, *Appl. Phys. Lett.*, 2002, 81, 3885.
- 22 I. Riedel, J. Parisi, V. Dyakonov, L. Lutsen, D. Vanderzande, and J. C. Hummelen, *Adv. Funct. Mater.*, 2004, 14, 38.
- 23 S. M. Sze. Physics of Semiconductor Devices. Wiley, 1981, 0-471-05661-8..
- 24 <http://www.pv.unsw.edu.au/links/products/pc1d.asp>.
- 25 J. Nelson, The Physics of Solar Cells, Imperial College Press, 2003, 1-86094-340-3.
- 26 P. Flesch, Light and light sources: high intensity discharge lamps, 103-540-32684-7.
- 27 R. Steim, Rene F. Kogler, and C. J. Brabec, Interface Materials of Organic Solar Cells, *Journal of Materials Chemistry*, 2010, DOI: 10.1039/B921624C.
- 28 <http://www.ircam.de>
- 29 J. Bachmann, C. Buerhop-Lutz, C. Deibel, I. Riedel, H. Hoppe, C.J. Brabec, V. Dyakonov, *Sol. Energy Mater. Sol. Cells*, 2009, doi:10.1016/j.solmat.2009.11.006.
- 30 O. Breitenstein, M. Langenkamp, Lock-In Thermography, Springer, 2003, 3-540-00405-X
- 31 J. C. Rivière, S. Myhra, Handbook of surface and interface analysis methods for problem solving, Taylor&Francis group, 2009, 978-0-8493-7558-3
- 32 http://en.wikipedia.org/wiki/X-ray_photoelectron_spectroscopy
- 33 K. W. Böer, Survey of semiconductor physics, Van Nostrand Reinhold, 1992, 0-442-00672-1.
- 34 A. Crispin, X. Crispin, M. Fahlman, M. Berggren and W. R. Salaneck, *Appl. Phys. Lett.*, 2006, 89, 213503.
- 35 S. Braun, W. R. Salaneck and M. Fahlman, *Adv. Mater.*, 2009, 21, 1450.
- 36 W. Osikowicz, M. P. de Jong and W. R. Salaneck, *Adv. Mater.*, 2007, 19, 4213.
- 37 C. D. Lindstrom and X.-Y. Zhu, *Chem. Rev.*, 2006, 106, 4281.
- 38 X. Crispin, V. Geskin, A. Crispin, J. Cornil, R. Lazzaroni, W. R. Salaneck and J. L. J. Bredas, *J. Am. Chem. Soc.*, 2002, 124, 8131.
- 39 H. Ishii, K. Sugiyama, E. Ito and K. Seki, *Adv. Mater.*, 1999, 11, 605.
- 40 V. D. Mihailetschi, P. W. M. Blom, J. C. Hummelen and M. T. Rispens, *J. Appl. Phys.*, 2003, 94, 6849.

Bibliography

- 41 C. J. Brabec, A. Cravino, D. Meissner, N. S. Sariciftci, T. Fromherz, M. T. Rispens, L. Sanchez and J. C. Hummelen, *Adv. Funct. Mater.*, 2001, 11, 374.
- 42 M. C. Scharber, D. Mühlbacher, M. Koppe, P. Denk, C. Waldauf, A. J. Heeger and C. J. Brabec, *Adv. Mater.*, 2006, 18, 789.
- 43 A. Cravino, *Appl. Phys. Lett.*, 2007, 91, 243502.
- 44 M. Campoy-Quiles, T. Ferenczi, T. Agostinelli, P. G. Etchegoin,
Y. Kim, T. D. Anthopoulos, P. N. Stavrinou, D. D. C. Bradley and J. Nelson, *Nat. Mater.*, 2008, 7, 158.
- 45 Z. Xu, L.-M. Chen, G. Yang, C.-H. Huang, J. Hou, Y. Wu, G. Li, C.-S. Hsu and Y. Yang, *Adv. Funct. Mater.*, 2009, 19, 1227–1234.
- 46 Waldauf, M. Morana, P. Denk, P. Schilinsky, K. Coakley, S. A. Choulis and C. J. Brabec, *Appl. Phys. Lett.*, 2006, 89, 233517.
- 47 X. L. Chen, B. H. Xu, J. M. Xue, Y. Zhao, C. C. Wei, J. Sun, Y. Wang, X. D. Zhang and X. H. Geng, *Thin Solid Films*, 2007, 515, 3753–3759.
- 48 V. Bhosle, J. T. Prater, Fan Yang, D. Burk, S. R. Forrest and J. Narayan, *J. Appl. Phys.*, 2007, 102, 023501.
- 49 J. Owen, M. S. Som, K.-H. Yoo, B. D. Ahn and S. Y. Lee, *Appl. Phys. Lett.*, 2007, 90, 033512.
- 50 Y. Yamamoto, K. Saito, K. Takahashi and M. Konagai, *Sol. Energy Mater. Sol. Cells*, 2001, 65, 125.
- 51 S. Park, S. J. Tark, J. S. Lee, H. Lim and D. Kim, *Sol. Energy Mater. Sol. Cells*, 2009, 93(6–7), 1020–1023.
- 52 O. Kluth, B. Rech, L. Hoben, S. Wieder, G. Schöpe, C. Beneking, H. Wagner and A. Löffl, *Thin Solid Films*, 1999, 351, 247.
- 53 M. W. Rowell, M. A. Topinka, M. D. McGehee, H. J. Prall, G. Dennler, N. S. Sariciftci, L. B. Hu and G. Gruner, *Appl. Phys. Lett.*, 2006, 88, 233506.
- 54 G. Eda, Y. Y. Lin, S. Miller, C. W. Chen, W. F. Su and M. Chhowalla, *Appl. Phys. Lett.*, 2008, 92, 233305.
- 55 Y. H. Zhou, F. L. Zhang, K. Tvingstedt, S. Barrau, F. H. Li, W. J. Tian and O. Inganäs, *Appl. Phys. Lett.*, 2008, 92, 233308.
- 56 K. Tvingstedt, O. Inganäs, *Adv. Mater.*, 2007, 19, 2893–2897.
- 57 J. Y. Lee, S. T. Connor, Y. Cui and P. Peumans, *Nano Lett.*, 2008, 8, 689–692.
- 58 B. O'Connor, C. Haughn, K. H. An, K. P. Pipe and M. Shtein, *Appl. Phys. Lett.*, 2008, 93, 223304.
- 59 C. Guillen and J. Herrero, *Sol. Energy Mater. Sol. Cells*, 2008, 92, 938–941.
- 60 B. V. Andersson, D. M. Huang, H. J. Moule and O. Inganäs, *Appl. Phys. Lett.*, 2009, 94, 043302.
- 61 J. Y. Kim, S. H. Kim, H. H. Lee, K. Lee, W. Ma, X. Gong and A. J. Heeger, *Adv. Mater.*, 2006, 18, 572.
- 62 A. Roy, S. H. Park, S. Cowan, M. H. Tong, S. Cho, K. Lee and A. J. Heeger, *Appl. Phys. Lett.*, 2009, 95, 013302.
- 63 S. H. Park, A. Roy, S. Beaupre, S. Cho, N. Coates, J. S. Moon, D. Moses, M. Leclerc, K. Lee and A. J. Heeger, *Nat. Photonics*, 2009, 3, 297.
- 64 K. Suemori, M. Yokoyama and M. Hiramoto, *J. Appl. Phys.*, 2006, 99, 036109.
- 65 M. O. Reese, A. J. Morfa, M. S. White, N. Kopidakis, S. E. Shaheen, G. Rumbles and D. S. Ginley, *Sol. Energy Mater. Sol. Cells*, 2008, 92, 746–752.
- 66 S. T. Lee, Z. Q. Gao and L. S. Hung, *Appl. Phys. Lett.*, 1999, 75, 10.
- 67 K. Lee, J. Y. Kim, S. H. Park, S. H. Kim, S. Cho and A. J. Heeger, *Adv. Mater.*, 2007, 19, 2445.
- 68 M. D. Irwin, B. Buchholz, A. W. Hains, R. P. H. Chang and T. J. Marks, *Proc. Natl. Acad. Sci. U. S. A.*, 2008, 105, 2783–2787.
- 69 A. R. Schlatmann, D. Wilms Floet, A. Hilberer, F. Garten, P. J. M. Smulders, J. M. Klapwijk and G. Hadzioannou, *Appl. Phys. Lett.*, 1996, 69, 1764.
- 70 P. Peumans and S. R. Forrest, *Appl. Phys. Lett.*, 2001, 79, 126.
- 71 Y. Hirose, A. Kahn, V. Aristov, P. Soukiassian, V. Bulovic and S. R. Forrest, *Phys. Rev. B: Condens. Matter*, 1996, 54, 13748.
- 72 P. Peumans, V. Bulovic and S. R. Forrest, *Appl. Phys. Lett.*, 2000, 76, 2650.
- 73 J. Blochwitz, M. Pfeiffer, T. Fritz and K. Leo, *Appl. Phys. Lett.*, 1998, 73, 729.
- 74 W. Gao and A. Kahn, *Org. Electron.*, 2002, 3, 53.
- 75 W. Gao and A. Kahn, *J. Appl. Phys.*, 2003, 94, 359.
- 76 C. K. Chan, F. Amy, Q. Zhang, S. Barlow, S. Marder and A. Kahn, *Chem. Phys. Lett.*, 2006, 431, 67.
- 77 C. K. Chan, W. Zhao, S. Barlow, S. Marder and A. Kahn, *Org. Electron.*, 2008, 9, 575.
- 78 Steven K. Hau, Hin-Lap Yip, Kirsty Leong and Alex K.-Y. Jen, *Org. Electron.*, 2009, 10(4), 719–723.
- 79 Jung-Yong Lee, Stephen T. Connor, Yi Cui and Peter Peumans, *Nano Lett.*, 2008, 8(2), 689–692.

- 80 M. O. Reese, M. S. White, G. Rumbles, D. S. Ginley and S. E. Shaheen, *Appl. Phys. Lett.*, 2008, 92, 053307.
81 Herbert B. Michaelson, *J. Appl. Phys.*, 1977, 48(11), 4729.
82 M. Chikamatsu, T. Taima, Y. Yoshida, K. Saito and K. Yase, *Appl. Phys. Lett.*, 2004, 84, 127.
83 A. Colsmann, *Ladungstransportschichten für effiziente organische Halbleiterbauelemente*, Universitätsverlag Karlsruhe, 2009, 978-3-86644-332-7.
84 C. Tao, S. Ruan, G. Xie, X. Kong, L. Shen, F. Meng, C. Liu, X. Zhang, W. Dong and W. Chen, *Appl. Phys. Lett.*, 2009, 94, 043311.
85 M. Y. Chan, C. S. Lee, S. L. Lai, M. K. Fung, F. L. Wong, H. Y. Sun, K. M. Lau and S. T. Lee, *Appl. Phys. Lett.*, 2006, 100, 094506.
86 S. Han, W. S. Shin, M. Seo, D. Gupta, S.-J. Moon and S. Yoo, *Org. Electron.*, 2009, 10, 791, DOI: 10.1016/j.orgel.2009.03.016.
87 V. Shrotriya, G. Li, Y. Y. Yao, C. W. Chu and Y. Yang, *Appl. Phys. Lett.*, 2006, 88, 073508.
88 K. Takanezawa, K. Tajima and K. Hashimoto, *Appl. Phys. Lett.*, 2008, 93, 063308.
89 J. S. Huang, C. Y. Chou, M. Y. Liu, K. H. Tsai, W. H. Li and C. F. Lin, *Org. Electron.*, 2009, 10, 1060–1065.
90 H.-H. Liao, L.-M. Chen, Z. Xu, G. Li and Y. Yang, *Appl. Phys. Lett.*, 2008, 92, 173303.
91 A. K. K. Kyaw, X. W. Sun, C. Y. Jiang, G. Q. Lo, D. W. Zhao and D. L. Kwong, *Appl. Phys. Lett.*, 2008, 93, 221107.
92 L. Cattin, F. Dahou, Y. Lare, M. Morsli, R. Tricot, S. Houari, A. Mokrani, K. Jondo, A. Khelil, K. Napo and J. C. Bernède, *J. Appl. Phys.*, 2009, 105, 034507.
93 R. Steim, S. A. Choulis, P. Schilinsky and C. J. Brabec, *Appl. Phys. Lett.*, 2008, 92, 093303.
94 A. Hayakawa, O. Yoshikawa, T. Fujieda, K. Uehara and S. Yoshikawa, *Appl. Phys. Lett.*, 2007, 90, 163517.
95 G. K. Mor, K. Shankar, M. Paulose, O. K. Varghese and C. A. Grimes, *Appl. Phys. Lett.*, 2007, 91, 152111. *Phys. Lett.*, 2007, 91, 152111
96 M. N. M. Glatthaar, B. Zimmermann, P. Lewer, M. Riede, A. Hinsch and J. Luther, *Thin Solid Films*, 2005, 491, 298.
97 J. Gilot, I. Barbu, M. M. Wienk and R. A. J. Janssen, *Appl. Phys. Lett.*, 2007, 91, 113520.
98 M. S. White, D. C. Olson, S. E. Shaheen, N. Kopidakis and D. S. Ginley, *Appl. Phys. Lett.*, 2006, 89, 143517.
99 L. Vayssieres, *Adv. Mater.*, 2003, 15, 464.
100 S. K. Hau, H.-L. Yip, N. S. Baek, J. Zou, K. O’Malley and A. K.-Y. Jen, *Appl. Phys. Lett.*, 2008, 92, 253301.
101 T. Kuwabara, H. Sugiyama, T. Yamaguchi and K. Takahashi, *Thin Solid Films*, 2009, 517(13), 3766–3769.
102 K. Takanezawa, K. Tajima and K. Hashimoto, *Appl. Phys. Lett.*, 2008, 93, 063308.
103 J. S. Huang, C. Y. Chou, M. Y. Liu, K. H. Tsai, W. H. Lin and C. F. Lin, *Org. Electron.*, 2009, 10, 1060–1065.
104 K. Takanezawa, K. Hirota, Q. S. Wei, K. Tajima and K. Hashimoto, *J. Phys. Chem.*, 2007, C111, 7218–7223.
105 I. Gonzalez-Valls and M. Lira-Cantu, *Energy Environ. Sci.*, 2009, 2, 19–34.
106 D. C. Olson, J. Piris, R. T. Collins, S. E. Shaheen and D. S. Ginley, *Thin Solid Films*, 2006, 496, 26.
107 W. H. Baek, I. Seo, T. S. Yoon, H. H. Lee, C. M. Yun and Y. S. Kim, *Sol. Energy Mater. Sol. Cells*, 2009, 93, 1587–1591.
108 G. K. Mor, K. Shankar, M. Paulose, O. K. Varghese and C. A. Grimes, *Appl. Phys. Lett.*, 2007, 91, 152111.
109 M. Nada, T. Gonda, Q. Shen, H. Shimada, T. Toyoda and N. Kobayashi, *Jpn. J. Appl. Phys.*, 2009, 48, 025505.
110 M. H. Park, J. H. Li, A. Kumar, G. Li and Y. Yang, *Adv. Funct. Mater.*, 2009, 19, 1241–1246.
111 A. A. Zakhidov, J. K. Lee, H. H. Fong, J. A. DeFranco, M. Chatzichristidi, P. G. Taylor, C. K. Ober and G. G. Malliaras, *Adv. Mater.*, 2008, 20, 3481–3484.
112 A. Kumar, G. Li, Z. Hong and Y. Yang, *Nanotechnology*, 2009, 20, 165202.
113 K. Walzer, B. Maennig, M. Pfeiffer and K. Leo, *Chem. Rev.*, 2007, 107, 1233–1271.
114 S. E. Shaheen, C. J. Brabec, N. S. Sariciftci, F. Padinger, T. Fromberz and J. C. Hummelen, *Appl. Phys. Lett.*, 2001, 78, 841.
115 Y. Cao, G. Yu, C. Zhang, R. Menon and A. J. Heeger, *Synth. Met.*, 1997, 87, 171.
116 S. A. Carter, M. Angelopoulos, S. Karg, P. J. Brock and J. C. Scott, *Appl. Phys. Lett.*, 1997, 70, 2067.

Bibliography

- 117 J. C. Carter, I. Grizzi, S. K. Heeks, D. J. Lacey, S. G. Latham, P. G. May, O. R. d. I. Panos, K. Pichler, C. R. Towns and H. F. Wittman, *Appl. Phys. Lett.*, 1997, 71, 34.
- 118 C. Y. Li, T. C. Wen, T. H. Lee, T. F. Guo, J. C. A. Huang, Y. C. Lin and Y. J. Hsu, *J. Mater. Chem.*, 2009, 19, 1643.
- 119 C. Y. Li, T. C. Wen, T. F. Guo and S. S. Hou, *Polymer*, 2008, 49, 957.
- 120 G. Gustafsson, Y. Cao, G. M. Treacy, F. Klavetter, N. Colaneri and A. J. Heeger, *Nature*, 1992, 357, 477.
- 121 Y. Yang and A. J. Heeger, *Appl. Phys. Lett.*, 1994, 64, 1245.
- 122 J. Jang, J. Ha and K. Kim, *Thin Solid Films*, 2008, 516, 3152.
- 123 Y. Kim, A. M. Ballantyne, J. Nelson and D. D. C. Bradley, *Org. Electron.*, 2009, 10, 205–209.
- 124 C. J. Ko, Y. K. Lin, F. C. Chen and C. W. Chu, *Appl. Phys. Lett.*, 2007, 90, 063509.
- 125 D. Bagchi and R. Menon, *Chem. Phys. Lett.*, 2006, 425, 114.
- 126 H. J. Snaith, H. Kenrick, M. Chiesa and R. H. Friend, *Polymer*, 2005, 46, 2573.
- 127 S. Timpanaro, M. Kemerink, F. J. Touwslager, M. M. De Koc and S. Schrader, *Chem. Phys. Lett.*, 2004, 394, 339.
- 128 S. Ashizawa, R. Horikawa and H. Okuzaki, *Synth. Met.*, 2005, 153, 5.
- 129 L. A. A. Pettersson, S. Ghosh and O. Inganäs, *Org. Electron.*, 2002, 3, 143.
- 130 S. Ghosh and O. Inganäs, *Synth. Met.*, 2001, 121, 1321.
- 131 S. K. M. Jönsson, J. Birgerson, X. Crispin, G. Greezynski, W. Osikowicz, A. W. D. van der Gon, W. R. Salaneck and M. Fahlman, *Synth. Met.*, 2003, 139, 1.
- 132 F. Zhang, M. Joansson, M. R. Andersson, J. C. Hummelen and O. Inganäs, *Adv. Mater.*, 2002, 14, 662.
- 133 X. Crispin, S. Marciniak, W. Osikowicz, G. Zotti, A. W. Denier van der Gon, F. Louwet, M. Fahlman, L. Groenendaal, F. de Schryver and W. R. Salaneck, *J. Polym. Sci., Part B: Polym. Phys.*, 2003, 41, 2561.
- 134 J. Ouyang, C. W. Chu, F. C. Chen, Q. Xu and Y. Yang, *Adv. Funct. Mater.*, 2005, 15, 203.
- 135 J. Y. Kim, J. H. Jung, D. E. Lee and J. Joo, *Synth. Met.*, 2002, 126, 311.
- 136 J. H. Huang, D. Kekuda, C. W. Chu and K. C. Ho, *J. Mater. Chem.*, 2009, 19, 3704–3712.
- 137 T. Aernouts, P. Vanlaeke, W. Geens, J. Poortmans, P. Heremans, S. Borghs, R. Mertens, R. Andriessen and L. Leenders, *Thin Solid Films*, 2004, 451–452, 22.
- 138 M. Glatthaar, M. Niggemann, B. Zimmermann, P. Lewer, M. Riede, A. Hinsch and J. Luther, *Thin Solid Films*, 2005, 491, 298.
- 139 K. Tvingstedt and O. Inganäs, *Adv. Mater.*, 2007, 19, 2893.
- 140 M. P. de Jong, L. J. van IJzendoorn and M. J. A. de Voigt, *Appl. Phys. Lett.*, 2000, 77, 2255.
- 141 M. Jorgensen, K. Norrman and F. C. Krebs, *Sol. Energy Mater. Sol. Cells*, 2008, 92, 686–714.
- 142 E. Vitoratos, S. Sakkopoulos, E. Dalas, N. Paliatsas, D. Karageorgopoulos, F. Petraki, S. Kennou and S. A. Choulis, *Org. Electron.*, 2009, 10, 61.
- 143 J.-S. Kim, P. K. H. Ho, C. E. Murphy, N. Baynes and R. H. Friend, *Adv. Mater.*, 2002, 14, 206.
- 144 J. Huang, M. Pfeiffer, A. Werner, J. Blochwitz, K. Leo and S. Liu, *Appl. Phys. Lett.*, 2002, 80(1), 139.
- 145 J. Xue, S. Uchida, B. P. Rand and S. R. Forrest, *Appl. Phys. Lett.*, 2004, 85, 5757.
- 146 M. Vogel, S. Doka, Ch. Breyer, M. Ch. Lux-Steiner and K. Fostiropoulos, *Appl. Phys. Lett.*, 2006, 89, 163501.
- 147 A. G. Werner, F. Li, K. Harada, M. Pfeiffer, T. Fritz and K. Leo, *Appl. Phys. Lett.*, 2003, 82, 4495.
- 148 A. G. Werner, F. Li, K. Harada, M. Pfeiffer, T. Fritz, K. Leo and S. Machill, *Adv. Funct. Mater.*, 2004, 14, 255.
- 149 F. Li, M. Pfeiffer, A. Werner, K. Harada and K. Leo, *J. Appl. Phys.*, 2006, 100, 023716.
- 150 F. Li, A. G. Werner, M. Pfeiffer and K. Leo, *J. Phys. Chem. B*, 2004, 108, 17076.
- 151 B. Maenning, J. Drechsel, D. Gebeyehu, P. Simon, F. Kozlowski, A. Werner, F. Li, S. Grundmann, S. Sonntag, M. Koch, K. Leo, M. Pfeiffer, H. Hoppe, D. Meissner, N. S. Sariciftci, I. Riedel, V. Dyakonov and J. Parisi, *Appl. Phys. A: Mater. Sci. Process.*, 2004, 79, 1.
- 152 J. Drechsel, B. Maenning, F. Kozlowski, M. Pfeiffer, K. Leo and H. Hoppe, *Appl. Phys. Lett.*, 2005, 86, 244102.
- 153 M. Y. Chan, S. L. Lai, K. M. Lau, C. S. Lee and S. T. Lee, *Appl. Phys. Lett.*, 2006, 89, 163515.
- 154 C. K. Chan, W. Zhao, A. Kahn and I. G. Hill, *Appl. Phys. Lett.*, 2009, 94, 203306.
- 155 F. Nuesch, L. J. Rothberg, E. W. Forsythe, Quoc Toan Le and Yongli Gao, *Appl. Phys. Lett.*, 1998, 74, 34.
- 156 S. Khodabakhsh, B. M Sanderson, J. Nelson and T. S Jones, *Adv. Funct. Mater.*, 2006, 16, 95–100.
- 157 J. S. Kim, J. H. Park, J. H. Lee, J. Jo, D. Kim and K. Cho, *Appl. Phys. Lett.*, 2007, 91, 112111–3.

- 158 H. L. Yip, S. K. Hau, N. S. Baek, H. Ma and A. K. Y. Jen, *Appl. Phys. Lett.*, 2008, 92, 193313.
- 159 S. K. Hau, H. L. Yip, O. Acton, N. S. Baek, H. Ma and A. K. Y. Jen, *J. Mater. Chem.*, 2008, 18, 5113–5119.
- 160 H. L. Yip, S. K. Hau, N. S. Baek, H. Ma and A. K. Y. Jen, *Adv. Mater.*, 2008, 20, 2376.
- 161 C. J. Brabec, S. E. Shaheen, C. Winder, N. S. Sariciftci and P. Denk, *Appl. Phys. Lett.*, 2002, 80, 1288.
- 162 S. K. M. Jonsson, E. Carlegrim, F. Zhang, W. R. Salaneck and M. Fahlman, *Jpn. J. Appl. Phys.*, 2005, 44, 3695.
- 163 T. M. Brown, R. H. Friend, I. S. Millard, D. J. Lacey, J. H. Burroughes and F. Cacialli, *Appl. Phys. Lett.*, 2000, 77, 3096.
- 164 L. S. Hung, C. W. Tang and M. G. Mason, *Appl. Phys. Lett.*, 1997, 70, 152.
- 165 S. E. Shaheen, G. E. Jabbour, M. M. Morrell, Y. Kawabe, B. Kippelen, N. Peyghambarian, M. F. Nabor, R. Schlaf, E. A. Mash and N. R. Armstrong, *J. Appl. Phys.*, 1998, 84, 2324.
- 166 M. Matsumura, K. Furukawa and Y. Jinde, *Thin Solid Films*, 1998, 331, 96.
- 167 D. Grozea, A. Turak, X. D. Feng, Z. H. Lu, D. Johnson and R. Wood, *Appl. Phys. Lett.*, 2002, 81, 3173.
- 168 J. Kido and T. Matsumoto, *Appl. Phys. Lett.*, 1998, 73, 2866.
- 169 J. Huang, M. Pfeiffer, A. Werner, J. Blochwitz, K. Leo and S. Liu, *Appl. Phys. Lett.*, 2002, 80(1), 139.
- 170 G. Parthasarathy, C. Shen, A. Kahn and S. R. Forrest, *J. Appl. Phys.*, 2001, 89, 4986.
- 171 J. Huang, G. Li and Y. Yang, *Adv. Mater.*, 2008, 20, 415–419.
- 172 H. H. Liao, L. M. Chen, Z. Xu, G. Li and Y. Yang, *Appl. Phys. Lett.*, 2008, 92, 173303.
- 173 M.C. Alonso-Garcia, J.M. Ruiz, Analysis and modelling the reverse characteristic of photovoltaic cells, *Sol. Energy Mater. Sol. Cells* 90 (2006), 1105 – 1120.
- 174 M.C. Alonso-Garcia, W. Herrmann, W. Böhmer and B. Proisy, *Prog. Photovoltaics*, 2003, 11, 5, 293–307
- 175 F.A. Blake, K. L. Hanson, Proceedings of the 4th Intersociety Energy Conversion Engineering Conference, 1969, 575–581.
- 176 European Norm EN-61215, Crystalline Silicon Terrestrial Photovoltaic (PV) Modules-Design Qualification and Type Approval, 1995.
- 177 European Norm EN-61646, thin-film Terrestrial Photovoltaic (PV) Modules-Design Qualification and Type Approval, 1997.
- 178 UL1703, UL Standard for Safety for Flat-plate Photovoltaic Modules and panels, 1993.
- 179 IEEE 1262, IEEE Recommended Practice for Qualification of Photovoltaic (PV) Modules, 1995.
- 180 <http://de.wikipedia.org/wiki/Boxplot>.
- 181 http://www.gaa.baden-wuerttemberg.de/servlet/is/16486/5_007_3.pdf.
- 182 F. C. Krebs, M. Jørgensen, K. Norrman, O. Hagemann, J. Alstrup, T. D. Nielsen, J. Fyenbo, K. Larsen, J. Kristensen, *Sol. Energy Mater. Sol. Cells*, 2009, 93, 422–441.
- 183 E. Molenbroek, D.W. Waddington, Conference Record of the IEEE Photovoltaic Specialists Conference, 1992, 1, 547-552.
- 184 A. Woyte, J. Nijs, R. Belmans, *Solar Energy*, 2003, 74, 3, 217-233.
- 185 F.C. Krebs, Polymer solar cell modules prepared using roll-to-roll methods: knife-over-edge coating slot-die coating and screen printing, *Sol. Energy Mater. Sol. Cells*, 2009, 93, 465–475.
- 186 L. Blankenburg, K. Schultheis, H. Schache, S. Sensfuss, M. Schrödner, *Sol. Energy Mater. Sol. Cells*, 2009, 93, 476–483.
- 187 F.C. Krebs, S.A. Gevorgyan, J. Alstrup, *J. Mater. Chem.*, 2009, 19, 5442.
- 188 F.C. Krebs, *Sol. Energy Mater. Sol. Cells*, 2009, 93, 1636-1641.
- 189 F.C. Krebs, *Org. Electronics*, 2009, 10, 5, 761-768.
- 190 M. Punke, S. Valouch, S.W. Kettlitz, N. Christ, C. Gärtner, M. Gerken, U. Lemmer, *Appl. Phys. Lett.*, 2007, 91, 071118.
- 191 S.F. Tedde, J. Kern, T. Sterzl, J. Fürst, P. Lugli, O. Hayden, *Nano Lett.*, 2009, 9, 3, 980–983.
- 192 D. Zipperer, *Organische Gleichrichter*, Friedrich-Alexander-Universität Erlangen-Nürnberg.
- 193 O. Breitenstein, M. Langenkamp, *Lock-in Thermography*, Springer, 2003 3-540-00405-X.
- 194 K. Pomoni, A. Vomvas, *Chr. Trapalis, Thin Solid Films* 516 (2008), 1271-1278



Organic photovoltaic is an attractive technology to solve future energy supply scenarios. To further increase the potential of this technology novel absorber materials and interface materials have to be developed. In this work the paramount importance of interface materials for efficient as well as stable organic photovoltaic cells and modules is demonstrated. The general requirements of interface materials are elaborated and properties of a novel interface material which meets the demands are investigated experimentally and by simulations.

ISBN 978-3-86644-526-0

ISBN 978-3-86644-526-0



9 783866 445260 >